Dissociation Dynamics of Size-Selected Water Dimer

Dissertation
zur Erlangung des Doktorgrades
an der Fakultät für Mathematik, Informatik und Naturwissenschaften
Fachbereich Physik
der Universität Hamburg

vorgelegt von
Helen Bieker
helen.bieker@cfel.de

Hamburg
2020

Gutachter der Dissertation:	Prof. Dr. Jochen Küpper
	Dr. Daniel A. Horke
Zusammensetzung der Prüfungskommission:	Prof. Dr. Jochen Küpper
	Dr. Daniel A. Horke
	Prof. Dr. Daniela Pfannkuche
	Prof. Dr. Gerhard Grübel
	Prof. Dr. Arwen Pearson
Vorsitzende/r der Prüfungskommission:	Prof. Dr. Daniela Pfannkuche
Datum der Disputation:	29.01.2021
Vorsitzender Fach-Promotionsausschusses PHYSIK:	Prof. Dr. Wolfgang Hansen
Leiter des Fachbereichs PHYSIK:	Prof. Dr. Michael Potthoff
Dekan der Fakultät MIN:	Prof. Dr. Heinrich Graener

Eidesstattliche Versicherung

Hiermit versichere ich an Eides statt, die vorliegende Dissertationschrift selbst verfasst und keine anderen als die angegebenen Hilfsmittel und Quellen benutzt zu haben. Die eingereichte schriftliche Fassung entspricht der auf dem elektronischen Speichermedium. Die Dissertation wurde in der vorgelegten oder einer ähnlichen Form nicht schon einmal in einem früheren Promotionsverfahren angenommen oder als ungenügend beurteilt.

Hamburg, den _____ Unterschrift: _____

Helen Bieker

Abstract

Water is commonly said to be the matrix of life [1, 2]. It is built from water molecules, which are connected via hydrogen bonds. These connections have influences on many biomolecular systems and are the key to understand the importance of water on life. Somehow the smallest drop of water is the water dimer and seems to be a good candidate to study in order to understand the hydrogen bonding in water.

In the framework of this thesis, the behaviour of water dimers in electric fields have been investigated. A cold and pure molecular beam containing $93(15)$ % of water dimers has been created by spatially separating water dimers from several different water-cluster sizes to investigate its photophysics in combination with infrared-laser radiation. Therefore, an inhomogeneous electric field was utilized, leading to a spatial shift of the water dimer and larger water clusters. A simulation of the vertical molecular beam profiles assuming the water dimer to be rigid confirmed the experimental results that the water dimer is deflecting the most, followed by the water hexamer. The initial rotational temperature of the water dimer sample could be determined to be 1.5(5) K.

As the water dimer is known to be a non-rigid molecule, the Stark energies have been calculated taking intermolecular vibrations into account. First, the influence of each intermolecular motion onto the averaged electric dipole moment of the water dimer was investigated. Second, an adiabatic approximation has been used to calculate Stark energies of the non-rigid water dimer, assuming non-interacting intermolecular vibrational motions. It has been shown that the adiabatic description lead to a similar vertical molecular beam profile compared to the rigid-rotor description.

The strong-field ionization of the water dimer was investigated using a high-purity molecular beam produced by an electrostatic deflector. The branching ratios of the water dimer, the anisotropy parameters and the kinetic energy releases of the water dimer fragments following single and double ionization were investigated using a velocity map imaging spectrometer. A slicing method was demonstrated to separate the fragmentation products of interest in time. Single ionization products of water dimer were dominated by a neutral dissociation involving an H_3O^+ fragment. The double ionization creates a Coulomb explosion preferentially into two H_2O^+, but also new fragmentation processes of $2OH^+ + 2H$ and $H_3O^+ + O^+ + H$ were found for the first time.

Zusammenfassung

Wasser, welches aus Wassermolekülen besteht, wird herkömmlicherweise als Matrix des Lebens bezeichnet [1, 2]. Diese Wassermoleküle sind über Wasserstoffbrückenbindungen miteinander verbunden und bilden Wassercluster, welche das Verhalten von biomolekularen Systemen beeinflussen. Diese zu verstehen könnte der Schlüssel zum Verständnis von der Bedeutung von Wasser auf das Leben sein. Der gewissermaßen kleinste Wassertropfen ist das Wasserdimer, welches ein guter Kandidat zu sein scheint um Wasserstoffbrückenbindungen in Wasser zu verstehen.

Im Rahmen dieser Arbeit wurde das Verhalten von Wasserdimeren im elektrischen Feld untersucht. Ein kalter und reiner Molekulstrahl, der zu 93(15) % aus Wasserdimeren besteht, wurde durch eine räumliche Trennung der Wasserdimere von größeren Wasserclustern erzeugt, um die Photophysik mithilfe von Infrarot-Lasern zu untersuchen. Dazu wurde ein inhomogenes elektrische Feld erzeugt, welches zu einer räumlichen Aufteilung von Wasserdimeren und größeren Wasserclustern führte. Eine Simulation der vertikalen Molekularstrahlprofile unter der Annahme eines starren Wasserdimers bestätigte die experimentellen Ergebnisse, dass das Wasserdimer am stärksten ablenkt, gefolgt vom Wasserhexamer. Die ursprünglich Rotationstemperatur der Wasserdimerprobe von 1.5(5) K konnte so bestimmt werden.

Da das Wasserdimer als nicht-starres Molekül bekannt ist, wurden die Stark-Energien unter Berücksichtigung von intermolekularen Vibrationen berechnet. Als Erstes wurde der Einfluss der intermolekularen Bewegungen auf das gemittelte elektrische Dipolmoment des Wasserdimers untersucht. Als Zweites wurde ein adiabatischer Ansatz gewählt um die Stark-Energien eines nicht-starren Wasserdimers zu berechnen, unter der Annahme von nicht-wechselwirkenden intermoleuklaren Bewegungen. Es wurde gezeigt, dass eine adiabatische Beschreibung zu ähnlichen vertikalen Molekülstrahlprofilen wie bei der starren Beschreibung führt.

Starkfeldionization von Wasserdimeren wurde mithilfe eines Molekülstrahls mit hoher Reinheit und einem elektrostatischem Deflektor untersucht. Die Verzweigungsverhältnisse von Wasserdimeren, der Anisotropie Parameter und die kinetische Energiefreisetzung der Fragmente nach einer Einfachionisation und Zweifachionisation wurden mithilfe eines Velocity Map Imaging Spektrometers untersucht. Es wurde gezeigt, dass die genutzte Schneidemethode die interessierenden Fragmentierungsprodukte zeitlich trennt. Die Einfachionisationsprodukte von Wasserdimeren wurde von einer neutralen Dissoziation und einem Zerfall in ein H_3O^+ dominiert. Eine Zweifachionisation hat am wahrscheinlichsten zu einer Coulomb-Explosion in zwei H_2O^+ geführt. Außerdem wurden weitere Zerfallskanäle in $2OH^+ + 2H$ und $H_3O^+ + O^+ + H$ zum ersten Mal gemessen.

Contents

Acronyms

CE Coulomb explosion.

CFEL Center for Free-Electron Laser Science.

CMI Controlled Molecule Imaging.

CUI The Hamburg Center for Ultrafast Imaging.

DESY Deutsches Elektronen-Synchrotron.

EDM electric dipole moment.

FWHM full width at half maximum.

ICD interatomic Coulombic decay.

IP ionization potential.

IR infrared.

KER kinetic energy release.

LIAD laser-induced acoustic desorption.

LIED laser induced electron diffraction.

MCP multi-channel plate.

MEVELER Maximum Entropy Velocity Legendre Reconstruction.

MMI momentum map images.

MS mass spectrum.

MSG molecular symmetry group.

NSSW nuclear spin statistical weights.

OO oxygen-oxygen.

PEPIPICO Photoelectron-Photoion-Photoion coincidence.

PES potential energy surface.

PIPICO Photoion-Photoion coincidence.

SFI strong-field ionization.

TDSE time-dependent Schrödinger equation.

TOF time-of-flight.

VMI velocity map image.

VUV vacuum ultraviolet.

1 Introduction

It is odorless, transparent and tasteless. It is ubiquitous and everyone is using it everyday. No plant and no animal would exist without it and the Earth would look completely different. Also our body consists of more than two thirds of it. Water. It is the most abundant compound on Earth's surface and it is the second most abundant molecule after H_2 in the universe. As it plays such a crucial role in life, its existence on planets and asteroids has been linked with the possibility of extraterrestrial life [3, 4]. Water has been the focus of many studies, where it showed exceptional properties [5, 6]. One famous anomaly is the density anomaly, which describes that the density of water reaches its maximum at 4° C. Due to this special property of water, lakes, rivers and the ocean on Earth freeze from the top to the bottom such that life is able to survive at the bottom. This is just one example of why water is commonly said to be the matrix of life [1, 2].

Earth is (so far) the only planet where water was found in all three phases: solid, liquid and gas. Antarctica is covered with solid ice, while the oceans are filled with liquid water and the atmosphere contains water in the gas phase. Although these phases have different properties, they all have in common that they are built from water molecules, as depicted in Figure 1.1. A single water molecule consists of two hydrogen atoms and a single oxygen. Multiple water molecules interact via hydrogen bonds. These hydrogen bonds are of universal importance in chemistry and biochemistry, as many biomolecules and proteins are inactive in the absence of water. One of the most important models remains the water dimer, somehow the smallest drop of water [7, 8]. The water dimer is a system of two water molecules bound by a single hydrogen bond, as shown in the magnifying glass on the right hand panel in Figure 1.1. As it has only one hydrogen bond, the water dimer was chosen as candidate to study the hydrogen bonding in water in this thesis. Thereby, the water dimer can be seen as a model system toward the understanding of complex chemical processes, e. g. in biomolecules that are connected via hydrogen bonds with water molecules.

Hydrogen bonds have been studied in many different molecular systems, such as DNA [9], proteins [10] and water clusters [11]. To gain a better understanding of the influence of solvation on biomolecules, it is important to understand single isolated clusters. First, molecular dimers can be studied individually and, second, one molecule can be added at a time to go toward larger cluster systems to bridge the gap between single isolated molecules and molecules in solvation. This can be done by using supersonic molecular beams that create clusters of various sizes at low internal temperatures of a few Kelvin [12–14]. The compounds of a supersonic cluster beam, i.e. different cluster sizes, can be controlled by the amount and composition of the sample prior to the supersonic expansion. This is influenced by the temperature and pressure of the sample [15] and the nozzle shape [15]. All of these factors lead to a different composition of molecular clusters

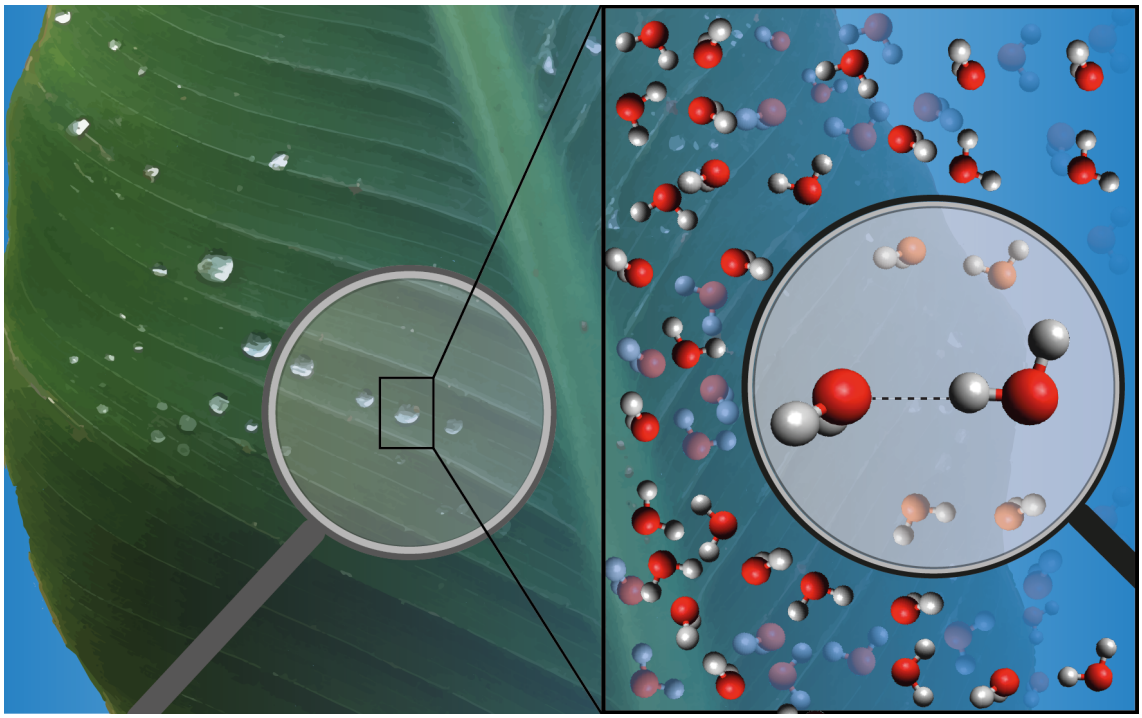

Figure 1.1: Water in nature: A water droplet on a leaf consists of many water molecules building a network of water clusters. A single water dimer is shown in the magnifying glass on the right.

in the gas phase.

Even when the above-mentioned factors are carefully controlled, there will always be more than one cluster size in a supersonic beam, which leads to a higher complexity of the experimental results and low concentrations of specific species. The mentioned rotationally cold samples can only be achieved using carrier gases, which are causing unwanted background and decreasing the signal-to-noise ratio. Molecular beams with a mixture of molecules require long measurement times due to the small experimental event rates and are only feasible if the molecule under study can be disentangled.

Therefore, additional methods like spatial separation can be used to avoid unwanted background from the carrier gas and to achieve a purer molecular beam of a single cluster size, such as an electrostatic deflector [16]. The electrostatic deflector is based on the Stern-Gerlach experiment [17, 18] and uses an inhomogeneous electric field to deflect molecules according to their effective dipole-moment-to-mass ratio, as depicted in Figure 1.2 for water clusters and water dimer and demonstrated in chapter 3. This can lead to a separation of different compounds, such as clusters [19], conformers [20, 21], nuclear spin states [22], but also different rotational states of the same molecule [23].

For a sufficient control of molecules one needs to accurately address the molecular properties. While most molecules are described in a simplified way using only separated degrees of freedom [24], this description does not apply to non-rigid molecules. In particular hydrogen bonded clusters show coupled degrees of freedom and large amplitude

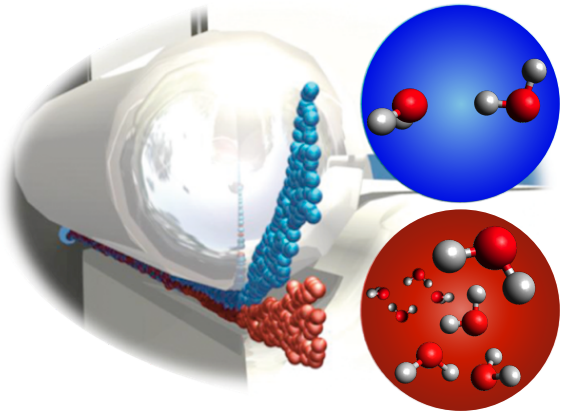

Figure 1.2: Spatial separation of water clusters using an electrostatic deflector leads to a larger deflection of water dimers (blue) than water clusters (red).

motions. Various forms of large amplitude motions, such as internal rotation, intra- and intermolecular vibrations, have been investigated spectroscopically [25–29]. Such dynamics are relevant to molecular properties, e. g. the dipole moment, polarizability, and the first and second hyperpolarizabilities [30] and chemical reactions.

Also the water dimer has been investigated using various spectroscopical methods [7, 8] and has been identified as a non-rigid molecule with intramolecular motions, large amplitude intermolecular vibrations [8, 31] and tunneling effects. These motions cause a splitting and shifting of rotational states, as compared to a rigid molecule [32, 33]. As these vibrational modes can not be sufficiently cooled during the supersonic expansion process, these processes must be taken properly into account, when investigating the deflection behavior of the water dimer in an electric field.

As a full-dimensional description of molecules is often complex, an adiabatic approach is one of the most extensively used methods to reduce the dimensionality of complex systems by separating fast from slow degrees of freedom. Originally, the Born-Oppenheimer approximation was introduced to separate fast electronic from slow nuclear motion [34], but was adapted for separating different kinds of fast and slow molecular motions [35–43]. Therefore, this approach will be used in chapter 4 to investigate the importance of large amplitude motions onto the deflection behavior of the water dimer in an electric field.

The above-mentioned and other dynamical processes, such as the proton transfer, were modeled using potential energy surface (PES) of the neutral and ionized water dimer [8, 44–50] and larger water clusters [51, 52]. For instance, photochemical and photophysical processes, such as ionization and dissociation, are occurring in the Earth's atmosphere through the interaction with sunlight [53]. These processes can be studied in the laboratory by using lasers of various wavelengths and intensities. Different processes that can be triggered in molecules are shown in Figure 1.3. Starting with intensities of about 10^{12} W/cm^2, molecules can be controlled, e. g. molecules can be aligned along the laser polarization axes. By increasing the laser intensity, the molecular potential

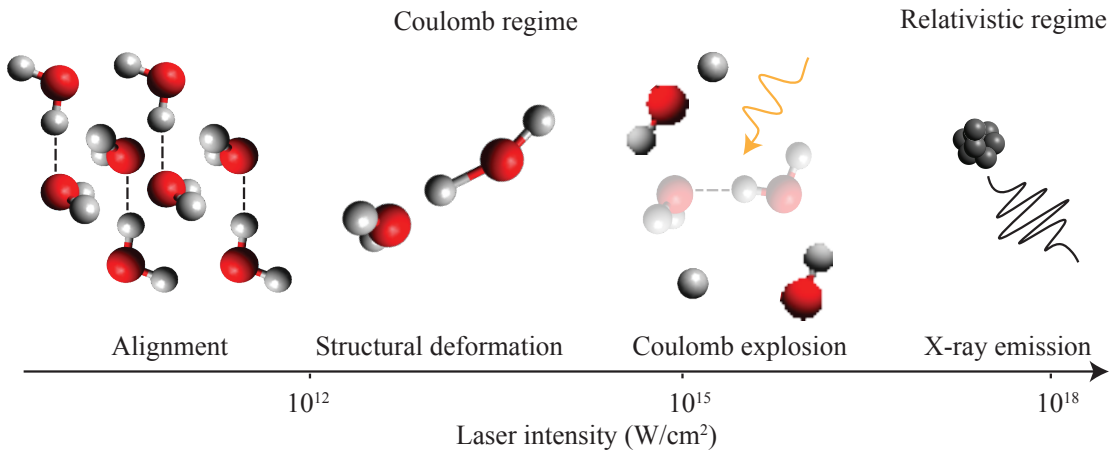

Figure 1.3: Behavior of molecules in laser fields of increasing laser intensity [55].

energy surface and, thus, the geometrical structure of the molecule are deformed. Going further toward higher laser intensities, ionization leads to a formation of molecular ions, including a single or several charges. In case of a multiply charged molecule, Coulombic repulsion leads to a Coulomb explosion and molecular fragments are ejected. In the relativistic regime, starting from intensities of 1 EW/cm^2, a plasma is produced and the plasma electrons are accelerated. This leads to an emission of bright X-rays in the range of (0.1-10) keV, which can be used as a light-source, as is done at the LUX beamline [54].

Different laser wavelengths have been used to address various properties of the water dimer. With microwave radiation, the structure of hydrogen bonded dimers was investigated [56–58], while its dissociation energy [59] and vibration-rotation tunnelling effects [60] were determined using laser light in the infrared (IR) and far-IR regime. Atmospheric processes, such as global warming, were investigated using laser light in the visible region simulating the interaction with sunlight [61, 62]. After photoionization in the VUV vacuum ultraviolet (VUV) [63], IR [64] or soft X-ray [65] regime, mass spectra of molecular beams that contain water clusters are mainly dominated by protonated water clusters, which arise from intermolecular charge transfer after ionization followed by fragmentation [63]. A combination of IR and X-ray in a pump probe experiment was theoretically proposed to further improve the knowledge of the intermolecular charge transfer [66], also called proton transfer. An unprotonated-water fragmentation channel $H_2O^+ + H_2O^+$ from the water dimer was reported using soft X-ray [67]. In the framework of this thesis, the fragmentation products of water dimers will be investigated using strong-field ionization, as described in chapter 5.

1.1 Outline

The goal of this thesis is to understand the photophysics and photochemistry of water dimers, including hydrogen bond formation and breaking, dissociation and fragmentation

processes. We will demonstrate the production of pure molecular beams of water dimer, utilizing a supersonic expansion [13, 14, 19] and an inhomogeneous electric field [16]. This is a prerequisite to study photofragmentation products by strong-field ionization with a velocity map imaging spectrometer [68–70].

In chapter 2, the basics about the used experimental methods are explained. This includes the supersonic expansion, the Stark deflection of a molecule and strong-field ionization processes. In addition, the water dimer will be introduced. Its equilibrium geometry, vibrational motions and nuclear spin states are described, all of which play important roles in the calculations of the Stark energies of the non-rigid water dimer.

The chapter 3 covers the production of the pure water dimer sample and the deflection of water clusters. A first indication of the photofragmentation of the water dimer will be investigated and a rigid-rotor approximation will be used to model the Stark interaction and the resulting deflection behavior to prove the deflected sample was indeed the water dimer.

As the water dimer is a non-rigid molecule, the inclusion of large amplitude motions of the intermolecular vibrations is incorporated in chapter 4 in two different ways. First, in Section 4.1, a simple approach will be used to describe each of the important intermolecular vibrations as independent non-interacting rotations. The averaged electric dipole moment will be calculated and used to describe each motion as a rigid water dimer with a different dipole moment to estimate its influence on the deflection in an electric field. Second, in Section 4.2, the Born-Oppenheimer approximation will be used to simulate the Stark interaction and resulting deflection behavior of the non-rigid water dimer, again neglecting the interaction and transitions of different states. The deflection behavior will be compared to the rigid-rotor approximation.

The photofragmentation of the water dimer after strong-field ionization will be investigated experimentally in chapter 5. Using a velocity map imaging technique and a pure sample of water dimers, a slicing method will be demonstrated to improve the resolution of the experiment. With this method, new fragmentation pathways following single and double ionization were observed, the branching ratios estimated, the anisotropy parameter β of the fragments and the kinetic energy releases of the Coulomb explosion channels obtained.

Finally, future experiments to study hydrogen bonding in water dimers by using soft X-rays and a Photoelectron-Photoion-Photoion coincidence spectrometer and how to go toward larger systems, such as biomolecules in liquid water, to investigate solvation dynamics will be discussed in chapter 6.

2 Fundamental Concepts

In this chapter, the atomic geometry of small water clusters is discussed and the fundamental aspects of the water dimer, such as its floppiness, are explained in detail. An overview of the experiments used in the framework of this thesis in order to investigate molecular clusters is given. This includes the creation of a pure supersonic molecular sample with an inhomogeneous electric field and the usage of an intense laser pulse to ionize and detect molecular samples.

2.1 The Water Dimer

The water dimer has a high concentration in the earth atmosphere [71, 72] and, thus, plays an important role in many atmospheric processes [73, 74], such as in the water continuum absorption [75–77] and in chemical reactions [78–80]. As the water dimer consists of two water monomers that are connected via one hydrogen bond and because of its simple equilibrium geometry, which is discussed in the next subsection 2.1.1, the water dimer is a good candidate to study hydrogen bonding. Nevertheless, the non-rigidity of the water dimer makes its investigation challenging, which also influences chemical, atmospheric and climate processes [81]. The major non-rigid effects of the water dimer are introduced in subsection 2.1.2, which cause a splitting of the water dimer into several nuclear spin isomers and are described in subsection 2.1.3. Also fragmentation products can be explained due to molecular dynamics, such as the proton transfer, which is described in subsection 2.1.4.

2.1.1 The Equilibrium Geometry

The geometry of the water dimer determines its electrical properties such as the polarizability and the electric dipole moment (EDM). The equilibrium geometry of the water dimer was investigated in many studies [57, 58, 82–85]. In general, the water dimer consists of two water monomers, where one monomer acts as the hydrogen bond donor (d) and the other monomer as an acceptor (a) molecule, bound by a hydrogen bond, see Figure 2.1. Each water molecule consists of 3 atoms, two hydrogen and one oxygen atom. The experimentally derived values for the distances R_{OO} between the two oxygens, the distance between the oxygen and hydrogen atoms R_{OH} and the angles $\theta_{\mathrm{a}}, \theta_{\mathrm{d}}, \psi = \psi_{\mathrm{a}} = \psi_{\mathrm{d}}, \chi_{\mathrm{d}}$ of the equilibrium water dimer are given in Table 2.1.

2.1.2 Non-Rigidity

The water dimer is a non-rigid molecule with hydrogen bond vibrations [86] that are important for modeling of the electric properties of the water dimer. The water dimer

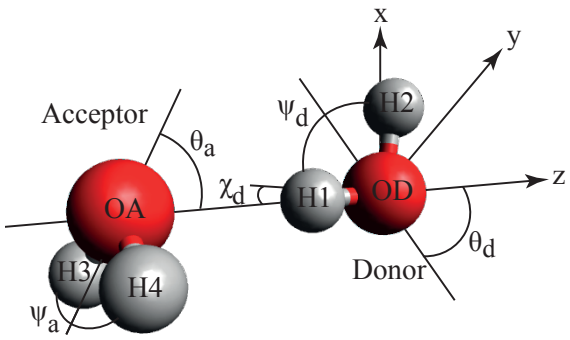

Figure 2.1: The equilibrium geometry of the water dimer in C_S symmetry and the angles $\theta_a, \theta_d, \chi_d$.

$\theta_a(^\circ)$	$\theta_d(^\circ)$	$\psi(^\circ)$	$\chi_d(^\circ)$	$r_{OH1,2}$(pm)	$R_{OH3,4}$ (pm)	R_{OO} (pm)
57	51	104.5	0	95.8	95	298

Table 2.1: Equilibrium angles and distances of the water dimer taken from [57, 58].

has twelve vibrational modes, which can be separated into six intermolecular and six intramolecular vibrations [86]. As the major contributors to the normal vibrations of the water dimer are the intermolecular vibrations with the smallest vibrational frequencies [87], this thesis focuses on these motions, which are shown in Figure 2.2. Six independent vibrational modes were found [86] and their frequencies measured [87–90].

The intermolecular vibrations can be described by applying rotations or a stretching to the acceptor water and donor water inside the water dimer. While the oxygen-oxygen (OO)-Stretch can be described as a stretching of the hydrogen bond between the donor and acceptor, the other five motions can be described by the change of six Euler angles $\alpha_{D,A}, \beta_{D,A}, \gamma_{D,A}$ as rotations around the monomers centre of mass and the axis $\lambda = z, y, x$, respectively. The torsional motion can be described by the angle $\delta = \alpha_D - \alpha_A$, with α_D being a rotation around the z-axis of the donor and α_A a rotation around the z-axis of the acceptor. The acceptor twist and the out-of-plane bend are described by rotations γ_A and γ_D around the x-axis of the acceptor and donor water, respectively. The acceptor wag β_A and in-plane bend β_D are rotations around the y-axis of the acceptor and donor, respectively. A rotation of $\alpha_D = \alpha_A$ describes an overall rotation around the water-dimer z-axis. In chapter 4, this is done by using the water dimer in its equilibrium structure from subsection 2.1.1 as a starting configuration and assuming the water monomers inside the water dimer to be rigid.

2.1.3 Nuclear-Spin Isomers

Symmetric molecules with non-zero nuclear spins exist with different nuclear-spin isomers, due to the indistinguishability of protons with a different spin orientation. This is also valid for the water dimer. Assuming the water dimer to be rigid, it belongs to the point

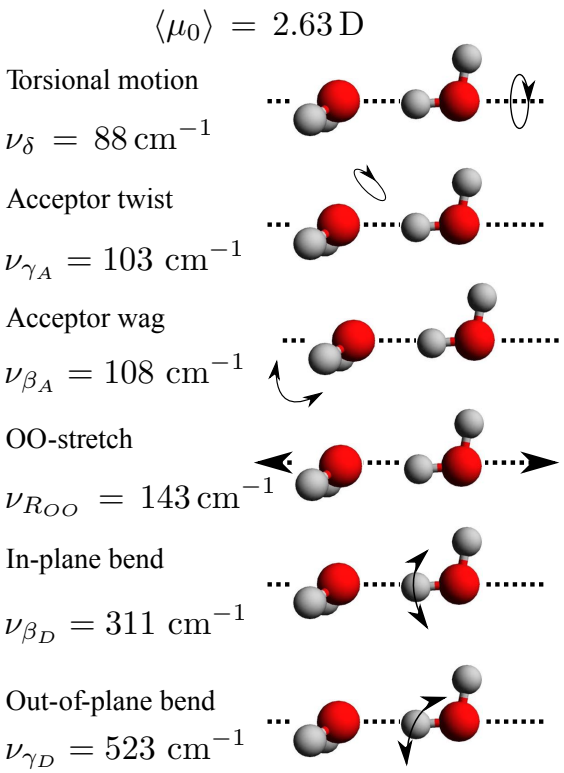

Figure 2.2: The six independent vibrational modes following the naming scheme of [86] with their frequencies taken from [87].

group symmetry $C_S(M)$ and can be separated into states with nuclear spin statistical weights (NSSW) $A' : A''$ of 16 : 16 [91]. Throughout this thesis A' is called *para* and A'' *ortho*. The next higher level of symmetry would be an acceptor tunneling or acceptor switching, which is a rotation around its C_2 axis. This belongs to a molecular symmetry group (MSG) of G_4 with a NSSW $B_1 : A_1$ of 12 : 4 and $B_2 : A_2$ of 12 : 4. Taking more vibrational modes into account the water dimer belongs to a MSG of G_{16}. and the states split into several sublevels. These can be assigned to spin states $A_1^\pm, B_1^\pm, A_2^\pm, B_2^\pm$ and $E^\pm$ with a NSSW of $1, 0, 3, 6$ and 3 [33], respectively. A donor tunneling or bifurcation is also possible and leads to a shift of the energy levels. An example of the splitting of the $\mathrm{J} = 0, \mathrm{K} = 0$ state and the energy-level-diagram of the non-rigid states are shown in Figure 2.3.

2.1.4 Proton Transfer and Fragmentation Products of the Water Dimer

The proton transfer is an intermolecular charge transfer across a hydrogen bond, as depicted in Figure 2.4 for a water-dimer cation. The hydrogen $H1$ from the donor water is moving closer to the oxygen $O2$ of the acceptor water and a new hydrogen bond between $O2$ and $H1$ and a H_3O^+OH complex is formed. The proton transfer can occur after ionization of a molecule, leading to fragments of protonated clusters [51, 63]. For this

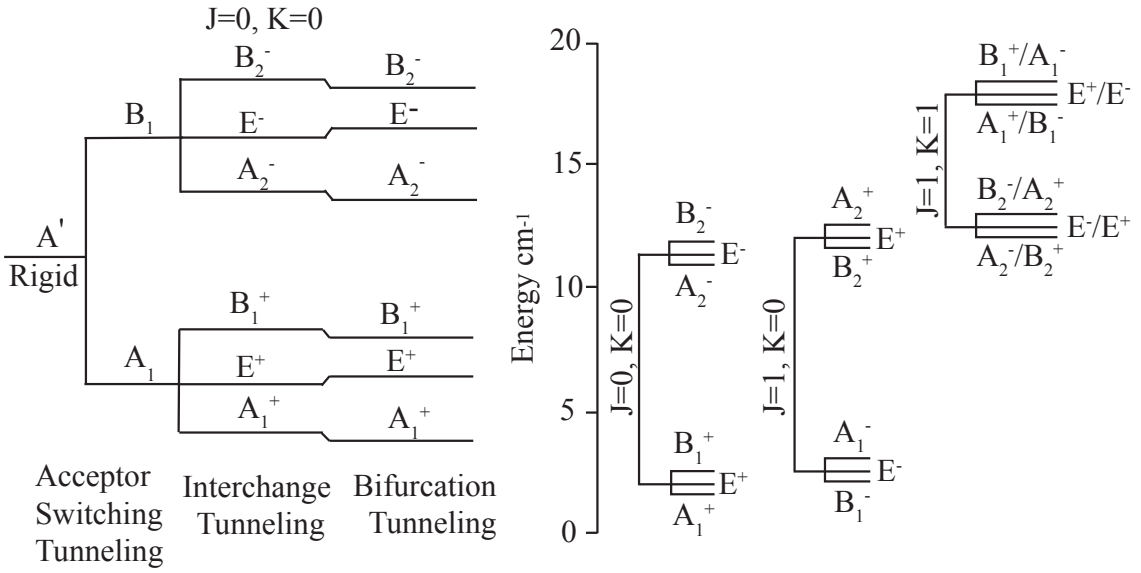

Figure 2.3: Experimental values and nuclear spin state assignment taking acceptor switching, interchange tunneling and bifurcation tunneling into account [32].

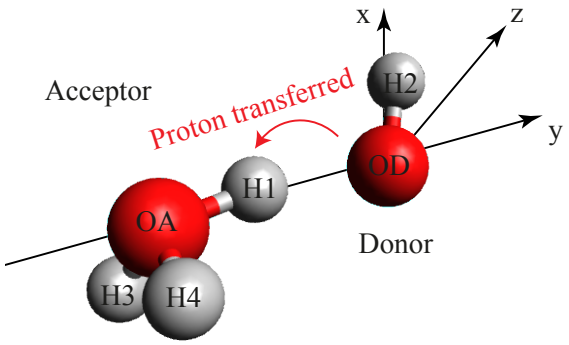

Figure 2.4: Water dimer after a proton transfer has formed the complex of H_3O^+OH.

reason, mass spectra of molecular beams containing water are dominated by protonated water clusters [63–65, 92, 93]. For a proton transfer inside the water dimer, an electron must overcome an ionization potential (IP) of 11.2 eV [94] to create a water-dimer cation. Depending on the ionization state, different complexes can be formed, leading to different fragmentation products. The water-dimer cation has two low-lying electronic states $^2A''$ and $^2A'$ with IPs of 12.1 eV and 13.2 eV [95], respectively. They form different complexes and fragmentation products, as shown in Figure 2.5. It was predicted theoretically [96] that an ionization into the water-dimer cationic ground state $^2A''$ leads to a complex formation of $(H_3O^+)OH$ and a following fragmentation into $H_3O^+ + OH$. While two complexes $(H_2O - OH_2)^+$ and $H_2O^+ - H_2O$ can be formed after ionization into the first excited state $^2A'$. Both cases lead to a fragmentation into $H_2O^+ + H_2O$. These neutral dissociation fragments were observed experimentally as well [92, 97, 98]. In addition, Coulomb explosion (CE) channels of $H_2O^+ + H_2O^+$ and $H_3O^+ + OH^+$ were found to occur using soft X-ray and IR ionization [67, 99]. Further, theoretical studies have shown that these

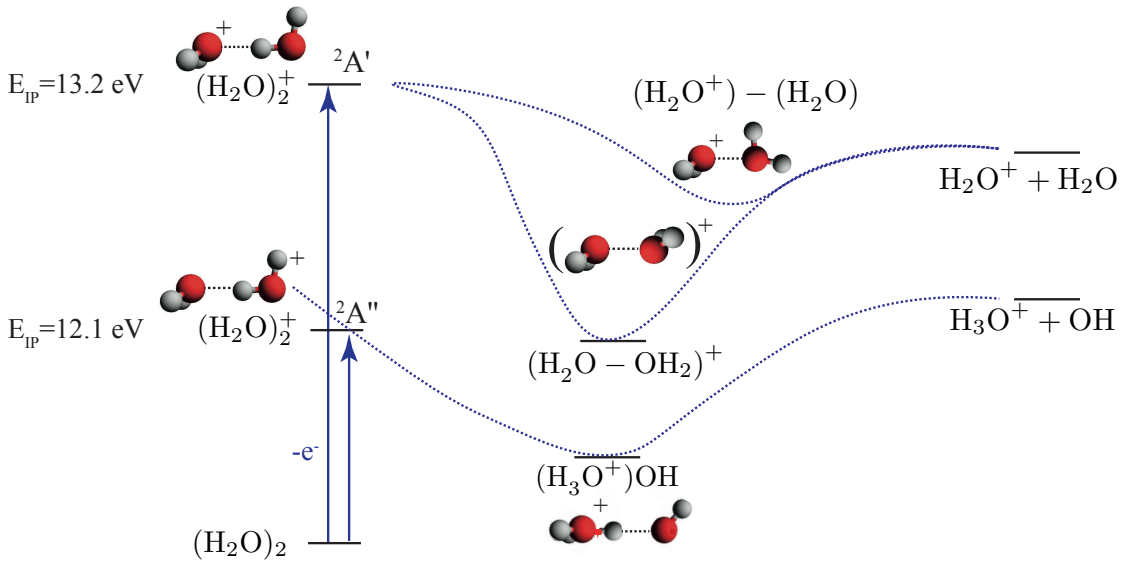

Figure 2.5: Theoretically predicted potential energy surface and formed complexes after ionization of the water dimer [96].

fragmentation products could also arise from other water-dimer cationic states [44, 95, 100–102].

2.2 Small Water Clusters $n = 3 - 7$

The equilibrium geometry of the water dimer has been investigated extensively in experiment and theory, leading toward one optimized geometry [57, 58, 82–85], as shown in subsection 2.1.1. Water clusters instead exist as different conformers with several possibilities of their geometry [82]. These conformers behave differently in electrical or laser fields. The chosen geometries to describe these water clusters throughout this thesis are shown in Figure 2.6. The water trimer, water tetramer and water pentamer have been shown to have a cyclic equilibrium structure [82, 106–108]. While the water hexamer exists most-likely as three conformers with a cage-, prism and book-like structure [109]. The water heptamer has been described in several conformational structures. Throughout this thesis, the two conformers shown in Figure 2.6 are used following the naming scheme of [104].

2.3 Experimental Methods

This section covers a description of the experimental methods used in this thesis, such as supersonic expansion, the Stark effect and time-of-flight mass spectrometry. The interaction of strong electric fields with molecules and the following dissociation processes are discussed.

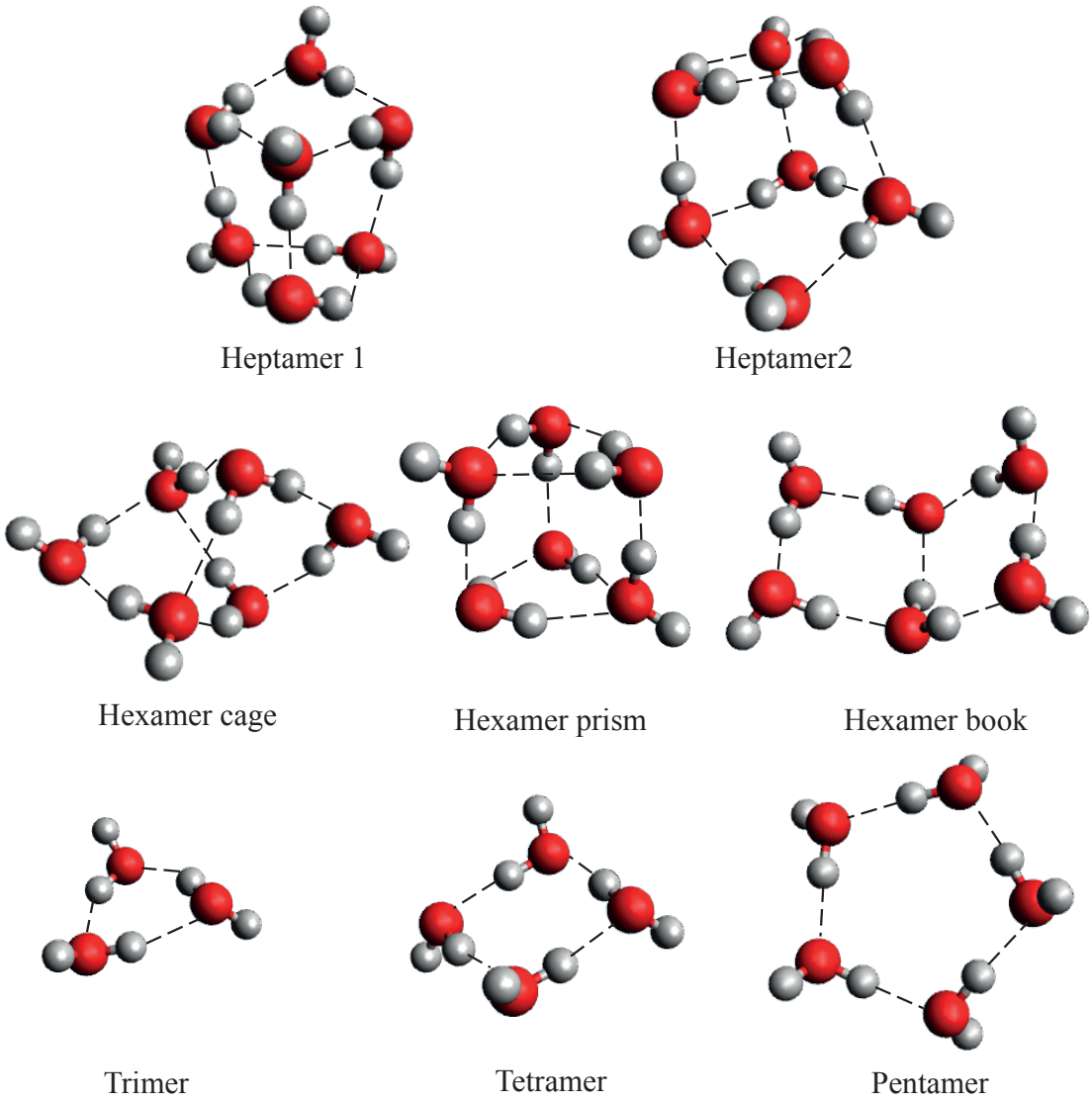

Figure 2.6: Possible geometries of small water clusters with the cartesian coordinates taken from [103–105].

2.3.1 Supersonic Molecular Beams

A widely used method to create a molecular beam is the supersonic expansion technique, where gas is expanded from a high pressure region through a small orifice into a region of low pressure. As the diameter of the orifice is larger than the mean free path of the molecules inside the high-pressure reservoir, many collisions are taking place while the molecules escape through the hole, thereby leading to an adiabatic cooling of the internal degrees of freedom. The internal energy of the molecules is transferred into kinetic energy and leads to a direct flow of cold molecules in the forward direction with a narrow velocity spread [110]. As the speed of the molecular beam exceeds the local speed of sound, it is called a supersonic molecular beam. The flow velocity of the molecular beam is defined

by the mass m and the temperature T of the carrier gas

$$v = \sqrt{\frac{5k_BT}{m}} \tag{2.1}$$

with the Boltzmann constant k_B [111].

Using a pulsed valve and a noble carrier gas, the translational temperature, which is defined by the velocity distribution of the molecular beam, can be cooled to below 1 K [13, 14] with a density of 10^{13} molecules/cm^3 [112]. While the rotational temperature is cooled down to below 1 K, the vibrational states remain mainly unchanged and a typical vibrational temperature of a few tens of Kelvin [12] can be achieved. At the edges of the molecular beam the cooling is less efficient. Therefore, a skimmer can be used to select the coldest part of the molecular beam with the highest beam density. This technique can be used to produce a cold molecular beam of clusters [113]. Nevertheless, the cooling of clusters is less efficient, as the binding energy of the cluster formation is transferred to a third molecule and leads to a heating of the molecular beam.

Clustering is a complex process and is not fully understood, yet. In general, the starting point for clustering is the formation of the dimer, which needs a three-body collision due to energy and momentum conservation. An empirical scaling law for rare gases and metals was found [15, 114, 115] and successfully tested for gas mixtures [116]. The reduced scaling parameter Γ^* is describing how changing flow fields are affecting the clustering process in a supersonic beam and is defined as

$$\Gamma^* = \frac{p_0 \cdot d_{eq}^{0.85}}{T_0^{2.29}} K_{ch}, \tag{2.2}$$

where T_0 is the initial temperature of the gas, p_0 the initial stagnation pressure, $d_{eq} = 0.74\frac{d}{\tan\alpha}$ the equivalent diameter of the nozzle, α the expansion half angle and d the nozzle diameter, and K_{ch} a parameter that depends on the type of gas [117]. The reduced scaling parameter Γ^* is separated in three regions

$$\Gamma^* < 200 \text{ no clustering} \tag{2.3}$$

$$200 < \Gamma^* < 1000 \text{ cluster with less than 100 atoms per cluster} \tag{2.4}$$

$$1000 < \Gamma^* \text{ cluster with more than 100 atoms per cluster} \tag{2.5}$$

of a different mean cluster size $\langle N \rangle$, which is defined as the mean number of atoms per cluster N.

Depending on the mean cluster size, the cluster distributions follow different functional forms [118]. For a cluster beam with a small mean cluster size, the distribution follows roughly an exponential decay $\sim e^{-N}$ [65], while for a large cluster regime a log-normal distribution $\sim e^{-\frac{(\ln N-\mu)^2}{2\sigma^2}}$, with μ the logarithm of the geometric mean and σ the logarithm of

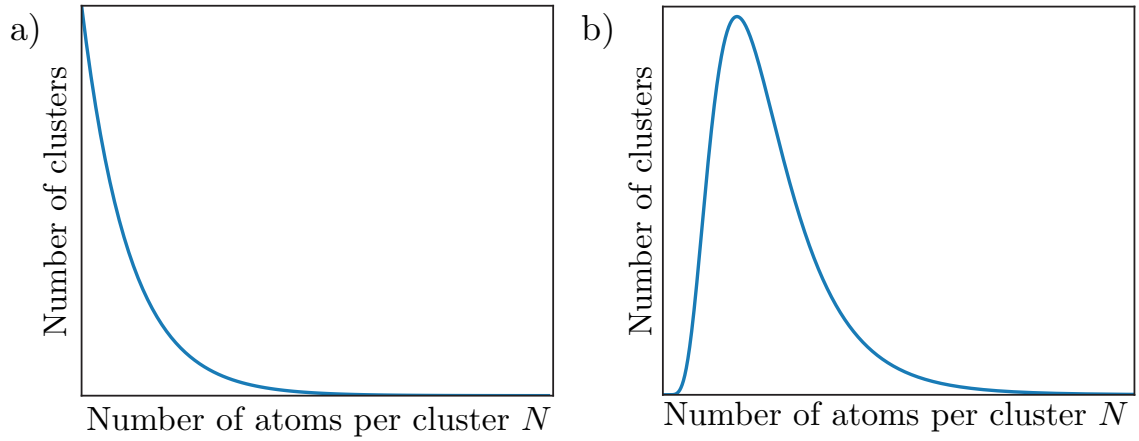

Figure 2.7: Cluster distribution of cluster beams in the a) small and b) large cluster regime.

the geometric standard deviation of the cluster distribution [119, 120]. These distributions are shown in Figure 2.7. In the intermediate regime, a mixture of the two distributions are measured [118].

Other studies have shown that the number of three-body collisions can be increased with decreasing initial temperature and increasing number density, initial stagnation pressure and nozzle diameter d [115, 121, 122]. For large water and ammonia clusters, the scaling law was adapted by taking the different number of degrees of freedom into account [119]. Moreover, carrier gases and the nozzle shape [15] also have an influence on the cluster formation. An overview can therefore be found in [123]. In short, carrier gases with larger masses are slower and provide more time for the aggregation process and larger clusters can be formed. The conical nozzle provides a cluster beam with a larger averaged cluster size. Nevertheless, the molecular beam most-likely contains more than one cluster size and additional techniques are needed to separate different molecular clusters, as discussed in the next subsection 2.3.2.

2.3.2 Size Separation

The electrostatic deflector is a tool to spatially separate different molecular species and clusters according to the difference of their effective dipole moments. A detailed description can be found in [16]. The electrostatic deflector was used elsewhere to separate different conformers [20, 21], nuclear spin isomers [22] and molecular clusters [19, 124, 125]. The general working principle of such a deflector is to shift the energy of a molecular system of interest by interacting the system with an external inhomogeneous electric field produced by a number of electrodes. Molecules in the electric field experience a force $\overrightarrow{F}$

$$\overrightarrow{F} = \mu_{\text{eff}}(\epsilon)\overrightarrow{\nabla_\epsilon} \tag{2.6}$$

proportional to the effective dipole moment μ_{eff}

$$\mu_{\text{eff}} = -\frac{\partial E}{\partial \epsilon}, \tag{2.7}$$

causing a spatial motion of the molecule, with energy E of a single state of a molecule. This effect, known as the Stark effect, can be described by a Hamiltonian H_{Stark}

$$H_{\text{Stark}} = -\overrightarrow{\mu} \cdot \overrightarrow{\epsilon} = -\epsilon_z \sum_{g=x,y,z} \mu_g \Phi_{Z_g}, \tag{2.8}$$

with the dipole moment $\overrightarrow{\mu}$, the electric field vector $\overrightarrow{\epsilon}$, the dipole moment components μ_g along the molecule-fixed axes x, y, z, the direction cosines Φ_{Z_g} of the x, y, z axes in reference to the space-fixed axes X, Y, Z of the laboratory-frame and the electric field ϵ_z along the laboratory Z axis. The time-independent Schrödinger equation, describing the coupled system of molecular clusters and the electrostatic deflector,

$$E\Psi = H\Psi, \tag{2.9}$$

with the wave function Ψ and the Hamiltonian operator H in the center-of-mass frame, are solved by replacing H with the Hamiltonian

$$H_{\text{rot},\epsilon} = H_{\text{rigid}} + H_d + H_{\text{Stark}}, \tag{2.10}$$

assuming the molecules to be rigid with a compensation factor H_d for non-rigidity including centrifugal distortions. The eigenvalues can then be calculated by diagonalizing the Hamiltonian in the basis of the asymmetric top wave functions using the CMISTARK software package [126].

As a supersonic molecular beam contains many clusters, the Stark effect can be used to spatially separate clusters according to their effective dipole moment-to-mass ratios. The calculated Stark energy and the effective dipole moments μ_{eff} for the rotational ground state $J = 0$ of water clusters up to $n = 7$ are shown in Figure 2.8 as a function of the applied electric field. The reported minimum energy structures, shown in Figure 2.6 of Section 2.2, were used to calculate Stark energies of water clusters. The rotational constants, dipole moments and centrifugal distortion constants that are used in these simulations are taken from the literature [104–109, 127–131] and summarized in Table A.1 of Section A.

All water clusters in the ground state show a decrease of energy with increasing electric field strengths, also called high-field seeking. The molecules are deflected toward larger electric field strength and downwards on the y-axis in the experimental setup, see Figure 2.8 b). The water hexamer in prism and book-like structure experience the biggest energy shift followed by the water dimer. Assuming the water clusters to be in the ground state, the water hexamer would be expected to have the largest spatial shift. In the experiment, more states are populated and, thus, a change of the measured spatial

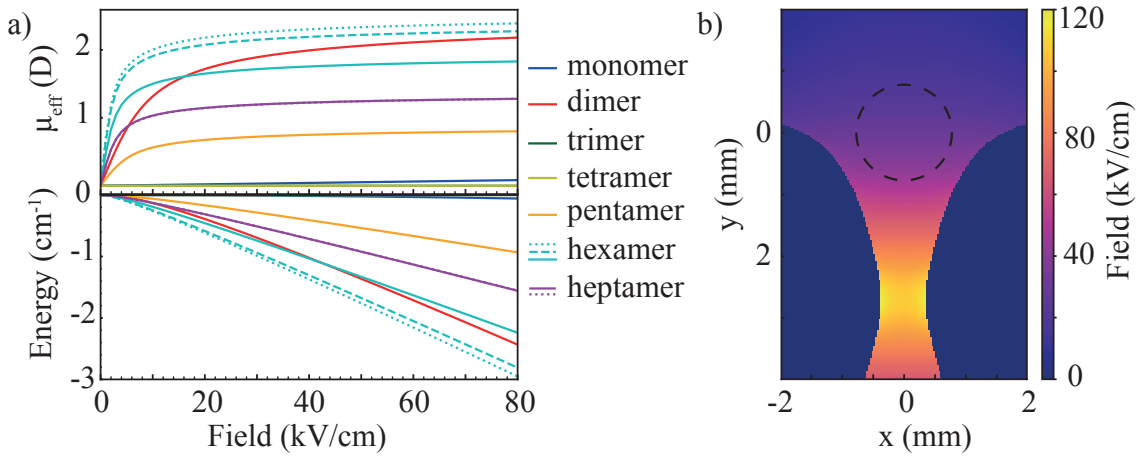

Figure 2.8: a) Stark Energy and effective dipole moment μ_{eff} in dependence of the electric field strength of the ground state of water (blue), water dimer (red), water trimer (green), water tetramer (yellow), water pentamer (orange), water hexamer (cyan) in cage- (solid), prism- (dotted) and book-like (dashed) structure and water heptamer (magenta) conformer 1 (solid) and conformer 2 (dotted). b) The simulated electric field strength inside the electrostatic deflector. The cross-sections of the pair of electrodes are shown in dark blue. The molecular beam is indicated by the black dashed circle.

molecular beam profiles are expected from the simulated ground state. As the dipole moments of the water trimer and the water tetramer are zero, their energy stays constant in the electric field.

Non-Rigid Molecules in an Electric Field

The above-mentioned method is used for the approximation of a rigid molecule, but the water dimer is a non-rigid molecule with large amplitude motions, which needs to be included in the simulations. In this thesis, an adiabatic approximation was used to separate slow translational motions from fast rovibrational motions solving the time-dependent Schrödinger equation (TDSE)

$$i\hbar\frac{\partial\Psi(\theta,R,t)}{\partial t} = H\Psi(\theta,R,t) \tag{2.11}$$

with the total wave function $\Psi(\theta,R,t)$ depending on the time, the rotational and translational coordinates. The Hamiltonian H is describing the motion of the nuclei in a molecular system

$$H = \underbrace{T_{rot}(\theta) + H_{Stark}(\theta,R)}_{H_q} + T_{tr}(R), \tag{2.12}$$

which can be separated into a kinetic energy operator T_{rot}, translational energy operator T_{tr} and the Stark interaction with the electrical field $H_{Stark} = -\mu(\theta)\epsilon(R)$ with the Euler angles

θ, which are defining the orientation of the molecules, and R the Cartesian coordinates in the center of mass of the polar molecule with respect to the space-fixed laboratory frame. One can separate the translational from the rovibrational motion by using the adiabatic theorem and the Ansatz

$$\Psi(\theta, R, t) = \sum_k \kappa_k(R, t)\phi_k(\theta; R) \tag{2.13}$$

with the adiabatic basis ϕ_k, where "; " denotes a parametric dependence, and the time-dependent wave function κ_k. The adiabatic basis $\phi_k(\theta; R)$ solves then the time-independent Schrödinger equation

$$H_q\phi_k(\theta; R) = E_k(R)\phi_k(\theta; R), \tag{2.14}$$

with a discrete rovibrational energy spectrum $E_k(R)$. The translational Schrödinger equation can be solved by taking the classical limit into account and one obtains

$$m\frac{\partial^2 R}{\partial t^2} = -\nabla_R E. \tag{2.15}$$

The electric field is assumed to be a slow perturbation on the rotational Hamiltonian, such that the two motions are assumed to be completely decoupled.

This approach is implemented in RichMol [132] and was used in Section 4.2 to calculate the rotational energies and eigenfunctions of the water dimer in an external electric field taking intermolecular vibrations into account.

2.3.3 Detection

The size of molecules is in the range of a few hundred picometer up to ten nanometers [133] and are, thus, not visible by eye or optical microscopes. Instead, spectroscopy, diffraction or mass spectrometry are often used to detect molecules indirectly. In this thesis, a time-of-flight (TOF) mass spectrum (MS) was used in combination with a velocity map image (VMI) technique to measure strong-field ionization (SFI) effects.

Strong-field dissociative ionization processes of molecules can be studied using an intense femtosecond laser pulse. In the case of an infrared laser with a wavelength around 800 nm, the photon energy of a single photon is below the ionization energy. Thus, the molecule cannot be vertical ionized by a single photon, but other ionization pathways can occur. This includes three major ionization processes: multiphoton, tunnel and over-the-barrier ionization [134]. An indicator to separate these regimes is the Keldysh parameter [135]

$$\gamma = \sqrt{\frac{E_i}{2U_p}}, \text{ with } U_p = \frac{I}{4\omega^2}. \tag{2.16}$$

U_p is the ponderomotive potential, E_i the ionization energy, ω the angular frequency of the

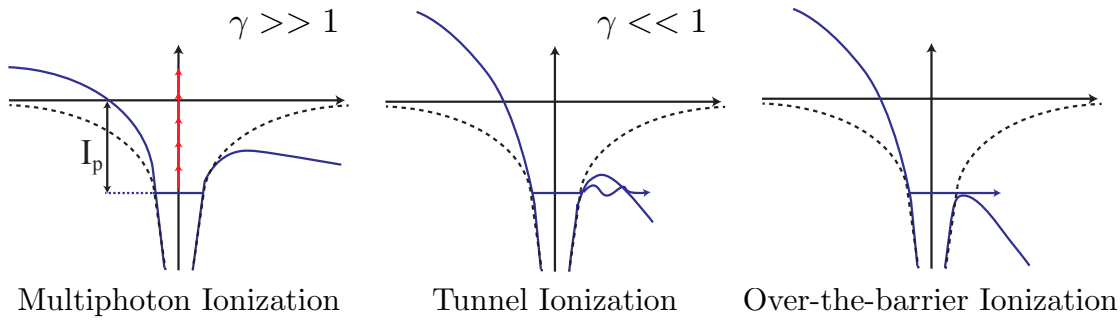

Figure 2.9: Ionization processes in a molecule

laser field and I the laser intensity. The Keldysh parameter is only clearly defined for the two regions of $\gamma \gg 1$ and $\gamma \ll 1$. At a low laser intensity and short wavelength/high frequency, ionization occurs through the absorption of many photons simultaneously, which is called the multiphoton regime with $\gamma \gg 1$. For large intensities and low frequencies, the IP is perturbed more than in the multiphoton regime and the electron within the molecule can tunnel through the barrier, which leads to tunnel ionization with $\gamma \ll 1$. At very high field strengths, the electric field suppresses the Coulomb barrier such that the electron can overcome the barrier through the so-called over-the-barrier ionization. These processes are depicted in Figure 2.9. In the intermediate regime $\gamma = 1$, the picture becomes blurry and both tunneling and multiphoton ionization can occur. As many studies are using laser intensities and wavelengths in the intermediate regime, it has become of interest to differentiate multiphoton from tunnel ionization processes differently [136, 137].

The ionization of a molecule simultaneously forms two wave packets: one from the electron and one from the nuclear vibrational wave packet of the molecular ion. While the electron is set free, the vibrational wave packet is moving on its PES to find its energetic minimum. This can lead to dissociative states and the molecule is fragmented into several particles. The different processes inside a diatomic molecule AB are depicted in Figure 2.10. A detailed description of the molecular hydrogen H_2 can be found in [138].

A diatomic molecule AB in the ground state (black curve in Figure 2.10) can reach an excited state in the event of resonant absorption (green). Ionization of the molecule into an ionization state AB^{n+} (blue and purple curve) can be written as

$$AB + h\nu \rightarrow AB^{n+} + ne^{-} \tag{2.17}$$

and can include several number of charges and kicked out electrons n. Both of these processes can lead to a fragmentation of the molecule. Either a dissociation state (red, purple) is reached or the molecule is ionized including several charges and a CE (purple) happens. The potential minimum of the dissociation state lies in the region of large internuclear distances such that it is more favorable to break apart. It forms a neutral B

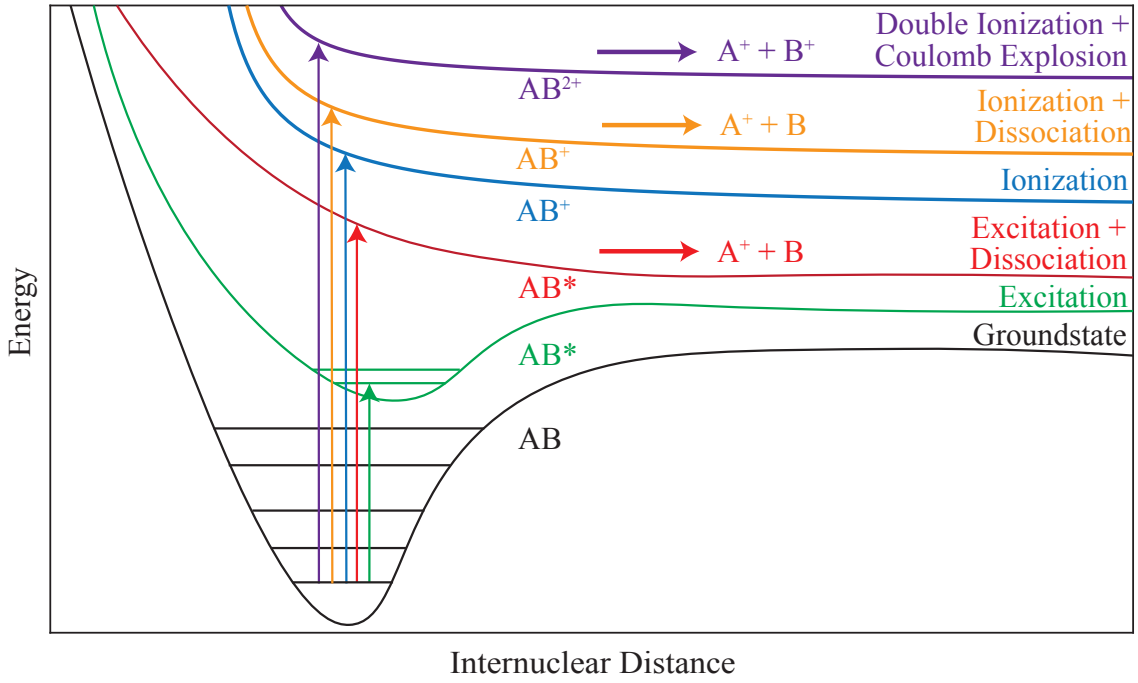

Figure 2.10: Potential energy of a diatomic molecule and the different strong-field processes. The molecule AB in the electronic ground state (black) can go to a stable excited state AB^* (green) or an unstable state with a following dissociation $A^+ + B$ (red). Strong-field ionization into AB^n (blue) or AB^{qn} are also shown, where an ionization with $n = 2$ leads to a Coulomb explosion into $A^+ + B^+$ (purple).

and an ionized fragment A^+

$$AB^* \rightarrow A^+ + B \text{ (neutral dissociation)}, \tag{2.18}$$

which is also called neutral dissociation. A CE occurs instead, when several charges are created inside the ionized molecule as they feel a Coulomb repulsion and the molecule explodes into several charged particles:

$$AB^{2+} \rightarrow A^+ + B^+ \text{ (Coulomb explosion)} \tag{2.19}$$

In all processes that leads to a fragmentation, the excess internal energy of the molecule is released as translational energy of the fragments. The sum of the fragmental energies is called kinetic energy release (KER) and can give some insight into the energetics of the transient molecular ion. Using the diatomic molecular ion as an example again, the KER from a CE looks as follows [139–141]:

$$KER = \frac{p_A^2}{2m_A} + \frac{p_B^2}{2m_B}, \tag{2.20}$$

with p_A, p_B being the momenta and m_A, m_B the masses of the fragments A and B. Assum-

ing a Coulomb explosion of a double ionized parent molecule, the distance of the two charges inside the parent ion can be calculated according to Coulombs law in vacuum

$$R = \frac{1}{4\pi\epsilon_0}\frac{q_A q_B}{KER}, \tag{2.21}$$

with the charges q_A, q_B of the fragmental ions and the electrical permittivity of the free space ϵ_0. Thus, the charge separation distance is given by [139, 142]

$$R \approx \frac{14.4}{KER}. \tag{2.22}$$

The width of the KER distribution represents the probability distribution of the molecule to be in the ground state at its equilibrium bond length.

The KER can be indirectly measured using a TOF-MS . In general, a TOF-MS consists of three electrodes producing a constant electric field ϵ to accelerate ions toward a multi-channel plate (MCP) detector and a field-free drift region with a distance d [143]. As the flight time t of the molecular ion depends on its mass-to-charge ratio m/q, the composition of a molecular beam and the constituents of a fragmentation process can be determined. The relation of the mass-to-charge ratio to the flight time of the ion is then given by

$$\frac{m}{q} = C(t_m - t_0)^2, \text{ with } C = \frac{2\epsilon}{d^2}, \tag{2.23}$$

where the measured flight time t_m has an offset of t_0 to the real time $t = t_m - t_0$. This simplified equation can be used for a calibration of the TOF spectrum by comparing the calculated masses with the actual mass values of a calibration sample or the seeding gas. The calibration is improved by using two calibration masses. One method is to use educated guessing, where two peaks are assumed to correspond to a certain m/q ratio. Therefore, the shortest flight time is often given by the proton and, as second mass, the seeding gas can be used. The obtained spectrum has to be compared to the measured masses such that all peaks are assigned. Also simulating the ion trajectories for a given spectrometer voltage is an option, e. g. with SIMION [144]. The resolution of the spectrometer is given by the width of the arrival times at the detector, caused by a variation of the initial position, timing and kinetic energy at the point of formation of the ions.

Combining the MCP with a phosphor screen and a camera, not only the mass spectra, but also the velocities and, thus, the kinetic energies of the created molecular ions can be measured. Therefore, the voltage ratio of the spectrometer electrodes must be optimized such that ions with the same velocity vector hit the same spot on the MCP detector [68]. The created ions are expanding spherically from the point of creation and form a three-dimensional Newton sphere. Only a projection into two-dimensions can be measured, but the full information can be extracted by a reconstruction of the detected VMI. This

transformation is called Abel transformation.

From the reconstructed VMI one can gain some information about the dependence of the angular distribution $I(\theta)$ on the laser polarization, which is given by the anisotropy parameter β. Originally, it was introduced for electrons [145]

$$I(\theta) = \frac{1}{4\pi}(1 + \beta P_2(\cos\theta)), \tag{2.24}$$

and has been adapted for ions [146]

$$\frac{d\sigma}{d\Omega} = \frac{\sigma}{4\pi}(1 + \beta P_2(\cos\theta)). \tag{2.25}$$

The angular distribution of ions $\frac{d\sigma}{d\Omega}$ is defined via the second Legendre polynomial $P_2(\cos\theta) = \frac{1}{2}(3\cos^2\theta - 1)$ with the angle θ between the fragmented ion and the polarization axes of the laser. The β parameter lies in the range between -1 and 2. It describes the degree of anisotropy of the angular distribution. In the case of $\beta = 0$ the distribution is fully isotropic, while $\beta = -1$ is perpendicular and $\beta = 2$ indicates a parallel distribution in reference to the laser polarization axis.

2.4 Experimental Setup

In this chapter, the experimental setup used in this thesis is discussed. A differential pumping system was used to separate the source, deflection and detection chambers with a vacuum of 10^{-8} mbar, 10^{-10} mbar and 10^{-9} mbar maintained within those chambers, respectively. Only skimmers with diameters of 3.0 mm and 1.5 mm were connecting the different chambers. A schematic drawing of the experimental setup is shown in Figure 2.11.

The source chamber involved a pulsed Even-Lavie valve to create a rotationally-cold water-cluster sample [14] and a skimmer 6.5 cm behind the nozzle. Inside the valve, a filter paper soaked with one droplet of deionized water was placed and heated up to 100° C. With a valve repetition rate of 250 Hz and a valve opening time of 19.5 µs, a molecular beam of water clusters was created using helium as a seeding gas with a pressure of 100 bar.

The molecular beam was skimmed by a second skimmer with a diameter of 1.5 mm to reduce the size of the molecular beam and so reduce the number of collisions with the deflector electrodes, that were placed 4.4 cm behind the second skimmer. An electrostatic deflector with two parallel rods, also called a b-type deflector [147], of 154 mm in length and maximum field strength of 50 kVcm^{-1} was used to spatially separate the water dimer from the seeding gas and other water clusters inside the molecular beam.

A third skimmer 3.6 cm behind the deflector connected the deflection and detection chamber. By optimizing its position, the coldest part of the molecular beam can be selected,

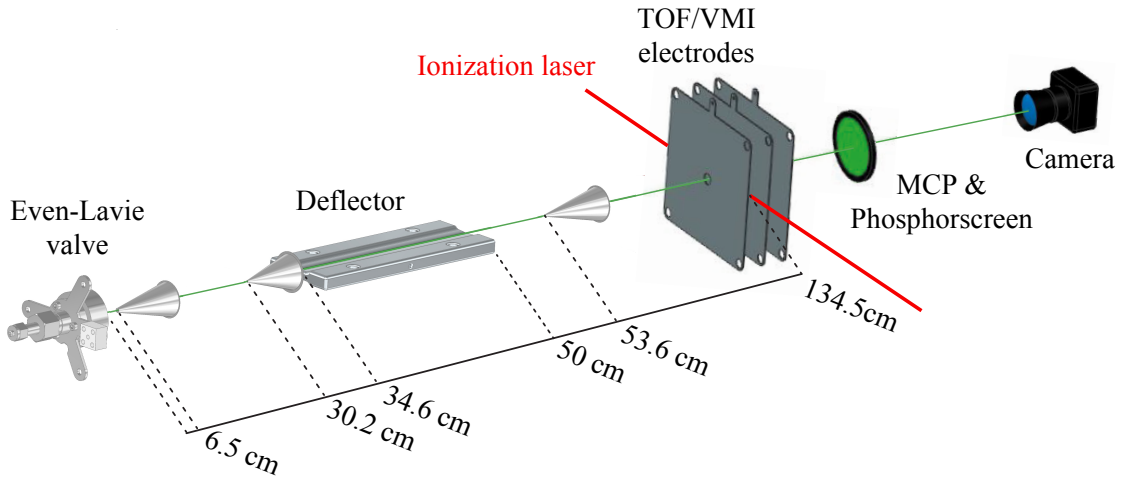

Figure 2.11: Schematic of the general experimental setup consisting of a pulsed valve, a deflector and a time-of-flight mass spectrometer/velocity map imaging spectrometer.

as it is usually the part of the beam that is deflecting the most. In the detection chamber, a VMI that can also be used as a TOF-MS and a MCP detector were placed 134.5 cm downstream from the nozzle. In the center of the TOF-MS, the molecular beam was ionized by a laser pulse with a full width at half maximum (FWHM) of 30 fs, a wavelength centered around 800 nm and a linear laser polarization parallel to the detector. The laser was focussed by a 500 mm focal length lens to a FWHM-spot size of (40 x 40) μm^2 with a pulse energy of around 170 µJ. The molecules were strong-field ionized and the created ions were accelerated toward the MCP detector, which was combined with a phosphor screen and a camera to record VMIs.

The valve, skimmers and the deflector were placed on motorized stages. By moving them vertically through the ionization laser area, the vertical molecular-beam-density profiles were measured. A further improved apparatus by using a knife-edge to cut unwanted molecules and increase the number density of the interested sample was introduced in [148].

3 A Pure Beam of Water Dimer*

3.1 Introduction

Hydrogen bonding between water molecules plays an important role in aqueous systems, e. g., for biomolecules that are surrounded by solvents. It is responsible for the unique properties of water, such as its high boiling point [149]. While hydrogen bonds have been studied extensively in many different molecular systems [26, 150–155], one of the most important models remains the water dimer, somehow the smallest drop of water. Numerous studies have been conducted on this benchmark system and its structure with a single hydrogen bond is well known [57, 58, 84, 156].

Water molecules and water clusters have been studied using various techniques to describe dynamics such as proton motion [157] or chemical processes, e. g., reactive collisions [158]. For investigations of ultrafast molecular dynamics, such as energy and charge transfer across hydrogen bonds in molecular systems, photoion-photoion coincidence measurements at free-electron lasers are developing as a powerful tool [155, 159, 160] and this approach was also used to study hydrogen bonding in the water dimer at a synchrotron [67]. Other spectroscopic techniques utilizing synchrotron facilities [161, 162] or table-top laser-systems [26, 52, 153, 163] further improved the knowledge about hydrogen bonding in water and water clusters.

Most of these experiments investigating the dynamics of hydrogen-bonded systems would benefit from samples of identical molecules in a well-defined initial state. The widely used supersonic expansion technique provides cold molecular beams down to rotational temperatures of < 1 K [13, 14, 19]. However, cluster expansions do not produce single-species beams, but a mixture of various cluster stoichiometries. Hence, only low concentrations of specific species can be achieved. In the case of water molecules, supersonic expansion produces a cold beam of various water clusters [150] with a water dimer concentration of only a few percent [67, 164]. This leads to small experimental event rates and requires long measurement times, e. g., in coincidence detection schemes [67, 160]. These experiments with a mixture of molecules in a molecular beam are only feasible if it can be disentangled which molecule was actually measured. Therefore, these mixtures severely limit the applicable techniques. A pure beam of water dimers would significantly speed up the measurements, when unwanted backgrounds from carrier gas and larger water clusters are avoided, or simply enable such experiments.

The electrostatic deflector is an established method to spatially separate the molecules of interest from the carrier gas and to separate different species within a cold molecu-

*This chapter is based on the publication: *Pure Molecular Beam of Water Dimer*, by Helen Bieker, Jolijn Onvlee, Melby Johny, Lanhai He, Thomas Kierspel, Sebastian Trippel, Daniel A. Horke, Jochen Küpper. My contribution was to perform the experimental measurements, data analysis, simulations, to discuss the results and to prepare the draft of the manuscript, including preparation of the figures.

lar beam [16]. This includes the separation of molecular conformers [20, 21, 165, 166], individual quantum states of small molecules [22, 167], as well as specific molecular clusters [19, 23, 168]. The deflector was previously utilized in investigations of water, e. g., to determine the rotational temperatures of "warm" molecular beams of water [169], to separate its *para* and *ortho* species [22], and to measure the dipole moment of small water clusters [170]. Alternatively, separation by the cluster species' distinct collision cross sections, i. e., by the transverse momentum changes due to scattering with a perpendicular rare-gas beam, was demonstrated [97]; this method is especially amenable to larger cluster sizes [171]. Such spatially separated single-species samples enable, for instance, advanced imaging applications of water clusters using non-species-specific techniques, as well as the study of size-specific effects and the transition from single-molecule to bulk behavior.

3.2 Experimental Methods

Here, the electrostatic deflector was used to spatially separate water dimers from water monomers as well as larger water clusters in a molecular beam formed by supersonic expansion. The experimental setup was described previously [16, 148]. Briefly, liquid water was placed in the reservoir of an Even-Lavie valve [14], heated to 55 °C, seeded in 100 bar of helium, and expanded into vacuum with a nominal driving-pulse duration of 19.5 µs and at a repetition rate of 250 Hz. The produced molecular beam was doubly skimmed, 6.5 cm ($\varnothing = 3$ mm) and 30.2 cm ($\varnothing = 1.5$ mm) downstream from the nozzle, directed through the electrostatic deflector [147] of 154 mm length and with a nominal field strength of 50 kV/cm with an applied voltage of 8 kV across the deflector, before passing through a third skimmer ($\varnothing = 1.5$ mm). The deflector was placed 4.4 cm behind the tip of the second skimmer. In the center of a time-of-flight (TOF) mass spectrometer, 134.5 cm downstream from the nozzle, molecules were strong-field ionized by a 35 fs short laser pulse with a central wavelength around 800 nm and a pulse energy of 170 µJ. Focusing to 65 µm yielded a peak intensity of $\sim 10^{14}$ W/cm^2. The generated ions were accelerated toward a microchannel-plate detector combined with a phosphor screen and the generated signal was recorded with a digitizer. The valve, skimmers, and deflector were placed on motorized translation stages, which allowed movement of the molecular beam through the ionization laser focus and the recording of vertical molecular-beam-density profiles without moving the laser focus, resulting in fixed imaging conditions [172–174].

While the employed strong-field ionization is a general, non-species specific ionization technique, it can also lead to fragmentation of molecules, such that recorded mass spectra (MS) do not directly reflect the composition of the molecular beam. In combination with the species-specific deflection process, however, this can be disentangled and, thus, even allows for the investigation of strong-field-induced fragmentation processes of a single species.

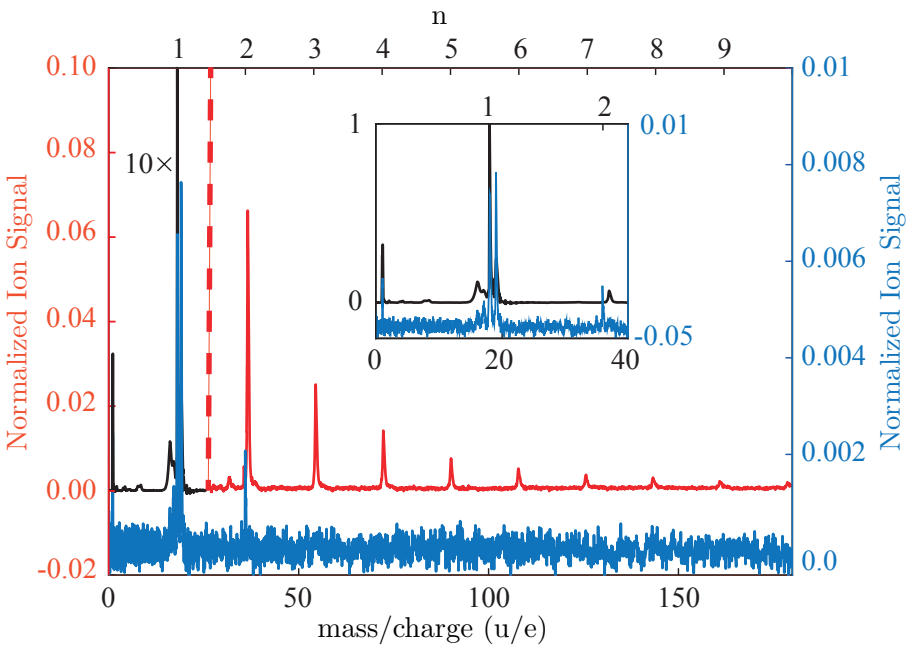

Figure 3.1: TOF-MS in the center of the molecular beam as depicted in Figure 3.2 with a deflector voltage of 0 kV (black, red) and at a position of +3 mm with a deflector voltage of 8 kV (blue). For mass/charge (m/q) ratios of 0 . . . 30 u/e, to the left of the dashed red line, the TOF-MS has been scaled by 0.1. The inset shows the region of $m/q = 0 \ldots 40$ u/e enlarged; see text for details.

3.3 Results and Discussion

TOF-MS of the direct and the deflected beams are shown in Figure 3.1. The spectrum of the undeflected beam shows water-cluster ions $(H_2O)_n^+$ up to $n = 2$ and protonated-water-cluster ions $(H_2O)_nH^+$ up to $n = 10$. Even larger clusters were likely formed in the supersonic expansion, but were not observed in the recorded TOF interval. We point out that all clusters that reach the interaction region are neutral clusters of the type $(H_2O)_n$, and protonated clusters must result from the interactions with the femtosecond laser, i. e., due to fragmentation during or after the strong-field-ionization process.

Vertical molecular-beam-density profiles for water ions $(H_2O)^+$, water-dimer ions $(H_2O)_2^+$, and protonated-water-cluster ions $(H_2O)_nH^+$ up to $n = 4$, with a potential difference of 8 kV applied across the deflector, are shown in Figure 3.2. For comparison, a field-free vertical profile for the water ion with 0 kV across the deflector is also shown. The vertical molecular-beam-density profiles have been normalized to the area of the field-free spatial profile of the water ion. For visibility the water-dimer profile has been scaled by a factor of 100 after normalization. While the field-free molecular beam profile is centered around 0 mm, application of a voltage of 8 kV to the deflector shifted the peak of water ions, water-dimer ions, and protonated- water-cluster ions by +0.5 mm, as indicated by the red arrow in Figure 3.2. In addition, water-dimer ions showed a broadening and an increase of signal at around +3 mm, indicated by a black arrow in Figure 3.2.

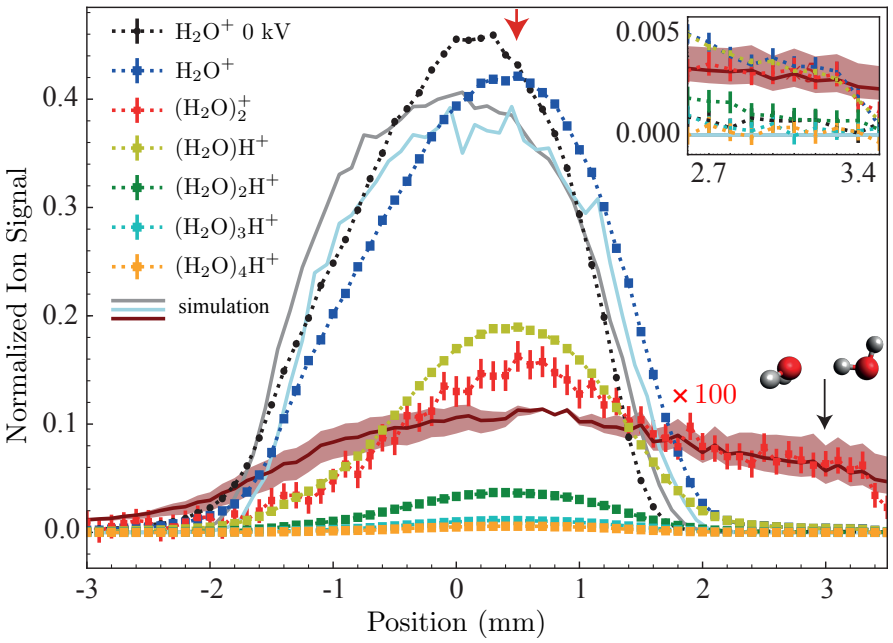

Figure 3.2: Normalized measured vertical molecular-beam-density profiles (dashed lines) of water cation $(H_2O)^+$ (blue), water-dimer cation $(H_2O)_2^+$ (red), and protonated- water-cluster ions $(H_2O)_nH^+$ up to $n = 4$ (yellow, green, cyan, orange) with deflector voltages of 0 kV (black circles) and 8 kV (squares). Simulated vertical molecular-beam-density profiles of the undeflected water monomer (grey) as well as of the deflected water monomer (light blue) and water dimer (dark red) with a deflector voltage of 8 kV are shown as solid lines. The shaded (dark red) area depicts the error estimate of the water-dimer simulation due to the temperature uncertainty, $T_{rot} = 1.5(5)$ K; see text for details. The black arrow indicates the position in the deflected beam where the TOF-MS shown in Figure 3.1 was measured. The inset shows the deflection region enlarged with a magnification factor of 5 applied to the $(H_2O)_2^+$ and $(H_2O)_nH^+$ signals.

In the inset of Figure 3.2 the region around +3 mm is shown enlarged with a magnification factor of 5 applied to $(H_2O)_2^+$ and $(H_2O)_nH^+$ with $n = 1 \ldots 4$. The corresponding TOF-MS in the deflected part of the beam at a position of +3 mm is highlighted in Figure 3.1 by the blue line. Not just water-dimer ions, but also hydronium ions, H_3O^+, and water ions, H_2O^+, showed an increased signal in the deflected beam. The shape of the vertical beam profiles for these ions matched the water-dimer profile in the region of 2.8–3.5 mm, indicating that they originated from the same parent molecule.

The water-dimer ion was the largest non-protonated cluster measured in this setup. To verify that the water-dimer ion was originating from the water dimer, the deflection behaviour of water clusters inside the electrostatic deflector was simulated. Therefore, the Stark energies and effective dipole moments of water monomers and water clusters were calculated with the freely available CMIstark software package [126] using rotational constants, dipole moments, and centrifugal distortion constants from the literature [57, 127–

130], see Suppl. Inf. Table A.1; contributions of the polarizability to the Stark effect could safely be ignored [147, 175]. The rotational constants of the water dimer are significantly smaller than for the water monomer, leading to a larger effective dipole moment for the water dimer than for water and a larger acceleration in the electric field in the deflector, see Figure A.3 and Table A.1 of the Suppl. Inf. for further information.

The simulated vertical molecular-beam-density profiles of the water monomer and the water dimer are shown in Figure 3.2. The deviations between the measured and simulated undeflected vertical beam profiles are ascribed to imperfect alignment of the experimental setup, which was not taken into account in the simulations. Due to the rotational-state dependence of the Stark effect, the deflection of a molecular beam in an electrostatic field depends on the rotational temperature of the molecular ensemble [16] and the best fit for the profiles of the water monomer and the water dimer at a deflector voltage of 8 kV was obtained assuming a Boltzmann population distribution of rotational states corresponding to 1.5(5) K.

Not only deflection of water clusters measured as a mass of 36 amu, but also of water clusters detected as protonated clusters have been measured, for instance, for $(H_2O)_2^+$, as indicated by the red arrow and symbols in Figure 3.2. Trajectory simulations for water clusters $(H_2O)_n^+$ with $n = 3 \ldots 7$ using a rotational temperature of $T_{\mathrm{rot}} = 1.5(5)$ K were performed to understand the origin of this deflection behavior. For the water hexamer three and for the water heptamer two conformers have been simulated, assuming an equal population of the conformers. These showed that, based on the different effective dipole moments, a different deflection is expected for different water clusters, see Figure A.5 of the Suppl. Inf.. Since the detected protonated water clusters arose from the strong-field fragmentation of larger neutral clusters in the interaction region, the measured vertical protonated-cluster-density profiles are a superposition of several neutral-water-cluster density profiles. Thus, it is not possible to compare the individual simulated molecular-beam-density profiles of neutral clusters directly with the measured protonated-water-cluster density profiles. Instead, at each position of the deflection profile the signal from all water clusters has been summed up, both for the simulated and the measured molecular-beam-density profiles. The result yields a comparable amount of deflection for simulated and measured molecular-beam-density profiles, see Suppl. Inf. Figure A.6. The shift of 0.5 mm can, therefore, originate from the superimposed molecular-beam-density profiles from different larger clusters due to fragmentation into smaller water clusters. The same shift is visible for H_2O^+ and $(H_2O)_2^+$, which indicates that water clusters are also fragmenting into H_2O^+ and $(H_2O)_2^+$. Nevertheless, the simulation for water clusters $n = 1 \ldots 7$ shows that the water dimer deflected the most, reaching a position of +3 mm and above, see Suppl. Inf. Figure A.4 and Figure A.5. Of all the other clusters considered, only the water hexamer in its prism and book forms reaches to a position up to 3.2 mm with the falling edge of the profile. In our experiments the water hexamer and higher order clusters have only been measured as fragments, such that the concentration and

size distribution of neutral clusters in the molecular beam is unknown. However, the measured fragment distributions strongly suggest that significantly larger clusters are not present, since the ion signals decay exponentially and it is known that clusters primarily fragment through loss of single water molecules [63, 92, 176].

The TOF-MS in the deflected part of the beam, shown in Figure 3.1, contains peaks corresponding to H^+, O^+, OH^+, H_2O^+, and H_3O^+, in addition to the water-dimer ion. As mentioned before the short-pulse ionization can lead to fragmentation. For the water dimer, two fragmentation channels were reported for electron-impact ionization with 70 eV electrons [92]: either an H_3O^+ ion and a neutral OH are formed or a H_2O^+ ion and a neutral water monomer H_2O. Using a size-selection method and infrared spectroscopy, H_2O^+ has been reported as a fragment of the water dimer [97]. Comparison of the vertical molecular-beam-density profiles of the deflected molecules allowed further investigation of the fragmentation channels of the water dimer. The measured vertical molecular-beam-density profiles of these molecules showed a similar deflection behavior in the region of 2.8 to 3.5 mm as the water dimer, see Figure 3.2 and Suppl. Inf. Figure A.1. The observed constant ratio of those fragments over this spatial region indicates that all these fragments originated from the water dimer.

Comparing the intensity of the fragments of the water dimer, H_2O^+ and H_3O^+ and $(H_2O)_2^+$, in the deflected beam, the fragmentation ratios of the intact water dimer were estimated. These showed that $46(7)$ % of the water dimer fragmented into one ionized water molecule, while $46(4)$ % of the water dimer underwent most likely proton transfer and formed a hydronium ion. Only $8(2)$ % of the water dimer present in the molecular beam stayed intact after ionization.

The actual number of water-dimer molecules per shot in the deflected molecular beam was estimated to $\sim$0.8 within the laser focus using the known fragmentation ratios of H_2O^+ and H_3O^+, while the fragmentation channels of H^+, O^+, OH^+ have not been included. Taking the known fragmentation channels into account, the fraction of the water dimer within the molecular beam was evaluated. Comparing the ratios between the water dimer and all other species visible in the TOF, a water-dimer fraction of $3.9(6)$ % in the center of the undeflected beam and of $93(15)$ % in the deflected beam, at a position of +3 mm, was achieved. Thus, using the electrostatic deflector the fraction of the water dimer within the interaction region could be increased by nearly a factor of 24.

3.4 Conclusions

In summary, a high-purity beam of water dimers was created using the electrostatic deflector, which spatially separated water dimers from other species present in the molecular beam. The resulting water dimer sample had a purity of $93(15)$ %. The fragmentation products and ratios of the water dimer following strong-field ionization using a 35 fs laser

pulse with a wavelength centered around 800 nm and peak intensity of $\sim 10^{14}$ W/cm^2 were studied, with 46(4) % of the water dimer found to form a hydronium ion and 46(7) % fragmenting into one water cation and one neutral water monomer, while 8(2) % of the water dimer stayed intact. The deflection profiles could be simulated using a rigid-rotor model and an initial rotational temperature of 1.5(5) K.

The produced clean samples of water dimers are well suited for non-species-specific experiments, e. g., reactive-collisions, diffractive imaging, or ultrafast spectroscopies [158, 172, 177]. Even for experiments that can distinguish different species, for example photoion-photoion coincidence measurements [155, 178], the produced clean beams will enable significantly faster measurements of this important hydrogen-bonded model system, e. g., because unwanted backgrounds are avoided. Furthermore, the electrostatic separation technique can be used to separate different conformers [16], which could be highly interesting in the purification and studies of larger water clusters that exhibit multiple conformers [106].

4 Non-Rigidity of Water Dimer

In chapter 3, the water dimer was treated as a rigid rotor to calculate the Stark energies and to simulate the vertical molecular-beam-density profiles of the water dimer in an electric field. But at room temperature the water dimer is a non-rigid cluster with large amplitude motions, which are changing the structure of the water dimer, its EDM and its behavior in an electric field. Thus, the rigid rotor approximation might not be valid anymore. In this chapter, the importance of the non-rigidity of the water dimer and its influence onto the Stark energies are investigated. First, a simple model is used to obtain the averaged dipole moment of each internal vibration of the water dimer to calculate the Stark energy of each vibrational mode using the rigid-rotor approximation. In the second part of this chapter, these calculations are improved by using a more accurate and more efficient way to calculate the Stark energies of the non-rigid water dimer. Therefore, the water dimer is modeled using an *ab-initio* variational approach to simulate the Stark energies using a Born-Oppenheimer-like approximation. Both simulations, which are neglecting the interaction between different vibrational modes and, thus, are only valid in case of low-field gradients and well-separated rotational states, are compared to the results of the rigid-rotor approximation of chapter 3.

4.1 A Simple Description of the Intermolecular Motions and their Effect on the Stark Energies [†]

In this section, the intermolecular motions of the water dimer are modeled assuming the water monomers inside the water dimer to be rigid with a fixed EDM. With this approximation, it is shown that only the acceptor wag, in-plane bend and torsional motion changes the water dimer EDM. For these three motions, the potential energy and the averaged EDM were modeled by solving the Schrödinger equation. Therefore, a Hamiltonian and a periodic potential were set-up, which describes the important intermolecular motions to calculate the averaged EDM. The Stark energies were calculated using these averaged EDMs of each motion treating the water dimer as a rigid rotor again.

The experimentally observed equilibrium geometry is discussed in subsection 2.1.1 and shown in Figure 2.1. However, the water dimer is a non-rigid molecule with large amplitude motions, which are changing the positions of the atoms inside the water dimer. As discussed in subsection 2.1.2, the major vibrations of the water dimer are the intermolecular vibrations and can be described by six Euler rotations with the angles $\alpha_j, \beta_j, \gamma_j$ with $j = A, D$ for the acceptor water and donor water, respectively, around the z, y and x-axis, respectively, and by a hydrogen bond stretching along the z-axis changing

[†]This chapter was done in collaboration with Boris Sartakov from the Russian Academy of Sciences in Moscow.

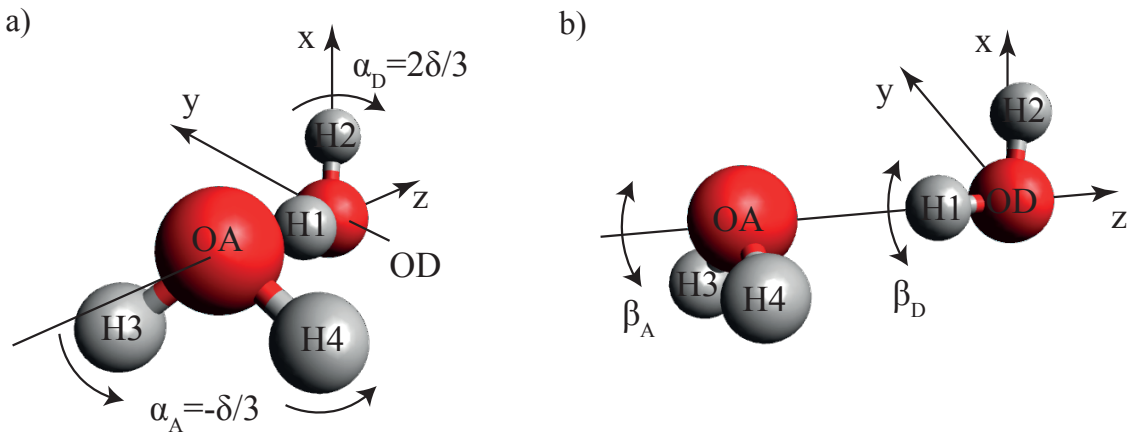

Figure 4.1: a) The torsional motion δ is a rotation of the water monomers inside the water dimer around the z-axis. It can be described as a rotation of the donor around α_D and the acceptor α_A in opposite directions. The donor D is rotating twice as much as the acceptor A. b) The acceptor wag and in-plane bend are rotations of the acceptor with an angle β_A and of the donor with an angle β_D, respectively, around the y-axis.

the distance R_{OO} of the two oxygens. In first order approximation, we can describe these vibrational modes as independent and not interacting. The EDM of the water dimer is assumed to be a vector sum of the EDMs of the two water monomers, which are assumed to be rigid. The orientation of the EDM of the water monomers is then fixed to the water-monomer orientation. With these assumptions, the overall rotation of the water dimer, the OO-Stretch R_{OO}, the acceptor twist γ_A and the out-of-plane bend γ_D do not influence the direction of the EDM of the water monomers and the overall EDM of the water dimer. Thus, only the torsional motion, the acceptor wag and the in-plane bend, which are shown in Figure 4.1, are changing the water-dimer EDM.

The torsional motion with an associated angle δ describes the rotation of the donor oxygen with an angle α_D and the acceptor oxygen with an angle α_A around the z-axis in opposite directions, see Figure 4.1 a). The overall angle of the torsional motion is then given by $\delta = \alpha_D - \alpha_A$, where the donor angle α_D is twice as much as the acceptor α_A. The in-plane bend with the associated angle β_D describes the rotation of the donor and the acceptor wag β_A the rotation of the acceptor around the y-axis, as shown in Figure 4.1 b).

The influence of the internal vibrations on the EDM can be obtained by solving the Schrödinger equation and by afterwards calculating the averaged EDM of the water dimer for each individual vibration. Each of these three internal motions can be described as a rotation, which can be characterized by the appropriate moment of inertia and a 2π-periodicity of its effective potential $U(\beta)$.

Solving the Schrödinger Equation for the Torsional Motion

In the framework of this chapter, the rigid rotor approximation was used except for the torsion between the two water molecules. Thus, the Hamiltonian $\hat{H}$ to solve the time independent Schrödinger equation

$$\hat{H}\psi_m(\delta) \quad = \quad E\psi_m(\delta) \tag{4.1}$$

can be described by independent rotations of the acceptor A and donor D with an interaction potential. As the mass of the oxygen is larger than the hydrogen, the rotations are assumed to be around the OO-axis. As the H1-atom is on a line with the two oxygen-atoms of the acceptor (OA) and donor (OD), the rotation of the donor can be described in analogy of a linear molecule [179], where the H1-atom is rotating around the OO-axis. The rotation of the acceptor is described as a rotation of the two hydrogen H3 and H4 around the OO-axis. Thus, the Hamiltonian can be written as

$$\hat{H} \quad = \quad B_D\hat{L}_D^2 + B_A(\hat{L} - \hat{L}_D)^2 + U(\delta) \tag{4.2}$$

with the angular momentum operator $\hat{L}_D = -i\frac{\partial}{\partial\alpha_D}$ of the donor, the total angular momentum operator $\hat{L} = \hat{L}_D + \hat{L}_A = -i\frac{\partial}{\partial\delta}$ and the angular momentum operator $\hat{L}_A = -i\frac{\partial}{\partial\alpha_A}$ of the acceptor. The first term in Equation 4.2 describes the rotation of the donor and the second term the rotation of the acceptor. Thus, the Hamiltonian can be rewritten as

$$\hat{H} \quad = \quad B_D\frac{\partial^2}{\partial\alpha_D^2} + B_A(\frac{\partial}{\partial\delta} - \frac{\partial}{\partial\alpha_D})^2 + U(\delta). \tag{4.3}$$

As the torsional vibration is treated as an angular rotation, the effective potential can be characterized by a 2π-periodicity using a periodic model potential

$$U(\delta) = \frac{V_{\max,\delta}}{2}(1 - \cos\delta), \tag{4.4}$$

as a first-order approximation with a maximum of the angular potential $V_{\max,\delta}$, while the true potential would be more complex [180, 181]. The basis functions

$$\psi_m(\delta) = \frac{1}{\sqrt{2i\pi}}e^{-im\delta} \tag{4.5}$$

can be used as a basis set to solve the time independent Schrödinger equation for the Hamiltonian in Equation 4.3 with an integer m. The rotational constants of the water monomers were calculated to be $B_D = 14.36\ \mathrm{cm}^{-1}$ for the donor and $B_A = 17.22\ \mathrm{cm}^{-1}$ for the acceptor.

Solving the Schrödinger Equation for the Acceptor Wag β_A and the In-Plane Bend β_D

The acceptor wag β_A and the in-plane bend β_D are rotations of a single water monomer around the y-axis, see Figure 4.1 b), and around the principal axes of inertia of the water monomers. Thus, the rotational constants of the water monomer $C = 9.3\ \mathrm{cm}^{-1}$ [182] can be used as rotational constant B_β of these β-motions and for computing the eigenvalues. The corresponding Hamiltonian in the basis set of a free rotor can be modeled in analogy to the torsional motion as

$$\hat{H} = -B_\beta \frac{\partial^2}{\partial \beta^2} + U(\beta) \tag{4.6}$$

with the first-order approximation periodic potential

$$U(\beta) = \frac{V_{\max,\beta}}{2} \left(1 - \cos(\beta)\right) \tag{4.7}$$

where $V_{\max,\beta}$ is the maximum of the angular potential. The basis function

$$\psi_m(\beta) = \frac{1}{\sqrt{2\pi}} e^{-im\beta} \tag{4.8}$$

was used to solve the time-independent Schrödinger equation for the Hamiltonian in Equation 4.6 with an integer m.

The Potential Energy and the Averaged EDM

After solving the Schrödinger equation for the three vibrational modes, the potential energy curves, wave functions and resulting energy levels were analyzed. The potential energy curve describes the potential energy of the water dimer in dependence of the rotation according to the angles β_D, β_A and δ. The modeled potential energy and wave functions of the ground and first excited states of the torsional motion and of the in-plane bend and acceptor wag are shown in Figure 4.2 a), b) and in Figure 4.2 c), respectively. The maximum of the angular potential $V_{\max,\eta}$ with $\eta = \delta, \beta_A, \beta_D$ was chosen such that the difference of the first and second eigenvalue $E_{2,\eta} - E_{1,\eta}$ fits to the experimental observed frequencies ν_η, which are listed together with the used parameters and the corresponding measured frequencies in Table 4.1.

The influence of the three vibrational motions onto the EDM can be calculated in dependence of the corresponding Euler angles. The overall EDM of the water monomer is $\mu_{\mathrm{monomer}} = 1.857$ D [127] and assumed to be fixed for rotations around its principal axes of inertia, as done in the torsional motion, acceptor-wag and in-plane bend. The water-dimer EDM is then given by a vector sum of the water-monomer EDMs with the

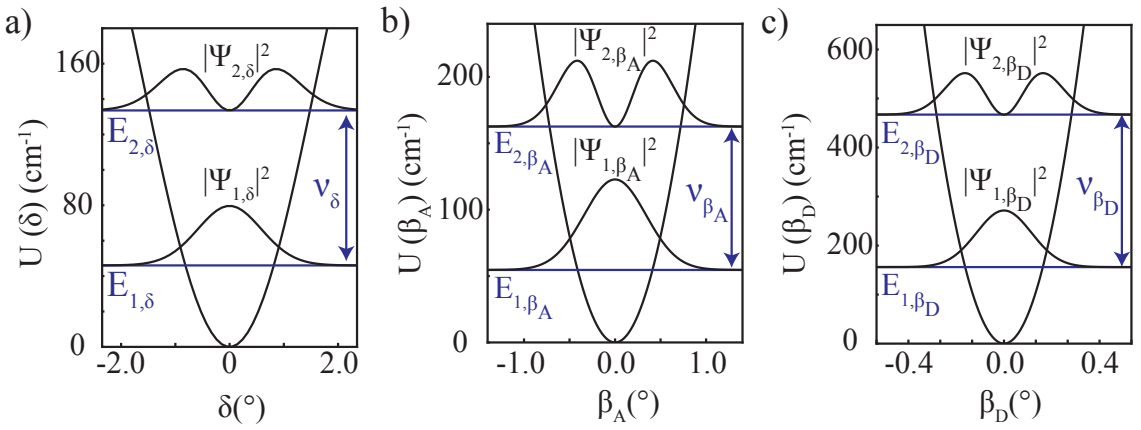

Figure 4.2: The potential energies of the a) torsional motion δ, b) acceptor wag β_A and c) in-plane bend β_D of the water dimer and the squares of the respective wave functions $|\Psi_\eta|^2$ of the ground and the first excited states with energies $E_{1,\eta}$, $E_{2,\eta}$ with $\eta = \delta, \beta_A, \beta_D$. The difference of the eigenvalues $E_{2,\eta} - E_{1,\eta}$ is given by the experimentally observed frequencies listed in Table 4.1.

Name	Frequency $\nu_\eta(\mathrm{cm}^{-1})$	Fitted Frequency $\nu_{\eta,\mathrm{fit}}(\mathrm{cm}^{-1})$	$V_{\max}$ (cm^{-1})	B_{acceptor} (cm^{-1})	B_{donor} (cm^{-1})
Torsional motion δ	88	88	293	17.22	14.36
Acceptor twist γ_D	103	-	-	14.5	-
Acceptor wag β_A	108	108	1310	9.3	-
OO-stretch R_{OO}	143	-	-	-	-
In-plane bend β_D	311	311.039	10569	-	9.3
Out-of-plane bend γ_A	523	-	-	-	14.5

Table 4.1: Experimentally observed frequencies [87], fitted frequencies and rotational constants of the corresponding vibrational motion used for the model.

water-monomer-EDM vector $\vec{\mu}_{\mathrm{monomer}} = \mu_{\mathrm{monomer}} \vec{n}$ and the unity vector

$$\vec{n} = \begin{pmatrix} \cos\alpha \sin\beta \\ \sin\alpha \sin\beta \\ \cos\beta \end{pmatrix}$$

using the Euler angles α and β describing the rotations of the water monomers independently. For sake of simplicity using $\alpha_A = 0$ and $\alpha_D = \delta$ leads to the following water-dimer-EDM vector

$$\vec{\mu}_{\mathrm{dimer}} = \mu_{\mathrm{monomer}} \begin{pmatrix} \cos\delta \sin(\pi - \theta_a - \chi + \beta_D) + \sin(\pi + \theta_a - \beta_A) \\ \sin\delta \sin(\pi - \theta_a - \chi + \beta_D) \\ \cos(\pi - \theta_a - \chi + \beta_D) + \cos(\pi + \theta_a + \beta_A) \end{pmatrix} \tag{4.9}$$

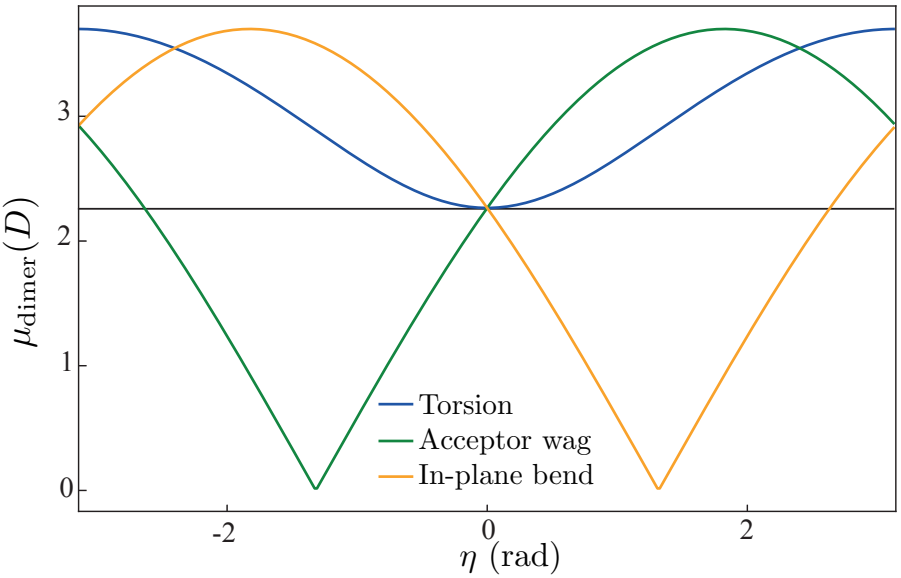

Figure 4.3: EDMs μ of the water dimer for the vibrational modes of the torsional motion (blue), acceptor wag (green) and in-plane bend (orange) with rotation angles $\eta = \delta, \beta_D, \beta_A$. The calculated equilibrium EDM is shown as a black solid line.

with the angles θ_a and χ of the water monomers inside the ground state water dimer, as discussed in subsection 2.1.1. The results for the EDM of the water dimer for different rotation angles $\eta = \delta, \beta_A, \beta_D$ are shown in Figure 4.3. Using vector addition, the EDM for the water dimer in the equilibrium structure is determined to be 2.27 D, while the measured EDM of water dimer is $\mu_{\text{dimer, exp}} = 2.63$ D [57]. The permanent EDM for the torsional motion takes values between 2.2 D to 3.7 D for various angles δ, while the EDM of the acceptor wag and the in-plane bend varies between 0 D and 3.7 D for angles β_A and β_D, respectively.

The expectation value of the EDM $\langle \mu_{\text{dimer},\eta} \rangle$ of each vibrational motion η gives an estimation how much the EDM of the water dimer is changing from the ground state. It can be calculated using the obtained eigenfunctions ψ_i of the potential energy $U(\eta)$ with $\eta = \delta, \beta_A, \beta_D$. The expectation value of the EDM of the water dimer is then given by

$$\langle \mu_{\text{dimer},\eta} \rangle = \left\langle \psi_{i,\eta} \middle| \mu_{\text{dimer},\eta} \middle| \psi_{i,\eta} \right\rangle = \int_{-\pi}^{\pi} \psi_{i,\eta} \mu_{\text{dimer},\eta}(\eta) \psi_{i,\eta} d\eta, \tag{4.10}$$

integrating over the whole range of $\eta = \beta_D, \beta_A, \delta$ for the first excited state i of the vibrational mode η with $\mu_{\text{dimer}} = \sqrt{\mu_{\text{monomer}}(n_x^2 + n_y^2 + n_z^2)}$. As in a cold beam probably only the lowest torsional states are populated, the integration goes over all three angles with using the orthogonality of eigenfunctions of $U(\eta)$, therefore, only one angle of interest is left. The obtained averaged dipole moments are listed in Table 4.2 for each vibrational motion. Comparing the expectation values of the EDM $\langle \mu_{\text{dimer},\eta} \rangle$ to the EDM of the equilibrium. These numbers suggest that all vibrations are small amplitude motions. Nevertheless, the expectation values of the EDM of the torsional motion, the acceptor

Name	EDM $\langle \mu_{\text{dimer},\eta} \rangle$ (D)	Scaled EDM $\langle \mu_{\text{dimer},\eta} \rangle$ (D)
Equilibrium	2.27	2.63
Torsional motion δ	2.67	3.1
Acceptor twist γ_A	2.27	2.63
Acceptor wag β_A	2.4	2.6
OO-stretch R_{OO}	2.27	2.63
In-plane bend β_D	2.2	2.55
Out-of-plane bend γ_D	2.27	2.63

Table 4.2: The expectation values of the EDMs and the scaled EDMs such that the equilibrium EDM fits the measured water-dimer EDM of 2.63 D [57].

Name	Rotational Constants (MHz)				Centrifugal Distortion constants (MHz)					
	A	B	C		Δ_J	Δ_{JK}	Δ_K	d_J	d_K	
Torsion δ	190327	6124.008	6124.008	[31, 129]	0.043	0	0	0	0	[31]
Acceptor wag β_A	190327	6127.966	6127.966	[31, 129]	−0.0147	0	0	0	0	[31]
In-plane bend β_D	190327	6162.762	6133.741	[130]	0.044	4.01	0	0	0	[57]

Table 4.3: Rotational constants and centrifugal distortion constants of water dimer in different vibrational modes used in the Stark effect calculations.

wag and the in-plane bend were used to calculate the corresponding Stark energies. As the expectation values of the EDM of the equilibrium structure is different to the measured EDM of the water dimer, see Table 4.2, the calculated EDMs were linearly scaled such that the averaged equilibrium EDM fits the measured water dimer EDM for a better comparison of the Stark energies.

Afterwards, the Stark energies of the torsional motion, acceptor wag and in-plane bend were calculated with the freely available CMISTARK software package [126] using the averaged water dimer EDM $\langle \mu_{\text{dimer},\eta} \rangle$ of each vibrational mode in the first excited state i as the permanent EDM of the water dimer treating the water dimer as a rigid rotor. The rotational and centrifugal distortion constants were taken from the literature [31, 129] and are listed in Table 4.3. The calculated Stark energies for $|J, K_a, K_c, M\rangle$-states up to $J = 5$ with field-free energies up to 7.5 cm^{-1} of the torsional motion, acceptor wag, in-plane bend and of the rigid water dimer are shown as a function of the electric field strength in Figure 4.4. For a better visibility the rotational states $J = 0 \ldots 5$ are shown in different subfigures from the bottom to the top. As only states with field-free energies up to 7.5 cm^{-1} only K_a-states up to 1 are shown. All states up to $J = 3$ were strong-field seeking and, hence, accelerated toward regions of stronger fields. States of $J = 3 - 5$ have low and high-field seeking states. The discontinuous change of the Stark energy for the acceptor wag at an electric field strength around 32 kV/cm and the torsional motion at an electric field strength around 28 kV/cm is ascribed to an avoided crossing of the $|J, K_a, K_c, M\rangle = |5, 0, 5, 0\rangle$ and $|1, 1, 0, 0\rangle$ states, which did not occur in the rigid rotor approximation and lead to a different gradient of the $|5, 0, 5, 0\rangle$ of the acceptor wag and

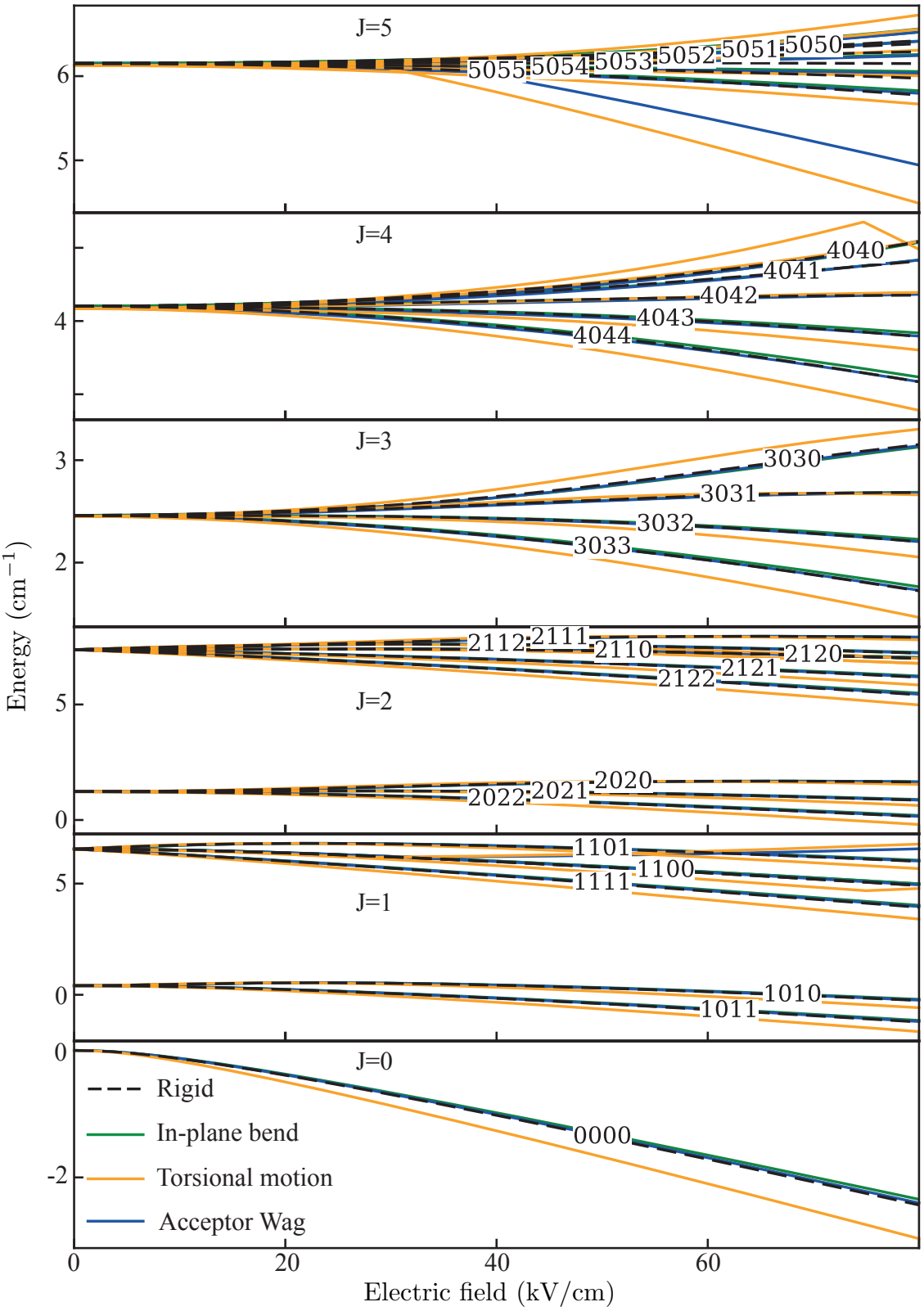

Figure 4.4: Simulated Stark energies $|J, K_a, K_c, M\rangle$ for $J = 0 \ldots 5$ with field-free energies up to 7.5 cm^{-1} of the rigid water dimer (dashed lines) and of the vibrational modes of the water dimer (solid line) treated as a rigid rotor.

the torsional motion compared to the rigid rotor approximation and the in-plane bend. At electric field strengths of 74 kV/cm and 79.5 kV/cm avoided crossing were occurring between $|J, K_a, K_c, M\rangle = |4, 0, 4, 0\rangle$ and $|1, 1, 1, 0\rangle$ and between $|2, 1, 2, 0\rangle$ and $|1, 1, 0, 0\rangle$ for the torsional motion only. Due to the larger averaged EDM, the torsional motion had a larger gradient of the Stark energy than the rigid rotor approximation, the acceptor wag and in-plane bend. Thus, the torsional motion differed the most from the rigid-rotor approximation and, therefore, had the largest effect on the behavior of water dimer in strong fields. From this first approach, it can be seen that all the intermolecular motions affected the Stark shift only slightly, while the torsional motion had the biggest effect on the Stark energies of the water dimer.

4.2 Adiabatic Molecular Dynamics Simulation of the Non-Rigid Water Dimer

In the previous Section 4.1, it is shown that the effect of internal vibrations of the water dimer onto its behavior in strong electric fields is small, describing the water dimer as a semi-rigid rotor and assuming the water dimer EDM to be a vector sum of the two water monomers with a fixed EDM of the water equilibrium structure. However, for an accurate simulation, it is important to take these motions into account. Thus, in this section, all intermolecular motions are described in a more accurate and more efficient way using a variational approach instead of describing each motion one by one. This might become even more relevant for the implementation of larger clusters and non-adiabatic effects that are known to play a role on the behavior of the molecules in strong electric fields, such that it will be easier to adapt to that afterwards. Therefore, a similar procedure to the Born-Oppenheimer approximation, which was used to separate the motion of nuclei from the motions of the electrons [34], was used to separate the slow translational from the fast rovibrational motions for the non-rigid water dimer, see subsection 2.1.2 for further details. As the translational motion is a slowly acting perturbation on the fast rovibrational motion, they can be separated and described independently. Mixing of states and coupling terms of the translational and rovibrational systems were neglected. The electric field is then a slowly acting perturbation compared to the rotation, which means the rovibrational system remains in its initial eigenstate.

First, the field-free energies of rovibrational states of the non-rigid water dimer were calculated by the group of Edit Mátyus of the Eötvös Loránd University using an *ab-initio* variational approach, see [183] for a similar calculation of the methane-water dimer. The rigid simulation in chapter 3 lead to an initial rotational beam temperature of 1.5 K. Rotational states up to $J = 5$ with a field-free energy up to 7.5 cm^{-1} account for 99.8 % of the population at this temperature and, therefore, excluded higher states from the non-rigid simulations. Thus, only states in $A_1^{\pm}$, $B_1^{\pm}$ and $E^{\pm}$ spin states with a NSSW of $1, 0$ and

3 were used, see subsection 2.1.3. Using these field-free energies the eigenvalues and Stark energies in an electric field with a nominal field strength of 50 kV/cm were computed using *RichMol* [132], a general variational approach for rovibrational molecular dynamics in external electric fields, by Andrey Yachmenev and Yahya Saleh [184]. These results were used to calculate the trajectories through the whole experimental setup of 10^7 molecules for each set of quantum state $|J, K_a, K_c, M\rangle$ with an initial Boltzmann distribution and an initial spread of the transverse velocities and positions of 10 m/s and 2 mm [174]. In chapter 3, the alignment of the experimental setup was imperfect and was not taken into account in the simulations. Here, the simulations were further improved by including the alignment of the experimental setup in both the rigid and non-rigid simulations, leading to an initial rotational temperature of 2.5 K of the molecular beam instead of 1.5 K. For a temperature of 2.5 K, states with field-free energies up to 7.5 cm^{-1} make a population of 96.9 % and, therefore, the vertical molecular-beam-density profiles are slightly less accurate, but good enough to compare the rigid and non-rigid simulations. For the electrostatic deflector a length of 154 mm and a nominal field strength of 50 kV/cm was used, which are the same settings as of chapter 3. The electric field was modeled using a zero-gradient over the length of the deflector in the flight direction of the molecules, thereby neglecting the variation of the electric field at the edges of the deflector.

The calculated Stark energies and simulated vertical molecular-beam-density profiles for single rotational states $|J, K_a, K_c, M\rangle$ up to $J = 5$ using the rigid and non-rigid approximation are shown in Figure 4.5 on the left- and right-hand side, respectively. For a better visibility, the rotational states $J = 0 \ldots 5$ are shown in different subfigures from the bottom to the top. For the non-rigid case, the three nuclear spin states A_1, B_1, E_1 and, for the rigid simulation, the two spin states A', A'' are shown. While rotational states with the same J-state in the the rigid rotor approximation had the same field-free energy, this did not apply for non-rigid states due to the splitting of the energy levels based on the nuclear spin, see subsection 2.1.3. Overall the Stark energies of the E_1-states showed a similar gradient as a function of the electric field as the rigid water dimer in A' and A'' states for all shown J-states. Just the field-free energies were shifted toward larger energies for E_1- states. The A_1- and B_1-states had no corresponding states in the rigid simulation. For $J = 1$ and $J = 2$, the rigid simulation contained states that shifted above 7.5 cm^{-1} in the non-rigid simulation and were, therefore, not included in the non-rigid simulation. On the right-hand side the normalized vertical molecular-beam-density profiles of the rigid and non-rigid simulations neglecting the rotational temperature are shown. For visibility these were averaged for states with the same J-state. A clear similarity of the vertical molecular-beam-density profiles of the non-rigid E_1 and the rigid states is visible. Also A_1- states with $J = 0, 1$ underwent a similar deflection as the rigid-rotor states. The spatial shift of the B_1-states differed the most from the rigid rotor approximation, but as the NSSW is zero, see subsection 2.1.3, it had no influence on the overall deflection profile.

The overall vertical molecular-beam-density profiles of the experiment, the rigid and

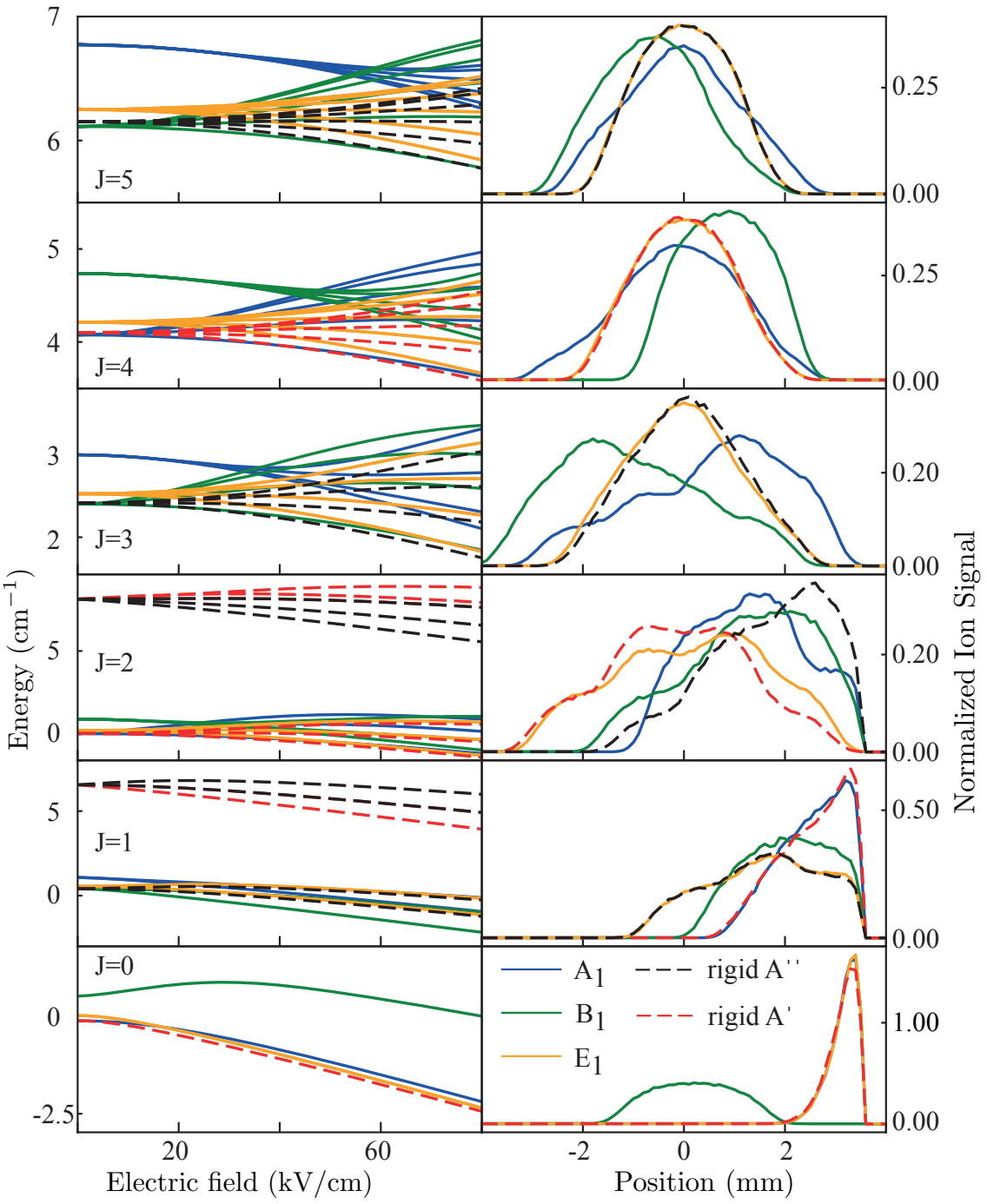

Figure 4.5: Calculated Stark energies (left) and simulated and averaged vertical molecular-beam-density profiles (right) for $J = 0 \ldots 5$ of the water dimer as a rigid approximation (dashed lines) in the two spin states A' (red) and A'' (black) and the water dimer as a non-rigid molecule (solid line) of the nuclear spin states A_1 (blue), B_1 (green) and E_1 (orange).

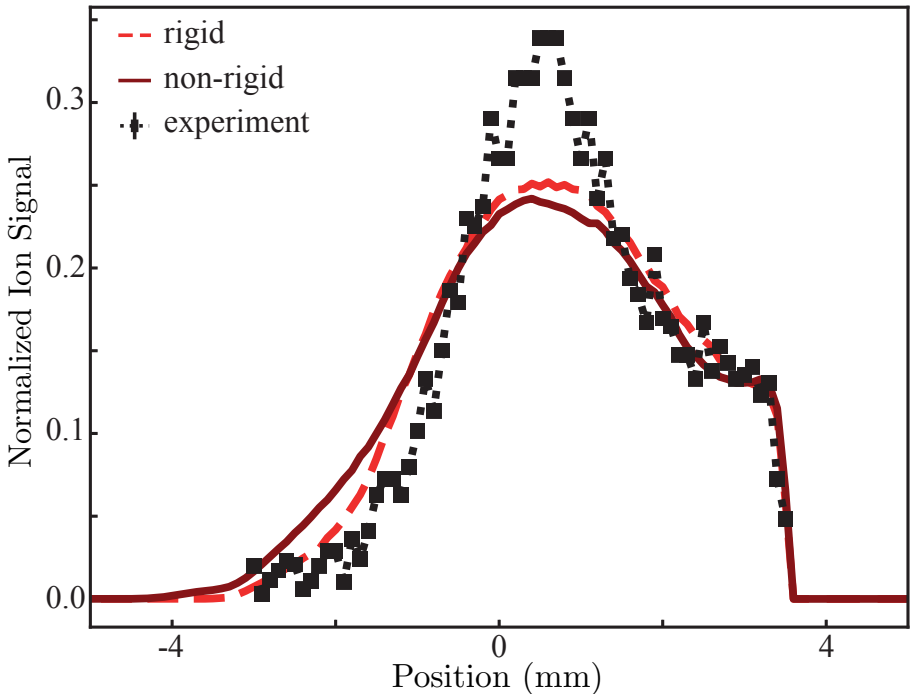

Figure 4.6: Measured (black squares, dotted) and simulated vertical molecular-beam-density profiles of the water dimer using a rigid (red, dashed) and non-rigid (dark red, solid) assumption with a deflector voltage of 8 kV and a rotational temperature of 2.5 K. The ion signal is normalized to the area under the curve.

non-rigid simulation with an initial rotational temperature of 2.5 K are shown in Figure 4.6. Both simulated vertical molecular-beam-density profiles reached up to 3.6 mm. Here, the experimental vertical molecular-beam-density profiles were clipped by the first spectrometer plate, which were taken into account in the simulations as well. The rigid and the experimental vertical molecular-beam-density profiles had a maximum at 0.6 mm, while the non-rigid simulation had a maximum at 0.4 mm. In the region of 2.2 mm to 3.3 mm, the experimental and the non-rigid vertical-molecular-beam-density profile had a plateau.

Overall, the rigid-rotor and non-rigid descriptions of the water dimer lead to similar vertical molecular-beam-density profiles and a reasonable description of the experimental measured vertical molecular-beam-density profile of the water-dimer cation. The similarity of the two simulations was due to the similar gradients of the Stark energies of the E_1-spin-states and the states from the rigid-rotor model. However, a slight difference of the simulations was due to the different nuclear spin assignment and weighting of the rotational states. The difference of the left-hand side edge in Figure 4.6 was larger for the non-rigid than for the rigid simulation. The left-edge mainly contained A_1-states in the non-rigid and A'-states in the rigid simulation. The experiment had a larger intensity in the maximum than the rigid and non-rigid simulations. This might be due to a contribution from larger water clusters fragmenting into water dimer cations. As only $J = 0, 1$-states deflect up to a position of 3.2 mm and higher rotational states usually deflect less, taking

higher rotational states than $J \leq 5$ and larger field-free energies than 7.5 cm^{-1} into account could lead to a smaller contribution of the ground and first excited state and to a different initial rotational temperature.

The adiabatic approximation breaks down in case of dense rotational states or large field gradients and high translational velocities. These effects are called nonadiabatic and lead to a transition of states inside the electric field. These are expected to occur especially at the borders of the deflector, as the fields are rapidly changing. For future simulations, the changes of the electric field at the edge of the deflector and the nonadiabatic effects are planned to be taken into account to study the influence of non-rigid effects.

5 Photophysics of Pure Water Dimer following Strong-Field Ionization[‡]

5.1 Introduction

Investigating biological systems, such as proteins and DNA, is highly important to understand, inter alia, the human body and to find new cures for diseases. As many biological molecules are inactive in the absence of water, it is highly important to understand their properties and interactions in the presence of water [51, 63, 176]. One of the key aspects to understand the effect of solvation on biomolecules is hydrogen bonding, which is still not well understood even for the much simpler case of pure water clusters. Understanding hydrogen bonding in water itself, is an important step toward understanding solvation of biomolecules. As the water dimer is the smallest water cluster, it is a favorable model system to study its hydrogen bonding and fragmentation behavior.

One way to study hydrogen bonding is the usage of strong-fields, such as free-electron lasers and femtosecond lasers, which offer new opportunities to study these systems and their ultrafast dynamics. The interaction of molecules with strong-fields can lead to fragmentation and dissociation of molecules [185–193]. As these methods are not size or isomer specific, it is important to either sort the molecular system by size and isomer prior to the interaction with the field, or detect all fragmentation products in coincidence to determine the corresponding parent system.

As cluster expansions do not produce single-species beams, but a mixture of various cluster stoichiometries, it is challenging to study a specific cluster in molecular beams. Hence, only low concentrations of specific species can be achieved. In the case of water molecules, supersonic expansion produces a cold beam of various water clusters [150] with a water dimer concentration of only a few percent [67, 164]. This leads to small experimental event rates and requires long measurement times. These experiments with a mixture of molecules in a molecular beam are only feasible if it can be disentangled which molecule was actually measured. Therefore, these mixtures severely limit the applicable techniques. Using a pure molecular beam of water dimer instead can help to disentangle its fragmentation pathways in more detail. An established method to spatially separate molecules of interest from different species within a cold molecular beam is the electrostatic deflector [16]. Alternatively, separation by the cluster species' distinct collision cross sections, i. e., by the transverse momentum changes due to scattering with a perpendicular rare-gas beam, was demonstrated [97] and has shown that in fact a fragmentation product

[‡]This chapter is based on a preliminary version of the manuscript: *Photophysics of pure water dimer following strong-field ionization*, by Helen Bieker, Jolijn Onvlee, Melby Johny, Sebastian Trippel, Daniel A. Horke, Jochen Küpper. My contribution was to perform the experimental measurements, the data analysis, to discuss the results and to prepare the draft of the manuscript, including preparation of the figures.

of H_2O^+ is involved in the water dimer fragmentation pattern [97].

The fragmentation patterns depend on the specific ionization states, which each exhibit different dynamics. Which ionization states are addressed can be achieved using specific wavelength and laser intensities. The water dimer cation has shown a dissociation process following single ionization of $H_3O^+ + OH$ using vacuum ultraviolet radiation [63], while electron-impact ionization revealed that the water dimer cation is favored to decay into $H_3O^+ + OH$ but that it also breaks up into $H_2O^+ + H_2O$ with 15 % probability [63, 92]. After double ionization of the water dimer, fragmentation pathways resulting in $H_2O^+ + H_2O^+$ and $H_3O^+ + OH^+$ were identified experimentally using synchrotron and infrared radiation [67, 99]. Further, a branching ratio of 0.081 ± 0.003 of $H_3O^+ + OH^+$ to $H_2O^+ + H_2O^+$ for the double ionization of water dimer was measured using strong-field ionization and infrared radiation [99]. With these values, a proton transfer rate of 0.032 ± 0.005 fs^{-1} of the ground state $(H_2O)_2^+$ using the Ammosov-Krainov-Delone model was determined.

Here, an electrostatic deflector [16] was used to create a high-purity water dimer sample [194]. This allowed to investigate the fragmentation of the water dimer after strong-field ionization. Moreover, it enabled us to calculate the branching ratios after single and double ionization using a velocity map imaging spectrometer with a slicing method. Further, this lead us to investigate the kinetic energy release and the anisotropies of the individual fragments.

5.2 Experimental setup

The experimental setup was described elsewhere [194]. Briefly, water was placed in the reservoir of an Even-Lavie valve [14], which was heated to 55 °C. The molecules were seeded in 100 bar of helium, and expanded into vacuum with a repetition rate of 250 Hz. The molecular beam was directed through three skimmers ($\varnothing = 3$ mm, $\varnothing = 1.5$ mm, $\varnothing = 1.5$ mm) and an electrostatic deflector behind the second skimmer [147]. We have previously demonstrated that this produced a molecular beam containing 93 % of water dimers [194]. A VMI spectrometer was placed 134.5 cm downstream from the nozzle, where molecules were strong-field ionized by a 35 fs laser pulse with a central wavelength of 800 nm and a pulse energy of 170 µJ. Focusing to 40 µm FWHM yielded a peak intensity of $\sim 4 \times 10^{14}$ W/cm^2. The generated ions were accelerated toward a microchannel-plate detector combined with a phosphor screen and a high-voltage switch (Behlke Power Electronics GmbH), which was used to gate the detector for measuring ions with a specific mass-to-charge ratio. The generated signal was recorded with a CMOS-camera. Normally, we use a pulse duration of 80 ns for the high-voltage switch to mass-gate the detector. However, since the timing resolution from the HV-switch was insufficient to distinguish water (m/z 18) from hydronium (m/z 19), we alternately measured VMI images with pulse durations of 80 ns and 90 ns and subtracted the measured signals from each other to achieve a temporal resolution of 10 ns, which we call gate-subtraction method in the

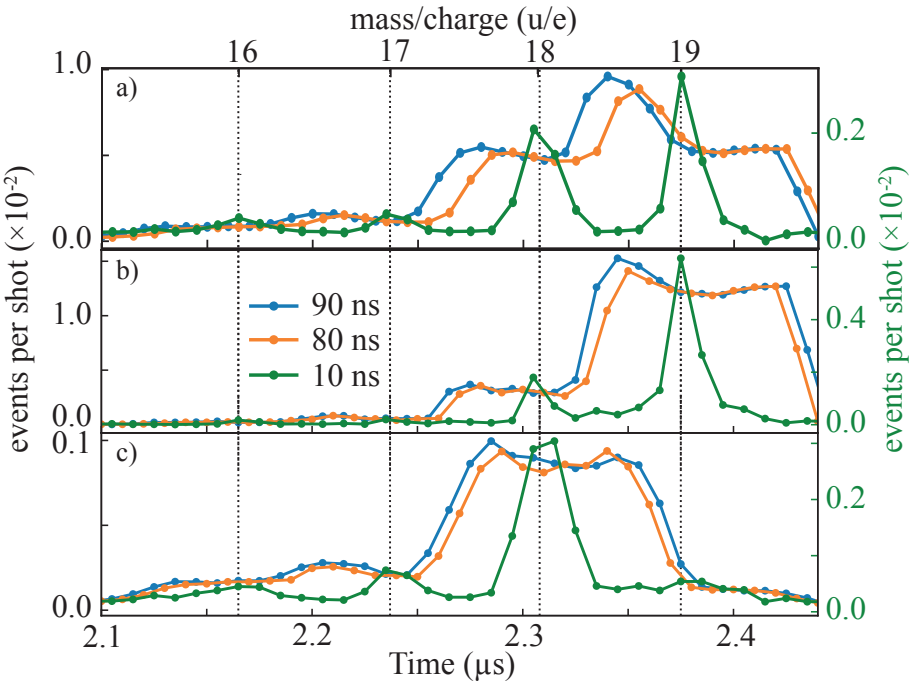

Figure 5.1: a) A measured TOF of b) ions originating from single ionization and c) double ionization. Each point contains ions with an arrival time width of 80 ns (orange), 90 ns (blue) and 10 ns (green). The green curve was obtained by subtracting the TOF with 80 ns pulse width from the TOF with 90 ns pulse width.

following.

5.3 Results and Discussion

5.3.1 Improved Timing Resolution for Mass Spectra and Ion Images

A MS is shown in Figure 5.1 a) for a pulse duration of 80 ns (orange), 90 ns (blue) and 10 ns (green). The arrival time on the x-axis is defined here as the mean between the start and end time of the gate of the HV-switch. A second x-axis on the top is showing the corresponding TOF-MS (m/q) in units of u/e. The TOF was extracted by counting the number of ions in the measured VMIs at different arrival times of the ions at the detector. The 10 ns pulse duration was achieved by subtracting the two measurements with a pulse duration of 80 ns and 90 ns, such that each data point of the resulting TOF contains data for a 10 ns gate only. Four local maxima are shown in Figure 5.1 a) for a TOF with 90 ns pulse width (PW) (blue), which are shifted by ∼10 ns to later arrival times for the 80 ns PW. The underlying peaks are not well separated and it is not possible to define the mass-to-charge ratio properly. Using the gate-subtraction method, well-separated maxima at masses of 16 u/e, 17 u/e, 18 u/e and 19 u/e, corresponding to O^+, OH^+, H_2O^+ and H_3O^+ become visible (green). This method thereby allows us to distinguish the signals from the different fragments after strong-field ionization of the water dimer.

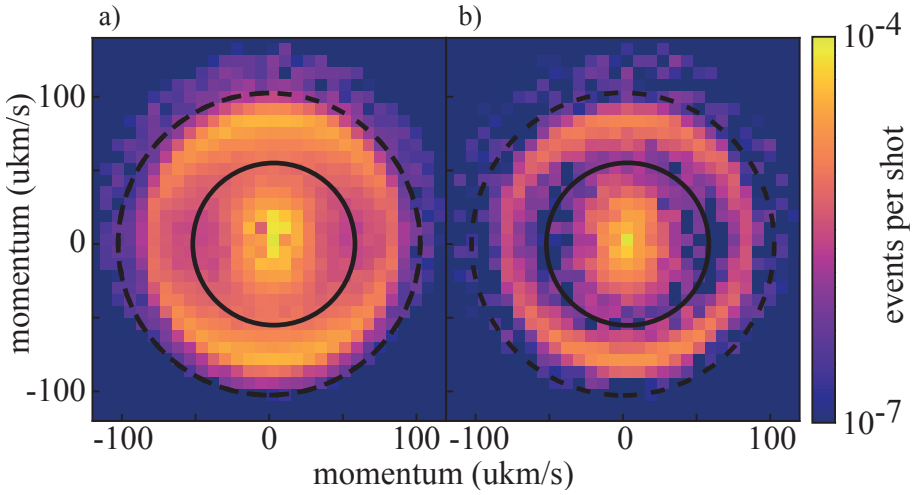

Figure 5.2: MMIs of ions with an arrival time of a) 2.30 μs and b) 2.305 μs corresponding to H_2O^+ using a pulse width of a) 80 ns and b) 10 ns. The black rings at ∼60 ukm/s and ∼100 ukm/s define the areas of the maximum in the center (solid line) and the local maximum on a ring (dashed line).

The measured VMIs were converted to momentum. These momentum map images (MMI) of H_2O^+ with a PW of a) 80 ns and b) 10 ns are shown in Figure 5.2. A PW of 10 ns was achieved by subtracting the MMI using a PW of 80 ns from the MMI using a PW of 90 ns. Both MMIs show a maximum intensity in the center with low momenta and a ring at high momenta with a maximum around 80 ukm/s.

SFI of a molecule can cause a fragmentation into several neutral molecules and ions that belong to a specific dissociation process, which can be identified using a pure sample of water dimer. Depending on the number of charges initially created in the water dimer, the momenta of fragments with the same masses differ from each other [195]. Here, the detected ions can be sorted to originate from two initial processes of single and double ionization of the water dimer defined by the minima of the Abel-inverted images of Figure 5.2, shown as black circles.

A TOF for ions arriving in the single ionization region (inside the solid circle) or in the double ionization region (between the solid and dashed line) are shown in Figure 5.1 b) and c), respectively. To obtain the TOF, the Abel-inverted MMIs have been integrated over the single ionization area for each timing corresponding to a momentum of up to ∼60 ukm/s, as depicted by the solid circles in Figure 5.2. In case of a PW of 80 ns (orange) and 90 ns (blue) maxima occurred that were not well separated. Using the gate-subtraction method, two well-separated ion maxima at 18 u/e and 19 u/e occurred in Figure 5.1 b) corresponding to low-momentum H_2O^+ and low-momentum H_3O^+. For a TOF of ions in the high-momentum region and after gate subtraction shown in Figure 5.1 c) (green), the maximum is at 18 u/e and three additional local maxima occurred at 16 u/e, 17 u/e and 19 u/e, which couldn't be identified without the gate-subtraction method. To verify the result after gate-subtraction, a simulated TOF using SIMION [144] is shown in Figure B.1

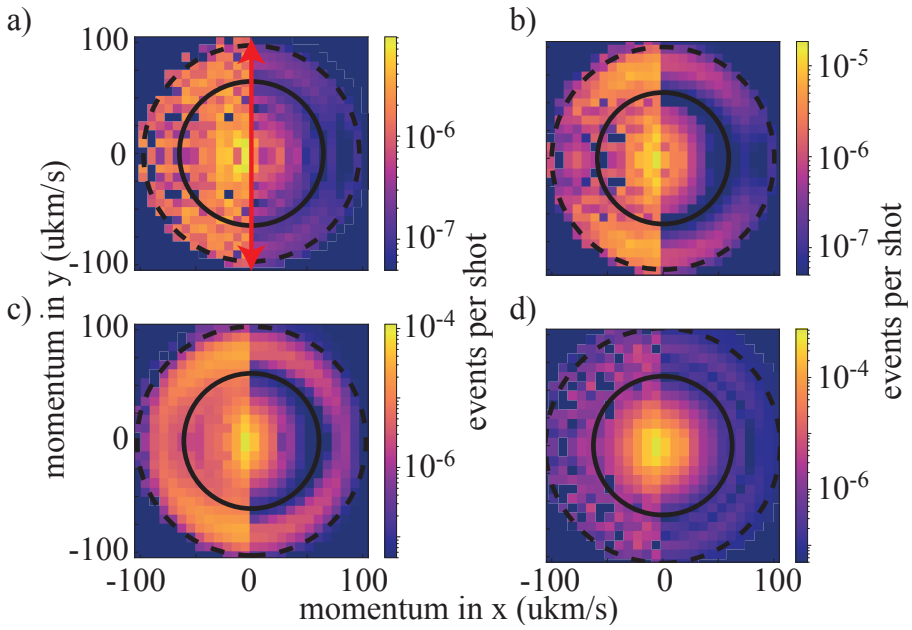

Figure 5.3: MMIs (left) and its Abel inversion (right) of a) O^+, b) OH^+, c) H_2O^+ and d) H_3O^+. The polarization axis is along the y-axis (red arrow). The black rings define the areas of single ionization (solid line) at ∼60 ukm/s and double ionization (dashed line) at ∼110 ukm/s.

of the supplemental information (Suppl. Inf.). The MMIs for a) O^+, b) OH^+, c) H_2O^+ and d) H_3O^+ and their Abel-inversion using the Maximum Entropy Velocity Legendre Reconstruction (MEVELER) method from Bernhard Dick [196] are shown on the right and on the left halves of Figure 5.3 a)-d), respectively.

For O^+, a rather smooth distribution with an anisotropic angular distribution in the y-direction and a slight maximum in the center is shown in Figure 5.3 a) (left). After inversion (right), a second maximum forming a ring with a stronger anisotropic angular distribution was visible. The OH^+ had a spot in the center and a ring at 80 ukm/s in Figure 5.3 b) with an anisotropic distribution in the y-direction along the polarization axis, shown as a red arrow in Figure 5.3 a). The H_2O^+ is shown in Figure 5.3 c) and had a maximum intensity in the center (black circle) of the MMI and also a ring at 80 ukm/s with an anisotropic distribution in the y-direction. The H_3O^+ in Figure 5.3 d) had a maximum intensity in the center and a weak ring at 80 ukm/s was appearing after inversion.

5.3.2 Fragmentation Pathways

The radial distributions of the inverted images for O^+ (orange), OH^+ (dark blue), H_2O^+ (light blue) and H_3O^+ (green) are shown in Figure 5.4 a). The radial distributions of all fragments show two local maxima with varying intensities and momenta. Ions with low momenta up to ∼60 ukm/s predominantly originated from single ionization of the water dimer followed by a neutral dissociation into one ion and a neutral molecule. Ions

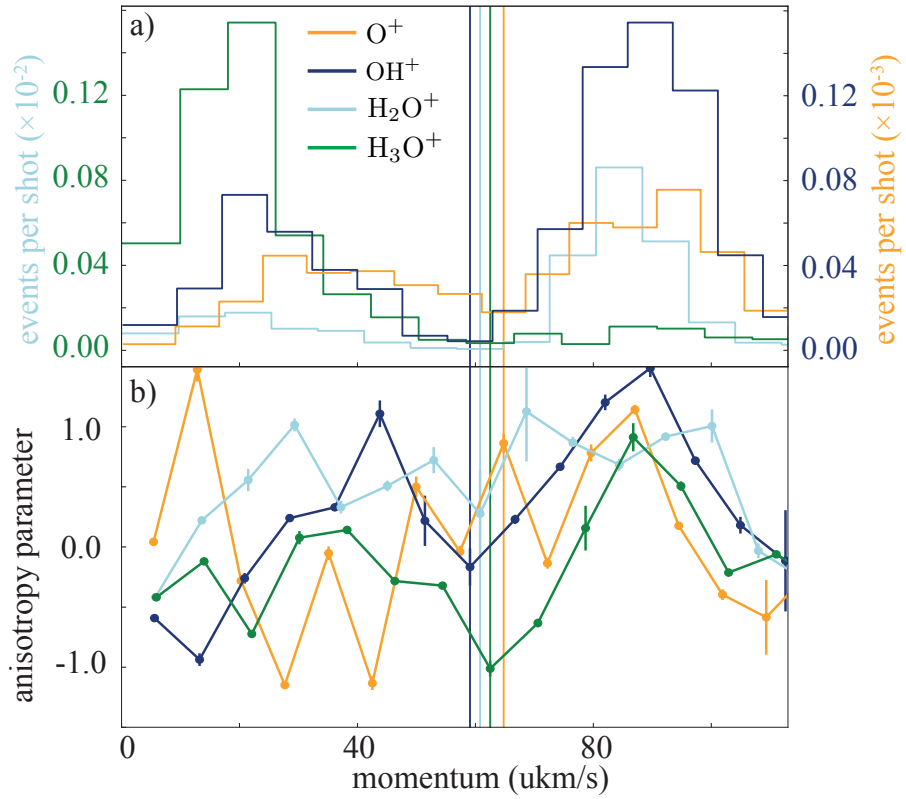

Figure 5.4: a) Abel-inverted radial distributions of O^+ (orange) and OH^+ (dark blue) (right y-axis), and H_2O^+ (light blue) and H_3O^+ (green) (left y-axis). b) Anisotropy parameter β of O^+ (orange), OH^+ (darkblue), H_2O^+ (light blue) and H_3O^+ (green).

with momenta in the region between ~60 ukm/s to ~110 ukm/s belonged to processes occurring following double ionization of the dimer. Thus, two detected ions in the regime of the double ionization must belong to one fragmentation process.

The relative ion yields of the measured fragments of single and double ionization are listed in Table T1 and the branching ratios were calculated. For a single ionization, previous publications [92] using electron impact ionization have shown, that the neutral partner for a fragmentation of a water dimer into H_2O^+ is an H_2O and for H_3O^+ is a neutral OH. As a neutral H_3O is unlikely, one option for a fragmentation following single ionization involving OH^+ is a fragmentation process of $OH^+ + H + H_2O$. For an O^+ the corresponding masses for the rest must add up to an H_4O, while the real neutral partners are unknown. But assuming neutral partners $H_2O + H$ could be an option. This gives the following possible single ionization fragmentation pathways:

$$(H_2O)_2 + h\nu \rightarrow (H_2O)_2^+ + e^- \rightarrow H_3O^+ + OH + e^-, \tag{5.1}$$

$$(H_2O)_2 + h\nu \rightarrow (H_2O)_2^+ + e^- \rightarrow H_2O^+ + H_2O + e^-, \tag{5.2}$$

$$(H_2O)_2 + h\nu \rightarrow (H_2O)_2^+ + e^- \rightarrow OH^+ + H_2O + H + e^-, \tag{5.3}$$

$$(H_2O)_2 + h\nu \rightarrow (H_2O)_2^+ + e^- \rightarrow O^+ + H_2O + 2H + e^-. \tag{5.4}$$

Due to the high purity of the molecular beam, we can exclude that H_2O^+ in the single ionization region can come from a single ionized H_2O from the molecular beam, which would have a different momentum distribution. A covariance map, which will be discussed in the next paragraph in more details for a double ionization process, of ions in the region of 0 to 60 ukm/s has shown that there were no correlations available for H_2O^+. This supports our findings that H_2O^+ ions with low momenta up to 60 ukm/s were fragments from a single ionization process. Contrary to the results in [99], that there was no contribution from a single ionized H_2O^+, we measured that 24 % of the measured water came from a dissociation after single ionization of water dimers.

Fragmentation processes that originated from a Coulomb explosion following a double ionization had two charged fragments involved. As the detection method allowed to measure only ions with the same mass in coincidence, it was not possible to identify correlations of two ions with different masses, such as OH^+ and H_3O^+ as theoretically predicted in [102] and measured in [99]. Nevertheless, a covariance map can identify whether a fragmentation into ions of the same mass were created, such as $H_2O^+ + H_2O^+$. Covariance maps of the angle θ of OH^+, H_2O^+ and H_3O^+ are shown in Figure 5.5, where θ is the angle between the detected ion in respect to the laser polarization axis. Only laser shots, where two ions with a momentum in the Coulomb explosion range between $\sim$60 ukm/s to $\sim$110 ukm/s were created within one laser pulse, were taken into account.

These covariance maps allow to investigate the correlation of two measured ions. The shape of the lines can also give information about the axial recoil and molecular alignment [197]. The covariance map of OH^+ showed two blurred lines, marked as red ellipses in Figure 5.5 a), while H_2O^+ and H_3O^+ showed two distinct lines. In Figure 5.5 b) for H_2O^+, also two blurred regions, marked by black circles, were visible, which arise due to false coincidences.

The distinct lines in Figure 5.5 b) of H_2O^+ and c) of H_3O^+ were correlated ions. As the lines have a small width, these ions flew apart axially from each other with an angle of around 180° between the momentum vectors of the fragmental ions. The length of the lines can give some information about the alignment of the molecular ions [197]. As the lines have a broader length, the molecules were not aligned. The correlated H_2O^+ resulted from a Coulomb explosion following double ionization of the water dimer into

$$(H_2O)_2 + h\nu \rightarrow (H_2O)_2^{++} + 2e^- \rightarrow 2H_2O^+ + 2e^-. \tag{5.5}$$

As the lines in Figure 5.5 a) for OH^+ were broader than for H_2O^+, these were correlated

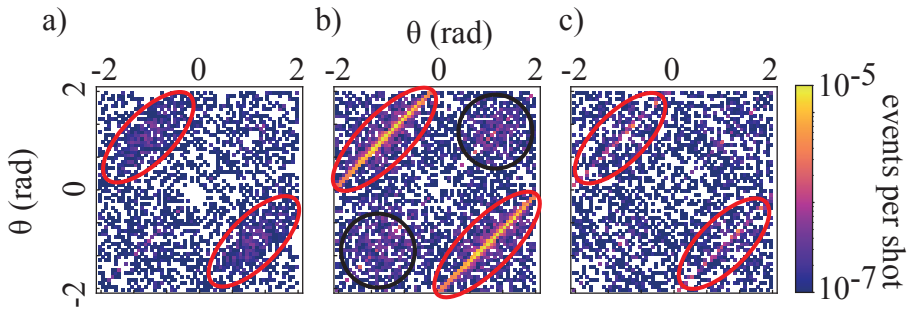

Figure 5.5: Covariance map of a) OH^+, b) H_2O^+ and c) H_3O^+ for laser shots with only two detected ions in the momentum range between ∼60 ukm/s and ∼110 ukm/s. The x-axis gives the angle θ of the first and the y-axis of the second ion. The red ellipse marks the regions of correlated ions and the black ellipse false coincidences.

ions that flew apart axially but with an angle below 180°. As the mass of two OH^+ does not add up to the mass of a water dimer, another ion must be involved in the fragmentation process. The momenta of the missing ions can be calculated by subtracting the momenta of two correlated ions that end up on the areas marked by the red ellipses in Figure 5.5 a), which were of the order of ∼20 ukm/s. Thus, for a fragmentation process of water dimer involving two OH^+, two H-atoms would be expected as additional partners with each having a momentum of ∼10 ukm/s. This lead to the following fragmentation process:

$$(H_2O)_2 + h\nu \rightarrow (H_2O)_2^{++} + 2e^- \rightarrow 2OH^+ + 2H + 2e^-. \tag{5.6}$$

The fragmentation channel involving two H_3O^+, must be a product from a larger water cluster as the sum of the masses had a larger mass than water dimer. Deflection simulations have shown, that the impurity of the water dimer beam could be caused by a water hexamer [194]. Thus, ions of H_3O^+ that ended up on the lines in Figure 5.5 c) won't be involved in the following analysis. These made a contribution of 0.8 % of H_3O^+ in the double ionization regime which came from larger water clusters, which is below the estimated impurity of the molecular beam given in [194].

From the covariance map, it can be seen that H_2O^+ came from a double ionization process fragmenting into $H_2O^+ + H_2O^+$. The ratio between correlated and uncorrelated ions can be used to investigate wether the fragmentation channel of $H_2O^+ + H_2O^+$ was the only double ionization process containing H_2O^+. This ratio was calculated to be 0.85, neglecting the contribution from larger water clusters and taking laser pulses into account, where only two created ions per laser shot were detected in the area of double ionization. This made a maximal contribution from another process than $H_2O^+ + H_2O^+$ of around (15.5 ± 0.5) % of the measured H_2O^+ in the double ionization regime, which will be neglected in the following. Instead, we assume that all measured H_2O^+ in the marked area of double ionization belong to the $H_2O^+ + H_2O^+$ process.

A fragmentation channel of $H_3O^+ + OH^+$ following SFI was reported by [99]. Due

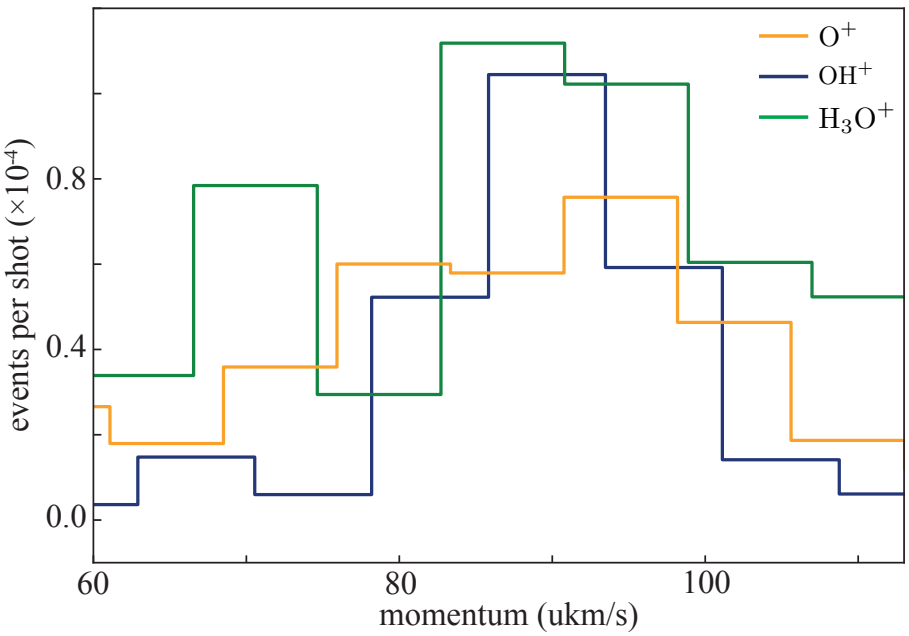

Figure 5.6: Radial distribution of the inverted MMI of O^+ (orange), OH^+ (darkblue), and H_3O^+ (green) originating from double ionization. The contribution of the OH^+ corresponding to a process of $OH^+ + OH^+ + 2H$ has been deleted from the OH^+ signal to compare the momenta with H_3O^+.

to our detection method, a direct correlation of H_3O^+ with another ion could not be measured. But momentum comparison can help to confirm the fragmentation process. The radial distributions of O^+ (orange), OH^+ (darkblue), and H_3O^+ (green) in the region of double ionization are shown in Figure 5.6. From the covariance analysis, the radial distribution of OH^+ from $OH^+ + OH^+ + 2H$ could be obtained and subtracted from the radial distribution of OH^+ in Figure 5.4 a), such that Figure 5.6 shows the radial distribution of not correlated OH^+ to compare the momenta with H_3O^+. All maxima of O^+, OH^+ and H_3O^+ were located at the same momentum, which lead to the following decay channels of

$$(H_2O)_2 + h\nu \rightarrow (H_2O)_2^{++} + 2e^- \rightarrow H_3O^+ + OH^+ + 2e^- \tag{5.7}$$

and

$$(H_2O)_2 + h\nu \rightarrow (H_2O)_2^{++} + 2e^- \rightarrow H_3O^+ + O^+ + H + 2e^-. \tag{5.8}$$

Using the covariance map analysis and the momentum comparison of the measured ions, we could reveal that we have measured fragments from a Coulomb explosion following a double ionization into $H_3O^+ + OH^+$, $H_3O^+ + O^+ + H$, $OH^+ + OH^+ + 2H$ and $H_2O^+ + H_2O^+$. While the two fragmentation pathways into $2H_2O^+$ and $H_3O^+ + OH^+$ were reported previously using SFI [99], the fragmentation channels into $H_3O^+ + O^+ + H$, $OH^+ + OH^+ + 2H$ have not been reported before.

Fragmentation process	Branching ratio
single ionization	0.76
$O^+ + H_4O$	0.04
$OH^+ + H_3O$	0.05
$H_2O^+ + H_2O$	012
$H_3O^+ + OH$	0.79
double ionization	0.24
$OH^+ + OH^+ + H + H$	0.11
$H_2O^+ + H_2O^+$	0.67
$H_3O^+ + O^+ + H$	0.14
$H_3O^+ + OH^+$	0.08

Table 5.1: Branching ratios of the single and double ionization of water dimer. The branching ratios of single and double ionization processes were calculated independently. The ratio of all single to all double ionization processes is 0.76, while the double ionization contribution is 0.24.

5.3.3 Branching Ratios

With the previous analysis and the ion yields in Table B.1, the branching ratios P_i of the fragmentation process i were calculated by

$$P_i = \frac{N_i}{\sum_i N_i}, \tag{5.9}$$

with N_i as the ion yield of the fragmentation process i divided by the sum of the contribution of all single or double ionization processes, as the branching ratios of single and double ionization were calculated independently. For the double ionization, the ion yields of H_2O^+ were reduced by (15.5 ± 0.5) % coming from larger water clusters and by a factor of two, taking into account that two H_2O^+ were involved in the fragmentation process. Also the ion yield of H_3O^+ resulting from a dissociation of a double ionized dimer, was adapted and reduced by 0.8 % expecting to come from larger water clusters. The ratio between OH^+ to O^+ from double ionized water dimer was used as a reference for the ratio of $H_3O^+ + OH^+$ to $H_3O^+ + O^+ + H$. The branching ratios are listed in Table 5.1.

Overall, the ratio of single to double ionization was 0.76:0.24. After single ionization, the most dominant break-up was into $H_3O^+ + OH$ followed by a break-up into $H_2O^+ + H_2O$. Fragmentation after double ionization was dominated by a break-up into $H_2O^+ + H_2O^+$. A ratio of 0.081 ± 0.003 of $N_{H_3O^+ + OH^+} / (N_{H_2O^+ + H_2O^+} + N_{H_3O^+ + OH^+})$ was reported by [99], while we achieved a ratio of 0.12. The difference can occur due to the missing fragmentation pathways in [99], where they neglected the single ionization of H_2O^+ and the double ionization channels into $2OH^+ + 2H$ and $H_3O^+ + O^+ + H$.

5.3.4 Anisotropies

In general, the angular distributions for the ionic products of doubly ionized water dimer is anisotropic. This angular distribution can be described by the anisotropy function [145,

Fragment	β
single ionization	
O^+	0.7 ± 0.8
OH^+	0.8 ± 0.6
H_2O^+	1.1 ± 0.4
H_3O^+	0.4 ± 0.3
double ionization	
O^+	1.0 ± 0.6
OH^+	1.0 ± 0.5
H_2O^+	1.3 ± 0.3
H_3O^+	0.6 ± 0.7

Table 5.2: Anisotropy parameter of the water dimer fragments in the region of single and double ionization.

146]:

$$P(\theta) \propto \frac{1}{4\pi}(1 + \beta P_2(\cos\theta)), \tag{5.10}$$

with $-1 < \beta < 2$ being the recoil anisotropy parameter and $P_2(\cos\theta)$ the second-order Legendre polynomial with θ being the angle between the recoil velocity of the fragment and the laser polarization vector. A β value of 0 results from an isotropic recoil, while $-1 < \beta < 0$ stands for a perpendicular and $0 < \beta < 2$ for a parallel recoil of the fragments with respect to the laser polarization axis [197].

The anisotropy parameter β for O^+ (orange), OH^+ (dark blue), H_2O^+ (light blue) and H_3O^+ (green) are shown in Figure 5.4 b). All ions showed a maximal β parameter and a recoil parallel to the laser polarization axis at around (80-95) ukm/s with β values between 0.5 and 2. For lower momenta, the anisotropy parameter was varying much more, but it was overall more isotropic than for the high-momentum region with values between -0.6 to 2.0 for O^+, -0.5 and 1.6 for OH^+, 0 to 1.5 for H_2O^+ and -0.2 to 0.5 for H_3O^+.

To obtain the anisotropy parameter for the fragments after single and double ionization of water dimer, the β-parameter were calculated by integrating over the marked areas of the single and double ionization regimes in Figure 5.4. These anisotropy parameter β are listed in Table 5.2 and the corresponding angular distributions are shown in Figure B.2 of the Suppl. Inf.. The OH^+ and H_3O^+ from single ionization had a mainly isotropic distribution, while O^+ and H_2O^+ showed an isotropic to parallel recoil to the laser polarization axes. For a double ionization process, all fragments originated from a mainly parallel recoil to the laser polarization axis. This axial recoil was the strongest for OH^+ followed by H_2O^+.

The recoil anisotropy β depends from the angle dependence of the cross section, the dissociation time and the axial recoil. Thus, if the alignment axis of the molecule is known, it can give some estimation about the dissociation lifetimes of the specific dissociation channels. As the water dimers were isotropic distributed, only a qualitative discussion can be given here. O^+, OH^+ and H_3O^+ resulting from a dissociation after single ionization had an isotropic distribution. As ions in the center region of the MMIs have a smaller

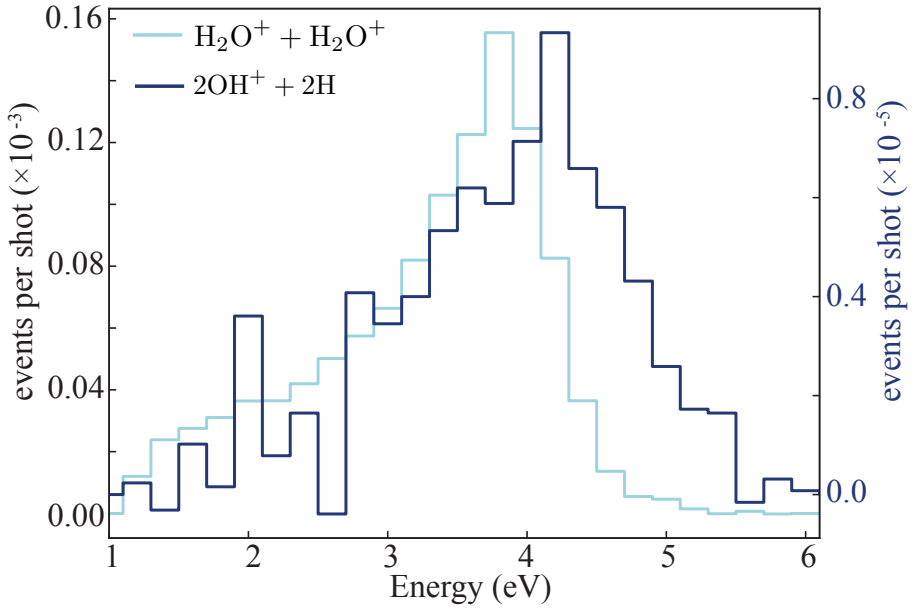

Figure 5.7: Kinetic Energy Release of the fragmentation channels $H_2O^+ + H_2O^+$ (light blue) and $OH^+ + OH^+ + 2H$ (dark blue).

momentum and, thus, a slower velocity than ions from a Coulomb explosion following double ionization, the isotropic distribution might arise due to a slow dissociation time compared to the molecular rotation period of the parent ion [195, 198, 199]. The H_2O^+ fragment as a result from a single ionization showed a parallel recoil to the laser polarization axis. This might occur due to the symmetric break-up of the single ionized water dimer into $H_2O^+ + H_2O$, while the break-up into other fragmental ions lead to a non-symmetric break up and to a non-axial recoil. The double-ionized water dimer lead to fragmental ions of O^+, OH^+ and H_2O^+ with a large anisotropy parameter and an axial recoil, which might be explained due to a faster dissociation process. Only H_3O^+ had a mainly isotropic distribution, which again might result from a non-symmetric break-up of the water dimer based on its geometry.

5.3.5 Kinetic Energy Release

Furthermore, we have analyzed the KER for the fragmentation processes of $H_2O^+ + H_2O^+$ and $OH^+ + OH^+ + 2H$, which resulted from a Coulomb explosion process, shown in Figure 5.7. The KER of correlated H_2O^+ (light blue) had a maximum at 3.8 eV with a FWHM of 1.2 eV. In case of a break-up $OH^+ + OH^+ + 2H$ (darkblue), the contribution of the not detected two H was estimated by subtracting the kinetic energies of two correlated ions to be at most 0.1 eV. A maximum of the KER had been measured at 4.2 eV with a FWHM of 1.4 eV.

From the KER, the distance R of the positive charges of the ionized water dimer can be estimated using the Coulomb explosion model [139]. In case of $H_2O^+ + H_2O^+$, this corresponds to a charge distance of $R = 380 \pm 70$ pm. As the correlation information

would get lost after inverting the MMIs, the ion signals of the original measurement were used for this calculation to identify the fragments that belong to one Coulomb explosion process and to sum up their energies. Thus, the projection of a 3D-sphere onto a 2D image has not been taken into account, leading to a rather long tale toward smaller energies. In a previous experiment, a charge separation of 339 pm (6.4 a.u.) using COLTRIMS with SFI [99] was estimated also using the Coulomb explosion model for the process of $H_2O^+ + H_2O^+$, which is in the range of our given error bar.

To verify the location of the charges inside the water dimer, the obtained distances can be compared to the positions of the atoms inside the water dimer. Assuming a charge location at the lone-pair orbitals of the two oxygen atoms and a direct vertical double ionization of the water dimer, one would expect to measure an OO distance that is close to the OO distance of a neutral water dimer. In case of a synchrotron experiment using 43 eV photon energy [67], a charge distance of 290 pm was measured for the water dimer before a break up into $H_2O^+ + H_2O^+$, expecting an ICD process, which fits the experimental observed OO distance of the neutral water dimer of 298 pm [56–58]. However, ICD is a fast process, while SFI is sensitive for many ionization states and also sequential double ionization can occur due to the laser pulse length of 30 fs. Both leading to a difference of the measured OO distance of the neutral water dimer. Theoretical calculations have shown that the OO distance can vary for different ionization states. For the water dimer cation in the ground state $^2A''$, an OO distance between 219.5 pm and 281.6 pm was calculated, while for the first excited state, a distance up to 320 pm was predicted [96]. These values are smaller than our measured charge distance. As the Coulomb repulsion model does not take the shielding of other electrons into account, a difference in the calculated charge separation is expected. However, the charges of the water dimer might also not be located at the oxygen atoms, but instead at the hydrogen atoms. Previous studies, have investigated the equilibrium geometry of the water dimer [57, 58]. From this, the distances between the two outermost hydrogen atoms can be calculated with an OO distance of 298 pm, a distance from the donor oxygen to the outer hydrogen of $R_{OH} = 24$ pm and a distance of the acceptor of $R_{OH} = 52$ pm to be $R_{HH} = 374$ pm, which is close to our measured charge separation distance.

The KER of a break up into $OH^+ + OH^+ + 2H$ corresponds to a charge distance of 343 ± 50 pm and let us assume to originate from a higher ionization state.

5.4 Conclusions

A pure sample of water dimer was used to study the fragmentation pathways following strong-field single and double ionization with a laser intensity of 4×10^{14} W/cm^2. We have furthermore demonstrated a slicing method that has been used to improve the resolution of the experiment. With this method, new fragmentation pathways that have not been previously observed containing a single charge of O^+, OH^+, H_2O^+ and H_3O^+, as well

as a Coulomb explosion into $OH^+ + OH^+ + 2H$ and $H_3O^+ + O^+ + H$ were observed. It was shown that single ionization was with a ratio of 0.76 to double ionization more likely than a double ionization process, which was dominated by a proton transfer with a break-up into a $H_3O^+ + OH$ and a branching ratio of 0.79. Double ionization lead most often to a Coulomb explosion into $H_2O^+ + H_2O^+$ with a branching ratio of 0.67. In addition, the anisotropy parameter was calculated and shown that a single ionization was resulting in an isotropic to parallel recoil of the fragments, while the Coulomb explosion following a double ionization lead to a parallel recoil of OH^+ and H_2O^+. The obtained covariance maps of the fragmentation processes of $OH^+ + OH^+ + 2H$ and $H_2O^+ + H_2O^+$ have further shown, that the two H_2O^+ experienced an axial recoil with an angle θ of around 180°, while the two OH^+ have an axial recoil with an angle below 180°. Further, the kinetic energy release of the Coulomb explosion channels could be investigated and the charge separation distance of the ionized water dimer modeled with a Coulomb repulsion method to be around $R = 380 \pm 130$ pm for $H_2O^+ + H_2O^+$ and 395 ± 155 pm for $OH^+ + OH^+ + 2H$. The described experiment in combination with a time- and position sensitive detector, such as Timepix [200–203], and a double sided VMI, also measuring electrons in coincidence, or a reaction microscope can clarify which ionization states are causing which fragmentation products. Further, this can be used to study site-specific ionization using soft X-ray in the photon energy range of the donor or acceptor oxygen.

6 Conclusion and Outlook

The following chapter contains a summary of the main results in Section 6.1 and an outlook in Section 6.2. The outlook covers the future perspectives on the research of water dimers using especially X-rays and coincidence detection schemes, such as Photoelectron-Photoion-Photoion coincidence (PEPIPICO) and a description how larger biomolecules and water clusters could be investigated, in future, based on the results obtained throughout this thesis, to understand the connection of liquid water and life.

6.1 Conclusion

The goal of this thesis was to understand the photophysics and photochemistry of the water dimer, including hydrogen bond formation and breaking, dissociation and fragmentation processes. To this end, the behavior of water dimers in electric fields was investigated experimentally and theoretically. Further, the behavior of the water dimer in an electric field taking non-rigid vibrations into account was modeled and the fragmentation processes, the branching ratios of the water dimer and the anisotropy parameters and the kinetic energy release of the water dimer fragments were experimentally investigated using SFI.

The experimental techniques employed for that purpose were presented and explained in Section 2.4, these includes techniques to generate, study and image a pure size-selected water-dimer beam. Using these techniques, a sample containing 93(15) % water dimer was created by using an inhomogeneous electric field in chapter 3. With a simulation of the deflection behavior of the water dimer, the initial rotational temperature of the water dimer sample could be determined to be 1.5(5) K.

As the water dimer is known to be a non-rigid molecule, the Stark energies were calculated taking intermolecular vibrations into account, in chapter 4. First, in Section 4.1, the influence of each motion was investigated and it has been shown that the torsional motion had the biggest effect on the averaged electric dipole moment of the water dimer. Second, in Section 4.2, an adiabatic approximation was used to calculate the Stark energies of the non- rigid water dimer, assuming non-interacting intermolecular vibrational motions. It has been shown that the adiabatic description leads to similar deflection profiles of single states, but that different nuclear spin weightings are slightly changing the overall vertical molecular beam profile. Nevertheless, the experimental results have shown that the rigid rotor approximation, as used by CMIstark, is a good approximation to calculate the Stark interaction of the non-rigid water dimer.

In chapter 5, the pure sample of water dimer was used to study strong-field ionization processes. Single and double ionization were detected leading to the same fragmentation products with different kinetic energies, such that the fragmentation pathways could be

inferred and new fragmentation process of $OH^+ + OH^+ + H_2$ was found.

6.2 Toward a Molecular Movie of Water-Clusters Networks

Femtosecond multiphoton or tunneling ionization was used in this thesis and the work of others [63, 64, 99] in order to investigate photophysical processes and fragmentation dynamics of the water dimer. However, radiation in the X-ray regime could lead to a better understanding of relaxation [204, 205], charge redistribution [204, 206] and interatomic Coulombic decay (ICD) [67, 207] processes. Combining the generation of a pure size-selected water-dimer beam with X-rays and with coincidence detection schemes, such as a PEPIPICO spectrometer [208] or reaction microscopes (COLTRIMS) [209, 210], even fragmentation channels could be identified by measuring ions and electrons. Therefore, one way to detect ions and electrons in coincidence is a double sided VMI spectrometer, which allows for 2D and 3D momentum detection of electrons and ionic fragments.

This combination of X-ray radiation and PEPIPICO was already employed [192, 211–215] in previous beamtimes by Controlled Molecule Imaging (CMI). At the synchrotron facility Petra III in 2017 and 2018, we investigated the photophysics and charge redistribution of pure samples of indole, indole-water, pyrrole, pyrrole-water and water dimer. Due to technical reasons, only data for a short amount of time could be recorded for water dimer and, therefore, it was not possible to record high-quality data. A Photoion-Photoion coincidence (PIPICO) spectrum of a molecular beam containing water clusters is shown in Figure 6.1. Different areas of the PIPICO map are marked with blue and black circles. These are assigned to fragmentation channels from water and water dimers, respectively. For water, coincidences between OH^+ and H^+ and very few coincidences between O^+ and H_2^+ were detected. Coincidences for water dimer contained fragmentation products of $H_3O^+ + OH^+$ and a few of $H_2O^+ + H_2O^+$. Using a pure molecular beam of water dimer with a larger statistic could help to identify the fragmentation products and to determine the branching ratios of the water dimer.

Dynamical processes can be triggered via site-specific ionization of molecules using X-rays due to their element selectivity [216, 217]. The difference in the ionization potential for the two oxygen atoms inside the water dimer is in the order of 1 eV [218]. Thus, using the above described experimental setup of a pure molecular beam of water dimer and a PEPIPICO spectrometer, the fragmentation pathways after ionizing the oxygen O(1s) of the donor and acceptor water molecule inside the water dimer could be studied by scanning the X-ray energy in the regime of 550 to 600 eV [219], such that the role of the hydrogen bond during relaxation and fragmentation processes via site-specific ionization could be investigated.

Further, dynamics of molecules can be studied using coherent nonlinear X-ray spectroscopy [220] or X-rays in a pump-probe experiment. At LCLS in 2017, we investigated

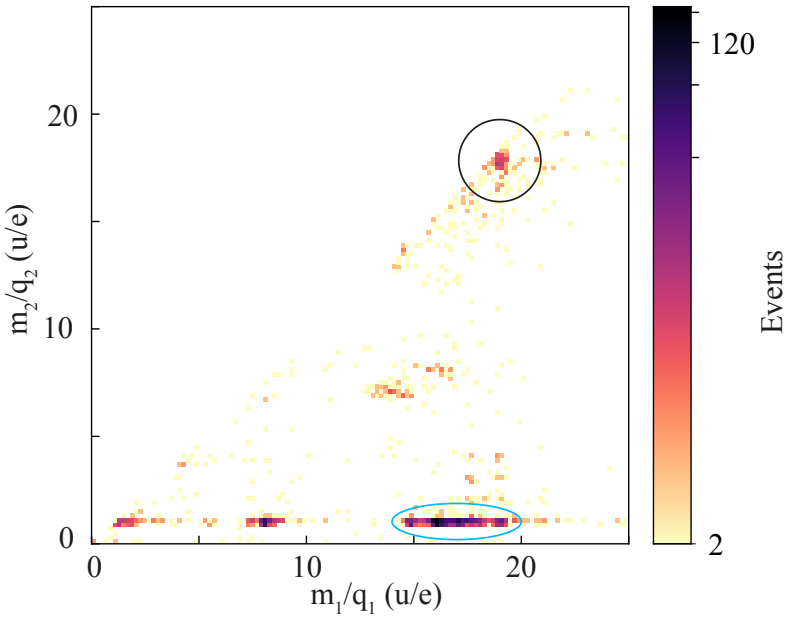

Figure 6.1: Coincidence spectra between the mass-to-charge ratio m_1/q_1 of the first and second m_2/q_2 detected ion per event using a molecular beam containing water clusters interacting with soft X-ray pulses with photon energies of 600 eV. The circles mark areas that belong to parent ions of H_2O (blue) and $(H_2O)_2$ (black).

the charge transfer inside an indole-water cluster by using a pump pulse of 266 nm and an X-ray probe pulse of 480 eV and 550 eV ionizing the nitrogen and the carbon atom in indole and the oxygen atom of the water molecule, respectively. This allowed us to study the charge transfer from indole to water and from water to indole. This setup could be adapted for investigating the water dimer using an IR-pump and an X-ray probe to induce relaxation dynamics and to study the proton transfer dynamics inside the water dimer, as suggested in [66].

The hydrogen bonding is involved in many dynamical processes of molecular systems [221–223]. Due to its single hydrogen bond, the water dimer is an ideal model system to investigate these processes. Therefore, a molecular movie [224–228], measuring the molecular motions in time, could help to track the dynamics of electrons and atoms inside molecules to reveal the dynamics around a hydrogen bond.

Moving toward larger water-cluster systems step by step could help to understand the influence of additional hydrogen bonds on the dynamics of larger systems, such as proteins, biomolecules and dipeptides, and to investigate the importance of water for life.

The creation of pure samples of large water clusters could be challenging using an electrostatic deflector, as the water dimer would be distributed over the whole vertical molecular beam profile. In addition, the water trimer, tetramer and pentamer have most likely a dipole moment of 0 D and, thus, can not be separated from the seeding gas or from each other, as shown in chapter 3. However, the number of unwanted water clusters can

still be reduced by the electrostatic deflector, making it easier to study larger water clusters. Therefore, water clusters could be investigated by coincidence measurements [229] using a time- and position sensitive detector, such as Timepix [230, 231], which would allow to disentangle fragmentation pathways and, thus, the parent ion of the measured fragments. In combination with an electrostatic deflector, fragments could be measured at different positions of the vertical molecular beam profile and the contributions from different water clusters could be disentangled by comparing the experimentally measured vertical molecular beam profiles with the simulations. Therefore, the simulations of the Stark energies and of the vertical molecular beam profiles must be calculated very accurately. Therefore, the development of general variational approaches for the modeling of the interaction of rovibrational motions and external fields for arbitrary polyatomic molecule is of high demand. As the adiabatic approximation, which is used in Section 4.2, is only valid for small field gradients and well-separated rotational states, it breaks down in case of large and non-rigid molecules with coupled degrees of freedom. In particular, at the edges of the electrostatic deflector large field gradients occur and increase the probability of non-adiabatic dynamics, such as transitions between rotational states. These non-adiabatic effects could further be simulated by using a Tully surface hopping algorithm [232], as done in CMI by Yahya Saleh [184], which could help to understand the behavior of large water clusters and other non-rigid molecules in electric fields in more details.

For a useful description of non-rigid molecules, it is important to understand the time-dependent structural changes going on inside molecules, which could be measured by using time-resolved X-ray diffraction [233] or laser induced electron diffraction (LIED) [234–236]. These allow for a high spatial and temporal resolution. In combination with a pump-probe system, snapshots of molecular clusters could be measured at different times and, thereby, used to create a molecular movie. As molecules are destroyed during the measurement process and an averaging over many molecules is required to obtain enough information, a strong control over the molecular sample, such as the isomer, quantum state, the alignment and orientation is required. Thereby, the anisotropy of the polarizabilities is defining whether a molecule is able to be aligned and oriented. While water monomers was aligned when confined in beryl single crystals to keep the dipole-dipole interaction intact and the hydrogen bonding suppressed [237], water-cluster polarizabilities were investigated theoretically [238, 239] and the possibility to align and orient water clusters could be further investigated to check wether these are useful candidates for measuring a molecular movie.

To bridge the gap between single isolated molecules and molecules in solvation, one could go toward larger cluster systems. Therefore, several techniques are available to enable cold molecular samples of large molecules, such as a laser-induced acoustic desorption (LIAD) [240–243] or a laser desorption setup [244–247]. By combining supersonic expansion with a laser desorption setup and an electrostatic deflector [248] the two conformers of the dipeptide Ac-Phe-Cys-NH_2 have been separated [21], such that we were

able to investigate their photofragmentation patterns at a beamtime at the electron laser facility FLASH in 2018. As a next step, the influence of water onto biomolecules could be investigated by adding one water molecule at a time to this or other molecules, as done for indole- water [148] and pyrrole-water [19]. Further, biologically relevant proteins could be studied embedded in water clusters, water droplets and aqueous solutions to bridge the gap between gas-phase water complexes and aqueous solutions.

Understanding the role of water as a biological solvent is still a riddle, which could be solved by studying electronic and geometric structural changes in real-time. Synchrotrons allow to measure dynamical effects down to hundreds of picoseconds, while with free electron laser facilities dynamics of around tens of femtoseconds can be resolved. Until now most proteins are measured as crystals in X-ray diffraction experiments, which are not comparable to their natural behavior and, thus, should be measured in its natural environment: water. Several X-ray spectroscopy [249] and X-ray scattering [250] methods could be combined to investigate the structural and electronic changes of water complexes in different thermodynamic phases [251, 252]. Also optical measurements such as transient absorption spectroscopy using THz pulses [253] or time-resolved photoelectron and photoion spectroscopy using high-order harmonic generation (HHG) sources [254] could complement X-ray studies to gain a full molecular picture on structural dynamics to understand how proteins and water interact with themselves and with each other.

Not only the interaction of water onto biomolecules under normal conditions, but also understanding water under extreme conditions is of great interest [255, 256] for the understanding of waters exceptional anomalies [257]. The above described experimental methods could be adapted for a broad range of temperatures and pressures also in the supercooled and -pressurized regimes. Investigating water samples in different thermodynamical phases could help to understand the complex polymorphism of crystalline and amorphous ice, which could finally reveal the connection between the low- and high-density amorphous ice and the low- and high-density liquid water [258].

The presented studies helped to further investigate the photophysical and photochemical processes of the smallest drop of water, the water dimer, and is the first step to resolve the mystery of the influence of water on life. Therefore, the suggested experiments could be used to study larger cluster systems in combination with water to investigate solvation dynamics.

A Supplemental Information for chapter 3

Fragmentation correction of measurements

The strong-field-ionization technique employed in this work can lead to fragmentation, such that clusters from the molecular beam contributed to smaller masses in the mass spectrum (MS). For example, the water-monomer and the water-dimer signals at $m/q =$ 18 u/e and 36 u/e, respectively, contained contributions due to fragmentation of larger water clusters in the molecular beam. Therefore, measured intensities needed to be corrected for these fragmentation channels. In addition, background water inside the chamber was measured at 18 u/e and needed to be corrected for.

For the latter, background measurement were permanently performed during the experiments using the higher repetition rate of the laser compared to the valve. Laser pulses were arriving in the interaction region at the same time as the molecular beam and between two molecular beam pulses, such that for each data point a background measurement was performed. The background signal was subtracted from the measurements.

The fragmentation ratios of the water dimer into smaller masses could be estimated and used for the calculation of the fraction of the water dimer in the deflected and undeflected molecular beam [19]. In Figure A.1 the deflection profiles measured at masses corresponding to H^+, O^+ and OH^+ are shown. In the region of 2.8 to 3.5 mm the deflection curves look identical to those for the water dimer, indicating that at these positions those are fragments from the water dimer. The ratios of the water dimer to H^+, O^+ and OH^+ at a position of 3 mm are 0.3, 0.8, and 0.7, respectively. For the calculation of the fraction of the water dimer in the molecular beam for the undeflected beam, these ratios were used to estimate the amount of the water dimer inside of the beam.

For larger clusters, only fragments were measured, such that the measured signal was not solely due to a specific cluster stoichiometry and the overall shape of the molecular beam profile arose from several larger water clusters. All protonated-water-cluster ions recorded showed the same deflection behavior, see Figure A.2. An estimate of the exponential decay of the measured protonated-water-clusters distribution showed that protonated water clusters $n = 1 - 10$ contained 99.6 % of the overall intensity.

Trajectory Simulations

The Stark energies and effective dipole moments μ_{eff} of water clusters $n = 1 \ldots 7$ were calculated using the freely available CMISTARK software package [126], which were then used to perform trajectory simulations [174] to verify the measured deflection profiles of water clusters. The rotational constants, dipole moments and centrifugal distortion

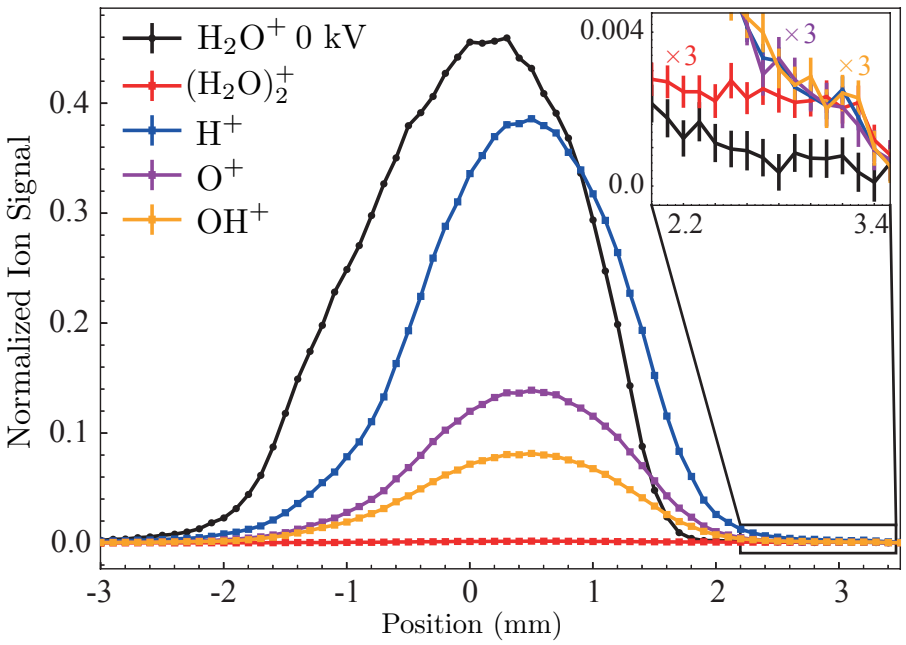

Figure A.1: Column density profiles, measured for the water-monomer cation with deflector voltages of 0 kV (black) and for H^+ (blue), O^+ (purple), OH^+ (orange) and the water-dimer cation with a deflector voltage of 8 kV (red). The inset shows the region around $y = 3$ mm enlarged, with O^+, OH^+ and the water-dimer ion scaled by a factor 3.

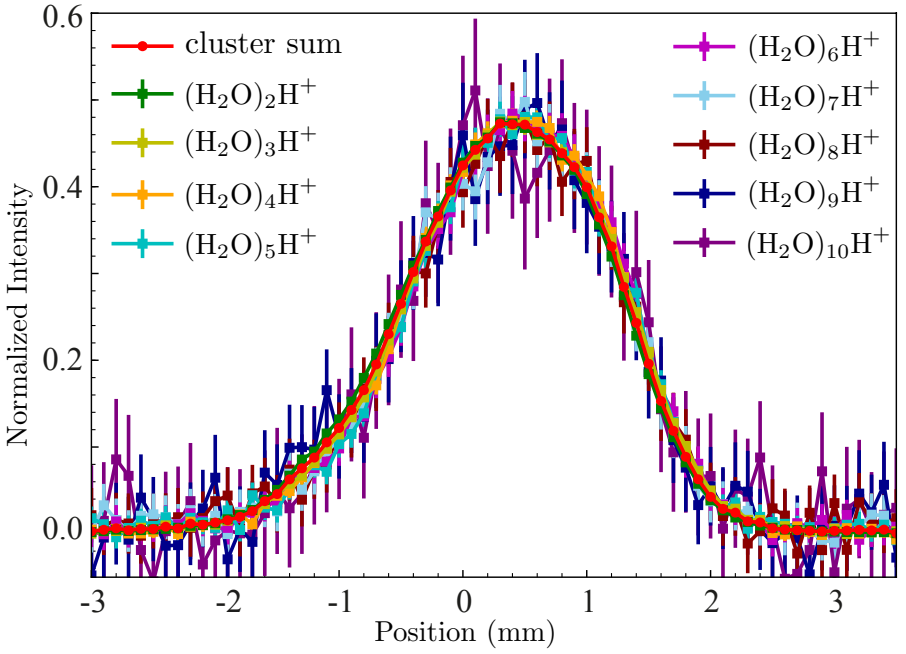

Figure A.2: Comparison of the averaged measured protonated-water-cluster signal (red) and the individual measured protonated-water-clusters deflection profiles for $n = 2 \ldots 7$. The profiles are normalized to the area under the curve.

molecule	dipole moment μ (D)				rotational constants (MHz)				Centrifugal Distortion constants (kHz)					
	μ_a	μ_b	μ_c		A	B	C		Δ_J	Δ_{JK}	Δ_K	d_J	d_K	
H_2O	0	−1.86	0	[127]	835840.29	435351.72	278138.70	[128]	3.759×10^4	-1.729×10^5	9.733×10^5	1.521×10^4	4.105×10^4	[128]
$(H_2O)_2$	2.63	0	0	[129]	190327.0	6162.76	6133.74	[130]	0.044	4010	0	0	0	[57]
$(H_2O)_3$	0	0	0	[106]	6646.91	6646.91	0	[131]	–	–	–	–	–	
$(H_2O)_4$	0	0	0	[106]	3149.00	3149.00	1622.00	[108]	–	–	–	–	–	
$(H_2O)_5$	0.93	0	0	[106]	1859.00	1818.00	940.00	[107]	–	–	–	–	–	
$(H_2O)_6$ book	0.17	2.46	0.16	[105]	1879.47	1063.98	775.06	[105]	–	–	–	–	–	
$(H_2O)_6$ cage	1.63	0.32	1.13	[105]	2163.61	1131.2	1068.80	[109]	–	–	–	–	–	
$(H_2O)_6$ prism	2.41	0.88	0.42	[105]	1658.22	1362.00	1313.12	[105]	–	–	–	–	–	
$(H_2O)_7$ 1	1.0	1.0	0.0	[104]	1304.44	937.88	919.52	[104]	0.457	−0.342	0.842	0.0377	0.63	[104]
$(H_2O)_7$ 2	1.0	0.0	1.0	[104]	1345.16	976.88	854.47	[104]	0.044	0.000	0.000	0.0000497	0	[104]

Table A.1: Dipole moments, rotational constants and centrifugal distortion constants of water clusters used in the Stark-effect calculations

constants from the literature are summarized in Table A.1.

Three conformers for the water hexamer in prism-, book- and cage-like form [105] and two conformers of the water heptamer following the naming scheme of [104] were included.

For these simulations the water clusters were assumed to be rigid rotors. Since the water dimer is known to be a floppy molecule with large amplitude motions [58, 130], the corresponding energy spectra and the description of the interaction of the states would significantly complicate further analysis. Using a rigid rotor assumption enables an easier and faster description and it has been shown previously that this model can be used to describe the dynamics of indole(H_2O) in strong-electric- and laser-field alignment and orientation experiments [23, 259] and to fit pure rotational transitions of the water dimer to experimental measurements [57].

For the rotational states $J = 0 \ldots 2$ of the water monomer and the water dimer the Stark energies and the corresponding μ_{eff} as a function of the electric field strength are shown in Figure A.3. For the water dimer all relevant states are strong-field seeking and, hence, accelerated toward regions of stronger fields. For a nominal field strength of 50 kV/cm the μ_{eff} of the water dimer are significantly larger than for the water monomer, except from the $|J, K_a, K_c, M\rangle = |2, 0, 2, 0\rangle, |2, 1, 1, 1\rangle$ states, leading to a larger acceleration in the electric field. All the shown states have a small asymmetry splitting, see Table A.1, resulting in a fast rise of μ_{eff} at small electric field strength. The discontinuous change of μ_{eff} at an electric field around 30 kV/cm is ascribed to an avoided crossing of the $|2, 2, 0, 2\rangle$ and $|3, 2, 2, 2\rangle$ states.

The trajectories of the molecules inside the electrostatic deflector were simulated using the calculated μ_{eff} [174]. For quantum states $J = 0 \ldots 10$, 10^7 trajectories were calculated for each set of J states and used to simulate the spatial profiles using a weighting factor based on the thermal distributions of the state for a given temperature. Those temperature-weighted simulated vertical molecular-beam profiles were scaled to the area under the curve of the corresponding experimental profile to compare the deflection profiles. The simulations include the nuclear-spin-statistical weights for the water monomer and the water dimer. For *para*- and *ortho*-water a room-temperature distribution of 1 : 3 was used.

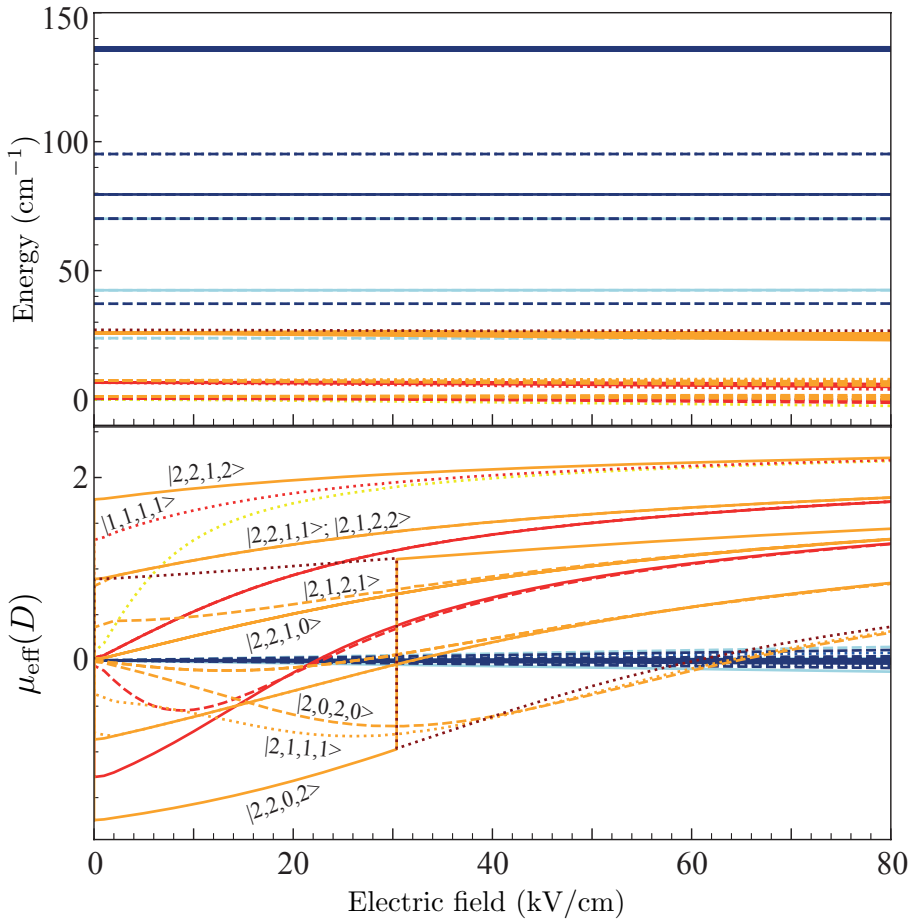

Figure A.3: Calculated Stark energy and effective dipole moments for the $J = 0 \ldots 2$ states of the water monomer (blue) and the water dimer (red, orange, yellow). $J = 0$ are shown in blue (water) and yellow (water dimer), $J = 1$ in light blue (water), red (water dimer), $J = 2$ in dark blue (water) and orange (water dimer) and the $|3, 2, 2, 2\rangle$ state in dark red for the water dimer. States where $K_a < K_c$ are indicated by dashed lines, $K_a > K_c$ by solid lines and $K_a = K_c$ by dotted lines.

The water dimer in its equilibrium geometry is isomorphic with the permutation-inversion point group D_{4h} including tunneling splittings [33]. Neglecting tunneling splittings and acceptor switching, the rigid water dimer belongs to the symmetry group $C_S(M)$, yielding nuclear-spin-statistical weights of *para*:*ortho* of 16 : 16 [91].

The simulated profiles for the water dimer at different rotational temperatures T_{rot} including rotational states $J = 0 \ldots 10$ are shown in Figure A.4. An initial-beam temperature of $T_{\mathrm{rot}} = 1.5(5)$ K reproduced the experiment the best. At this temperature the water monomer in the para nuclear spin state has 100 % of its population in its absolute rotational ground states $|J = 0, K_a = 0, K_c = 0, M = 0\rangle$, while ortho-water populates the $|J = 1, K_a = 0, K_c = 1, M = 0, 1\rangle$ state to equal amounts. 99.9 % of the para-water dimer and 99.9 % of the ortho-water dimer population is within $J = 0 \ldots 10$.

Trajectory simulations were performed for water clusters up to $n = 7$. Based on the estimated water-cluster distribution, *vide supra*, this covers 97.8 % of the water clusters in

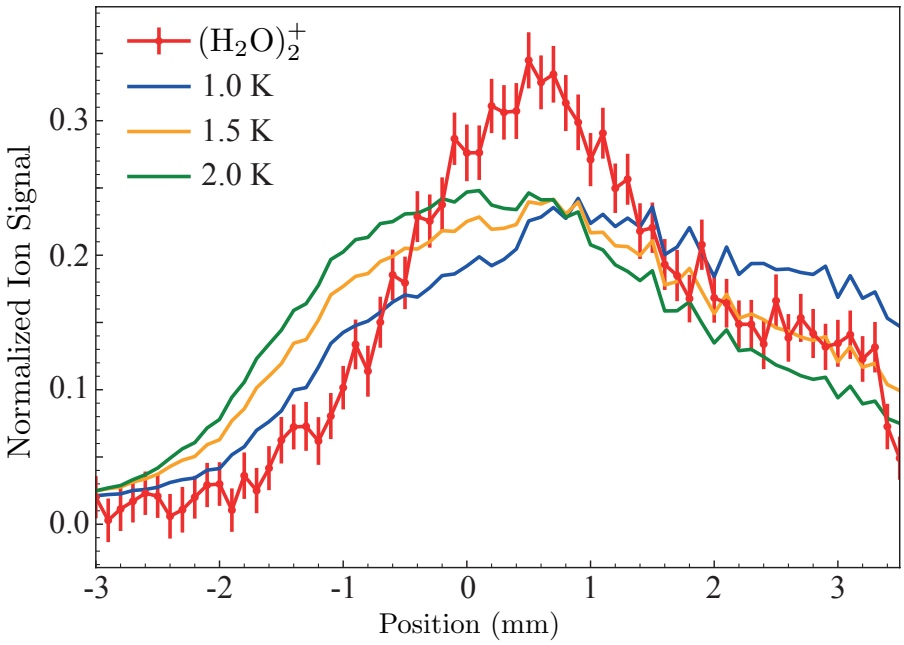

Figure A.4: Simulated deflection profiles for the water dimer at temperatures of 1.0 K, 1.5 K and 2 K compared to the corrected pure water-dimer profile at 8 kV (red, dots).

the molecular beam, while ∼2.2 % of the molecules in the beam are from water clusters $n \geq 8$. The simulations for water clusters including $J = 0 \ldots 2$ and using the same rotational temperature $T_{\text{rot}} = 1.5(5)$ K of the water dimer are shown in Figure A.5. We note that at this temperature rotational states up to $J = 10$ might be populated in the molecular beam and the rotational temperature can differ from the one of the water dimer. Thus, the simulations give just an estimate of the amount of deflection. Based on the simulations the water dimer is deflecting the most of all water clusters, followed by the water hexamer in prism- and book-like form, which reaches to a position of +3.2 mm.

Since for larger clusters only fragments have been measured and, therefore, the shape of the recorded beam profiles is the result of a superposition of several neutral cluster distributions in the molecular beam, it is not possible to compare the single deflection profiles directly with simulations. Therefore, at each position of the deflection profile the signal of the measured protonated water clusters for $n = 2 \ldots 10$ have been summed up. The H_3O^+, $n = 1$, contained also signal from the water dimer and has not been included. For the computationally derived profiles $n = 3 \ldots 7$ were summed up for each position. As for the hexamer and heptamer several conformers have been simulated, each profile of the hexamer has been divided by 3 and for the heptamer by 2. This is shown in Figure A.6. These simulations assume a rather low temperature of 1.5 K and did not include the needed nuclear spin statistical weighting for larger-clusters. In addition, the decaying water-cluster distribution in the molecular beam was not taken into account, resulting in a slightly different shape of the vertical molecular-beam-density profiles than the measured ones. However, comparing the simulated and the measured deflection

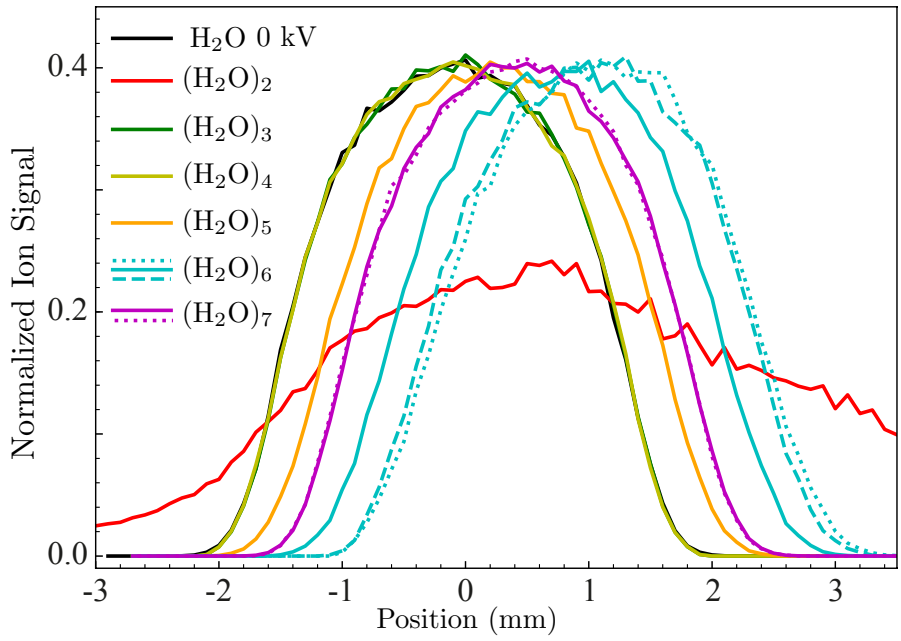

Figure A.5: Simulated deflection profiles for water clusters for $n = 2 \ldots 7$ are shown. Three different conformers of the water hexamer and two of the water heptamer were included, see text for details.

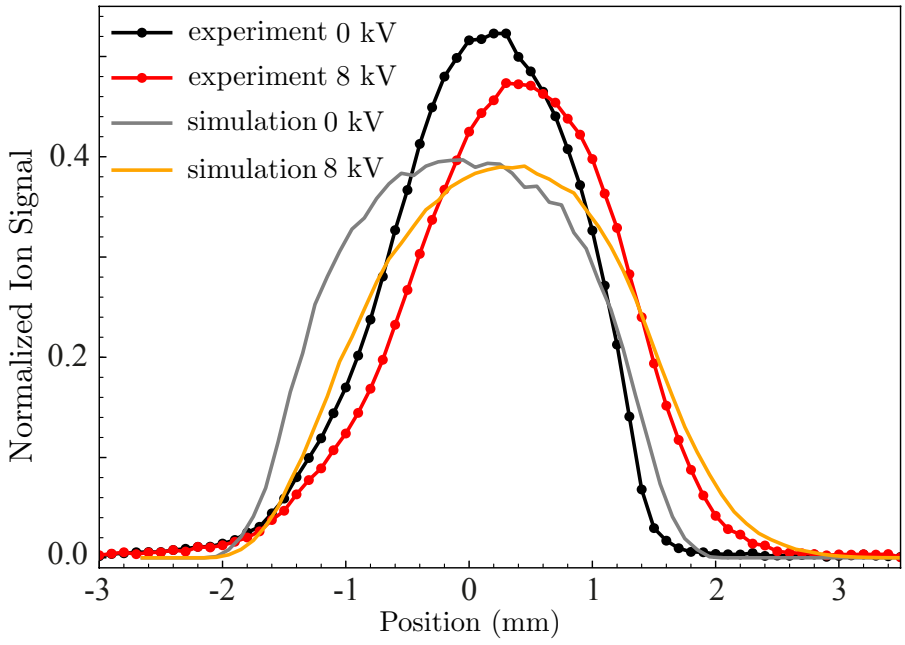

Figure A.6: Summed up simulated deflection profiles for water clusters for $n = 3 \ldots 7$ (grey, orange) and summed up measured deflection profiles for protonated water clusters for $n = 2 \ldots 10$ (black and red dots) for a deflector voltage of 0 kV (grey, black) and 8 kV (orange, red). The profiles are normalized to the area under the curve.

profiles, the deflection is on the same order of magnitude and the right-hand side tail of the simulated deflection profile is reaching up to a position of +3.2 mm.

B Supplemental Information for chapter 5

Simulation of a TOF to confirm the gate subtraction method

A simulated TOF using SIMION [144] and assuming a PW of 90 ns (blue) and 80 ns (orange) is shown in Figure 5.1. As input parameters the masses of 14 u/e to 19 u/e with velocities in the range of (0-5) mm/µs were used, which are equal to the measured velocity ranges. The two simulations were subtracted from each other (green), such that each data point of the resulting TOF contained data for 10 ns only (green). The arrival time of the simulated ions had an offset of 0.27 ± 0.01 µs compared to the experiment, caused by a not accurately placed laser focus in between the spectrometer electrodes and an unknown temporal offset between the actual arrival time of the laser in the interaction zone of the VMI spectrometer with respect to the laser trigger. For a PW of 90 ns (blue), local maxima are not well separated from each other and are shifted for a gate width of 80 ns (blue). After subtraction (green), four local maxima occur at 16 u/e, 17 u/e, 18 u/e and 19 u/e, corresponding to O^+, OH^+, H_2O^+ and H_3O^+.

In Figure 5.1 b) and c) only ions in a specific momentum range, as depicted by the black circles in Figure 5.3 in the main paper, were taken into account. For the low-momentum region, which corresponds to fragments resulting from a dissociation after single ionization, four separated local maxima occur in Figure 5.1 b) for a time window of 10 ns (green) at 16 u/e, 17 u/e, 18 u/e and 19 u/e. For the high-momentum region in Figure 5.1 c), which are ions resulting from a Coulomb explosion following double ionization, the local maxima are shifted with respect to Figure 5.1 b) and are located at 15.9 u/e, 16.9 u/e, 17.9 u/e and 18.9 u/e.

The structure of the measured TOF in Figure 5.1 in the main paper and simulated TOF in Figure 5.1 are in good agreement. The shift of the arrival times between the simulated TOF in Figure 5.1 b) and in Figure 5.1 c) can be explained by the larger velocity of ions that end up between the solid and dashed line in Figure 5.3 in the main paper, which can not be resolved in the measurement due to the overlap of the single and double ionization spheres. The separation of the fragments of O^+, OH^+, H_2O^+ and H_3O^+ after gate subtraction can be verified and their arrival times identified to be at 2.165 µs, 2.235 µs, 2.305 µs and 2.375 µs, respectively.

Ion yield

The relative ion yields of O^+, OH^+, H_2O^+ and H_3O^+ following single and double ionization were calculated by integrating the ion yields over the single and double ionization regions, depicted as solid lines in Figure 5.4. The relative ion yields are listed in Table B.1, which were normalized to one. Overall, single ionization was the favored process. The

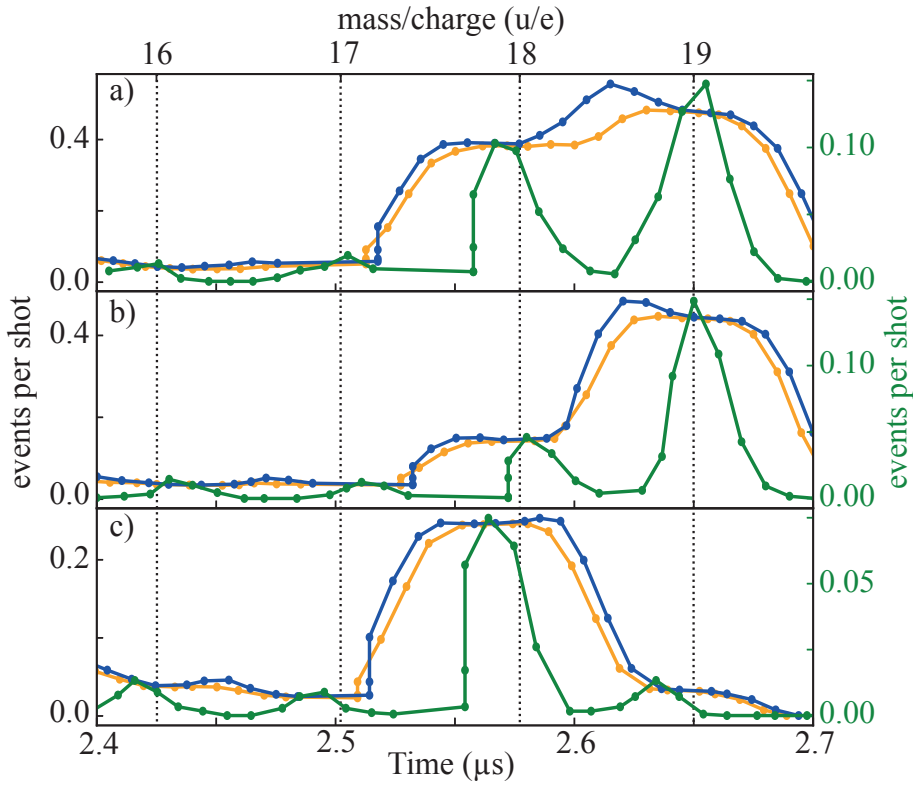

Figure B.1: a) A simulated time-of-flight of b) ions originating from single ionization and c) double ionization. Each point contains ions with an arrival time width of 80 ns (orange), 90 ns (blue) and 10 ns (green). The green curve was obtained by subtracting the TOF with the 80 ns pulse width from the TOF with the 90 ns pulse width.

major fragmentation observed is the production of H_3O^+ following single ionization of the dimer, followed by the production of H_2O^+ originating from a double-ionization break up. Ions from single ionization can be assumed to belong to independent fragmentation processes, as their partner were neutral molecules. An ion resulting from a double ionization process has another ion as a partner, such that two measured ions must belong to one double ionization process, which reduces its contribution in the actual branching ratio calculation.

Angular Distribution

The angular distribution of O^+ (orange), OH^+ (dark blue), H_2O^+ (light blue) and H_3O^+ (green) for fragments formed following a) single ionization and b) double ionization of the water dimer are shown in Figure B.2. The angular distribution for O^+, OH^+ and H_3O^+ resulting from single ionization are mainly isotropic, while O^+, OH^+ (dark blue), H_2O^+ from double ionization and H_2O^+ show an anisotropic distribution with a recoil along the laser polarization, depicted as a red arrow. For fragments resulting from a double ionization, OH^+ and H_2O^+ had the largest anisotropy, which broadens for O^+ and H_3O^+.

Fragmentation process	Relative ion yields
single ionization	0.61
$O^+ + n$	0.02
$OH^+ + n$	0.03
$H_2O^+ + n$	0.08
$H_3O^+ + n$	0.49
double ionization	0.39
$O^+ + c$	0.03
$OH^+ + c$	0.06
$H_2O^+ + c$	0.24
$H_3O^+ + c$	0.05

Table B.1: Relative ion yields of the fragments of water dimer and of the ionization process with n as a neutral molecule and c as an ion, which were normalized to 1.

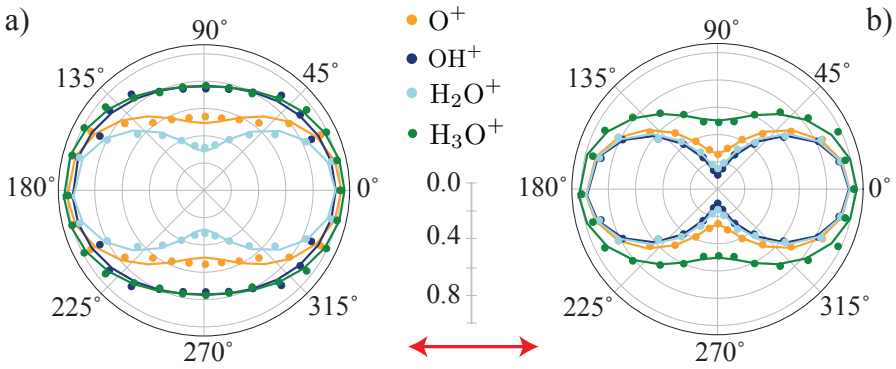

Figure B.2: Angular distributions (dots) of O^+ (orange), OH^+ (dark blue), H_2O^+ (light blue) and H_3O^+ (green) and the fitted second Legendre polynomial (lines) resulting from a) a dissociation of a single ionized water dimer and b) a Coulomb explosion of a double ionized water dimer. The red arrow represents the direction of the laser polarization.

C Creation of a Molecular Beam of Water Clusters

Clustering is a complex process, which is influenced by many parameters during the supersonic expansion, as discussed in subsection 2.3.1. As cluster expansion leads to a mixture of various cluster stoichiometries, only low concentrations for specific species can be achieved. Cold supersonic beams of water clusters [150] contain a water dimer concentration of only a few percent [67, 164]. This leads to small experimental event rates and requires long measurement times, e. g., in coincidence detection schemes [67, 160]. To increase the concentration of water dimers in the molecular beam, the vapor pressure needs to be controlled. A vapor pressure diagram of water is shown in Figure C.1. As the vapor pressure of water is decreasing with decreasing temperature, the formation of large clusters could be suppressed leading to an enhanced ratio of small water clusters, such as water dimer, trimer and tetramer, to larger water clusters. In this chapter, the influence of various parameters, such as the temperature, the pressure and the seeding gases, on the supersonic expansion process will be investigated. Moreover, the cluster distribution of a supersonic molecular beam containing different water clusters will be studied.

A similar experiment as described in Section 2.4 with a changing set of conditions and distances was used. An Even-Lavie valve [14] was used to expand water into vacuum with a nominal driving-pulse duration of (25 to 30.5) µs and at a repetition rate of 10 Hz. The Even-Lavie valve can run at room temperature and above. Therefore, a reservoir, shown in Figure C.2, containing the water sample was built and installed in front of the

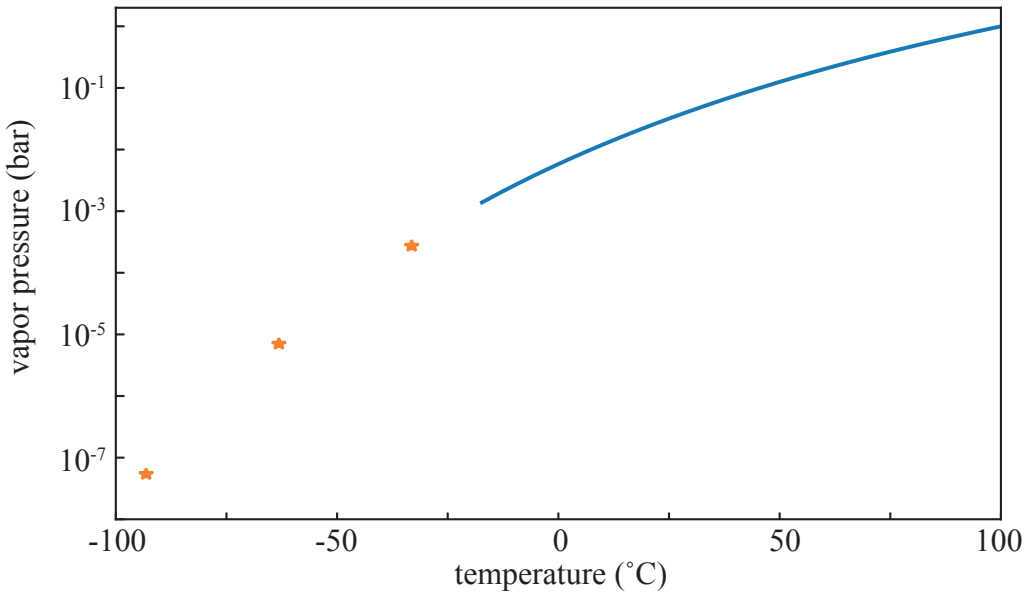

Figure C.1: Calculated vapor pressure diagram of water (blue [260, 261], orange [262]).

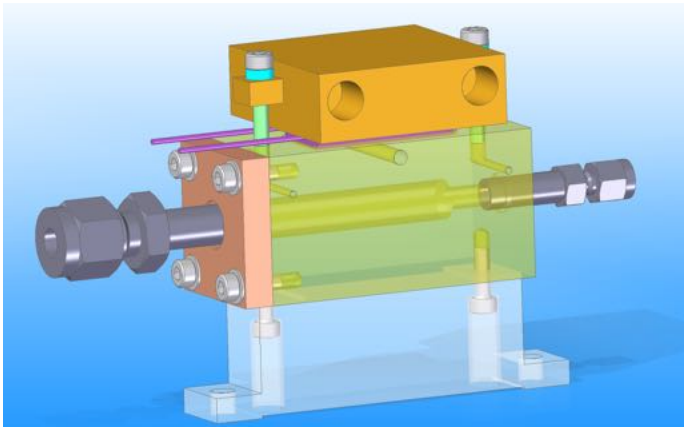

Figure C.2: A water reservoir containing the water sample was installed in front of the Even-Lavie valve.

valve with a temperature range of −20 °C to 20 °C. The molecular beam was created using helium, argon or neon as a seed gas with various stagnation pressures. The produced molecular beam was skimmed 7.4 cm (∅ = 2 mm) downstream the nozzle. In the center of a TOF spectrometer, molecules were strong-field ionized by a 35 fs short laser pulse with a central wavelength around 800 nm, focussed to 70 µm FWHM with varying peak intensities between $\sim(0.9 - 2.6) \times 10^{14}$ W/cm^2. The generated ions were accelerated toward a MCP detector combined with a phosphor screen and the generated signal was read out by the MCP through a decoupling box and a digitizer.

A TOF of the molecular beam using helium (dark blue) with a pressure of 85 bar, argon (purple) and neon (orange) with 10 bar as seed gases with a reservoir temperature of 20 °C and a laser intensity of $\sim 1.8 \times 10^{14}$ W/cm^2 is shown in Figure C.3. The TOF is normalized to the maximum of the water signal. The grey dashed lines indicate the positions of water clusters with $n = 1 \ldots 10$ monomers per water cluster. The intensity decreases with n and the contribution from protonated cluster was larger than for water clusters. Water, water dimer and protonated water clusters were measured for all seeding gases. Protonated water clusters $(H_2O)_nH^+$ were measured for helium up to $n = 10$ and neon $n = 19$, while argon most likely formed even larger protonated water clusters. Argon clusters Ar_m^+ and argon-water clusters $Ar_mH_2O_n^+$ were formed in case of argon as a seeding gas. The arrival times of these argon-water clusters were in some cases similar to the arrival time of water clusters and protonated water clusters and were hard to distinguish. Thus, only a contribution from water clusters up to $n = 8$ have been taken into account in the following analysis.

To investigate the contribution of water dimers, the maxima in the TOF of water clusters and protonated water clusters were integrated, the water dimer-to-water clusters ratio and the water dimer-to-protonated water cluster ratio with clusters up to $n = 8$ were calculated and compared under different temperatures, laser intensities, seeding gases and pressures, as shown in Figure C.4. With a laser intensity of 1.8×10^{14} W/cm^2, a

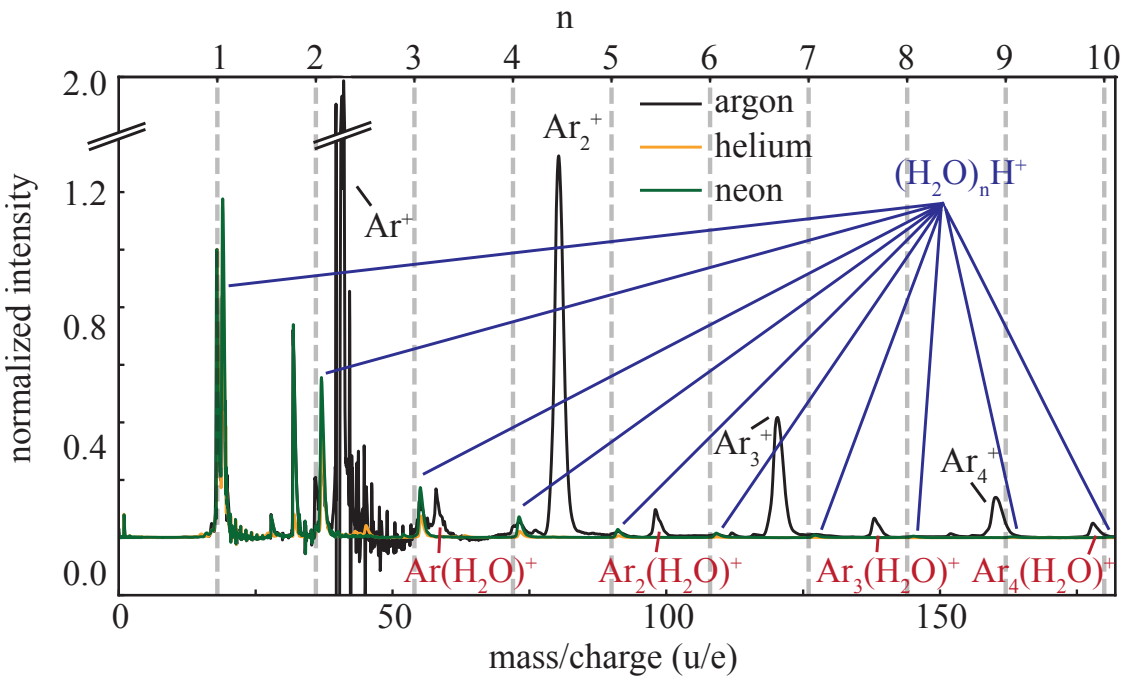

Figure C.3: A TOF of a molecular beam containing water clusters and protonated water cluster using helium (dark blue), argon (purple) and neon (orange) as a seeding gas.

maximal water dimer concentration of 13.4 % was achieved using a reservoir temperature of 20 °C. Using argon at 5 bar instead, a maximal water dimer concentration of 9.6 % could be achieved with a reservoir temperature of −10 °C. With helium, we achieved a maximal contribution of 2.9 % at 85 bar, a temperature of −20 °C and a laser intensity of 1.3×10^{14} W/cm^2. With neon a maximal dimer contribution of 2.5 % could be achieved with a pressure of 10 bar and 20 °C and a laser intensity of 1.8×10^{14} W/cm^2. For argon with 5 bar, a reservoir temperature of −10 °C were favorite leading to a water dimer contribution of 9.8 % at a laser intensity of 1.8×10^{14} W/cm^2. Using helium with 60 bar, a maximal water dimer concentration of 2.6 % was achieved using a laser intensity of 1.3×10^{14} W/cm^2. For neon at 5 bar, 2.2 % water dimer was found in the molecular beam at 0 °C and a laser intensity of 1.8×10^{14} W/cm^2.

Overall, the largest water dimer contribution could be achieved using argon with 10 bar and a temperature of −20 °C for all used laser intensities, followed by argon at 5 bar at temperatures of −10 °C and 10 °C. Helium and neon lead to the same order of magnitude of the water dimer concentration. For helium, a pressure of 85 bar was favorite for the water dimer formation, but for both pressures a temperature of −20 °C lead to the largest water dimer contribution for all laser intensities. For neon at 10 bar, an increasing water dimer ratio was measured toward larger temperatures. While for a pressure of 5 bar, a temperature of 0 °C was favorite for the water dimer-to-cluster ratio.

Conclusively, the change of the seeding gas gave the largest change of the cluster distribution, followed by the stagnation pressures. The changes of the water-cluster ratio

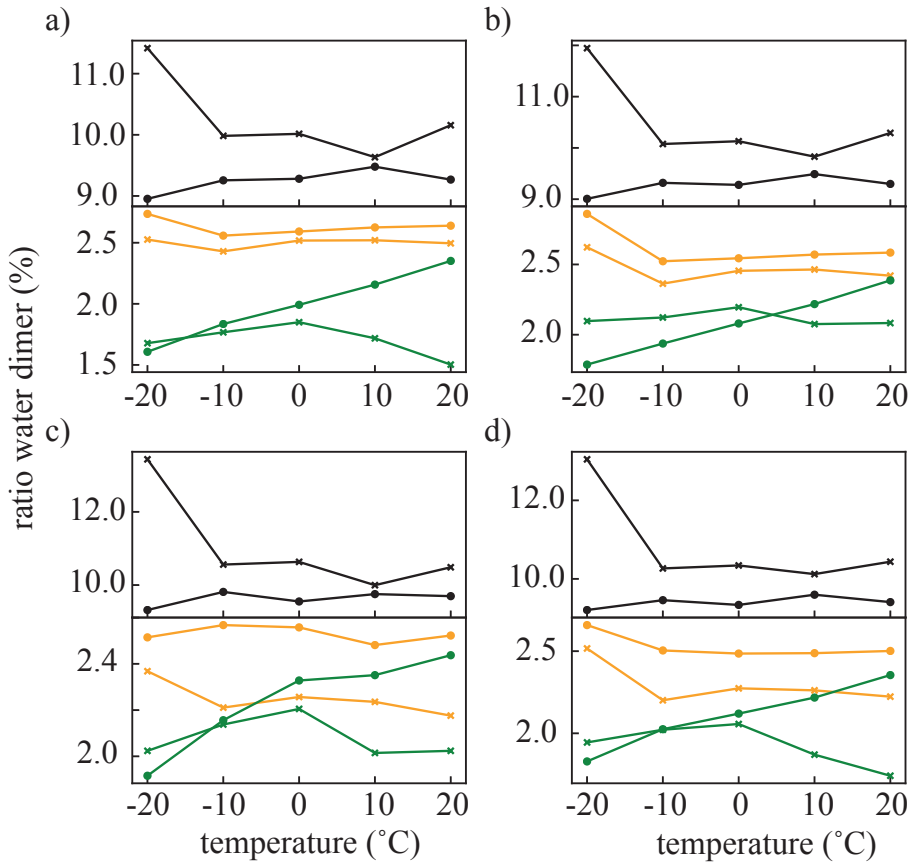

Figure C.4: The ratio of water dimer to water cluster and protonated water cluster up to $n = 8$ for argon (black) at 5 bar (circle), 10 bar (cross), helium (orange) at 60 bar (circle) and 85 bar (cross) and neon (green) at 5 bar (circle), 10 bar (cross) for different laser intensities a) 0.9×10^{14} W/cm^2 b) 1.3×10^{14} W/cm^2 c) 1.8×10^{14} W/cm^2 d) 2.6×10^{14} W/cm^2 .

with varying temperatures in the range of -20 °C and 20 °C were small. The temperature, where the water dimer formation is supported and the larger cluster formation suppressed, depend from the seeding gas species and the used stagnation pressures. The diagram in Figure C.1 revealed that the temperature changes from 20 °C to -20 °C lead to a vapor pressure decrease of only one order of magnitude, such that a larger temperature difference could be investigated to measure a larger change of the water dimer-to-cluster ratio in the molecular beam.

D Dissociation Processes from Water Clusters

In chapter 3, we observed mainly protonated clusters, water and water-dimer ions using SFI and a TOF spectrometer. Also literature reported mainly about the observation of protonated water clusters after ionization of a molecular beam. It has been shown that most often only water and water dimer ions could be found in the mass spectra [63–65]. Further studies have shown that using argon as a seed gas lead to argon-water clusters $Ar_mH_2O_n^+$ that fragmented into unprotonated water clusters $(H_2O)_n^+$ with $n > 2$ as well [93]. In [263], the fragmentation into unprotonated clusters has been explained by an evaporative cooling of argon atoms following photoionization, which removed the internal energy of water clusters and suppressed the fragmentation reaction of water clusters using VUV light. In this chapter, dissociation processes of water clusters following SFI will be investigated using a VMI spectrometer and a molecular beam containing several sized water clusters.

A similar experiment as described in Section 2.4 with a changing set of conditions and distances was used. Briefly, liquid water was placed in the reservoir of an Even-Lavie valve [14] at 20 °C, seeded in 10 bar of argon, and expanded into vacuum with a nominal driving-pulse duration of 24.5 µs and at a repetition rate of 10 Hz. The produced molecular beam was triple-fold skimmed, 7.4 cm ($\varnothing = 2$ mm), 15.7 cm ($\varnothing = 1$ mm) and 25.9 cm ($\varnothing = 1.5$ mm) downstream the nozzle. In the center of a VMI spectrometer consisting of two plates [264, 265], molecules were strong-field ionized by a 35 fs short laser pulse with a central wavelength around 800 nm and a pulse energy of 130 µJ. Focusing to 70 µm FWHM yielded a peak intensity of $\sim 1 \times 10^{14}$ W/cm^2. The generated ions were accelerated and velocity mapped toward a MCP detector combined with a phosphor screen and the generated 2D signal was recorded with a camera.

A TOF of the molecular beam with $n = 1 \ldots 10$ monomers per water cluster is shown in Figure D.1. The TOF is normalized to the maximum of the argon signal Ar^+. The argon signal caused a ringing signal of the detector. Maxima of protonated water clusters are clearly visible (dark blue), while the water clusters signals were too low to resolve in this TOF. Also argon Ar_m^+ (black) and argon-water clusters $Ar_mH_2O_n^+$ (red) were formed during the supersonic expansion.

However, using a VMI spectrometer the contribution from water clusters could be resolved as well. These VMIs were converted into momentum and are shown on the right half and their inversion using the Maximum Entropy Velocity Legendre Reconstruction (MEVELER) method from Bernhard Dick [196] on the left half in Figure D.2 and Figure D.3, Figure D.4 for water clusters $(H_2O)_n^+$ with $n = 1 \ldots 6, 8 \ldots 10$, for protonated water clusters $(H_2O)_nH^+$ with $n = 1 \ldots 10$ and for fragments O^+ and OH^+, respectively.

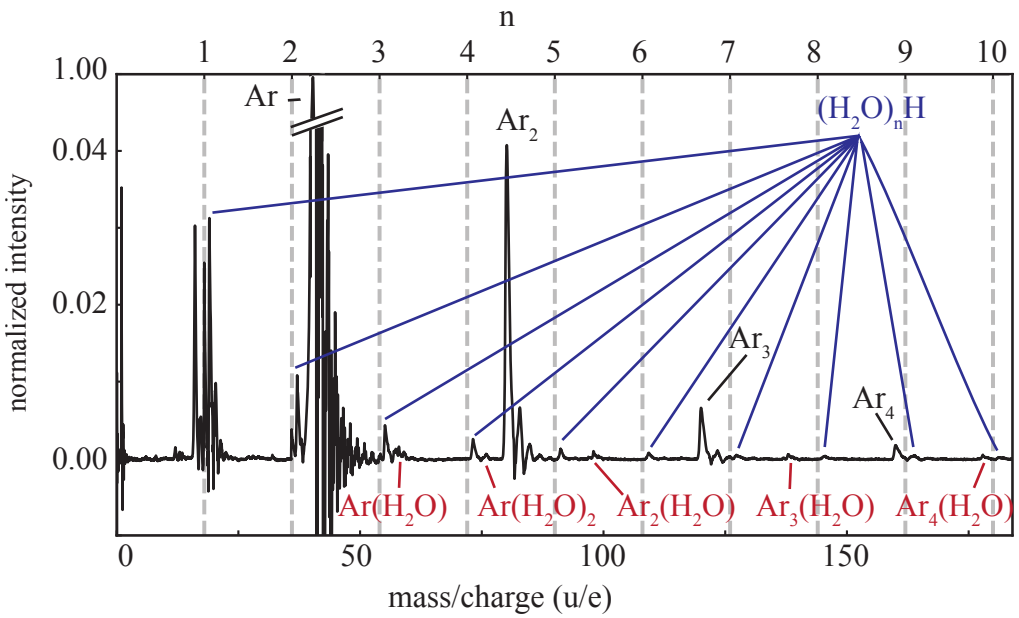

Figure D.1: TOF-MS of the molecular beam of unprotonated $(H_2O)_n^+$ and protonated water clusters $(H_2O)_nH^+$ for $n = 1 \ldots 10$. The TOF is normalized to the maximum of the argon signal and zoomed in.

For all water clusters, the maximum intensities were measured in the center of the MMI with low momenta. After inversion, several rings appeared in the MMI of $(H_2O)_n^+$ for $n = 2 \ldots 6, 8 \ldots 10$. The MMIs of protonated water clusters show a mainly smooth distribution over the detector with a slight maximum in the center region. After inversion, several rings appeared. Also the MMIs of O^+ and OH^+ show a smooth momentum distribution over the whole images. After inversion, a lower intensity in the center region and a ring structure became visible.

Radial distributions converted to energy of the measured water clusters $(H_2O)_n^+$ with $n = 1 \ldots 10$ are shown in Figure D.5 a), for protonated water clusters $(H_2O)_nH^+$ in Figure D.5 b) and for O^+ and OH^+ in Figure D.5 c). The radial distributions of water clusters $(H_2O)_n^+$ with $n = 1 \ldots 6, 8 \ldots 10$ had a maximum or a local maximum at 0.006 eV. For clusters with $n = 3 \ldots 6, 8 \ldots 10$ another local maximum were found at around 0.2 eV. For $(H_2O)_3^+$ additional maxima occurred at 0.03 eV and 0.07 eV. Another local maximum at 0.07 eV was found for $(H_2O)_4^+$. The radial distributions of H_2O^+ and $(H_2O)_2^+$ were smoothly decreasing toward larger energies.

For protonated water clusters $(H_2O)_nH^+$ with $n = 1, 2, 4, 7$, a maximal intensity close at an energy of 0.006 eV was measured. For protonated clusters with $n = 3, 5, 6, 8, 9, 10$, a maximal intensity at an energy of 0.03 eV were found. Additional local maxima were arsing at an energy of $\sim$0.2 eV for protonated water clusters with $n = 4 \ldots 10$. A decrease of intensity toward larger energies is shown with $n = 1 \ldots 3$ monomers per protonated cluster.

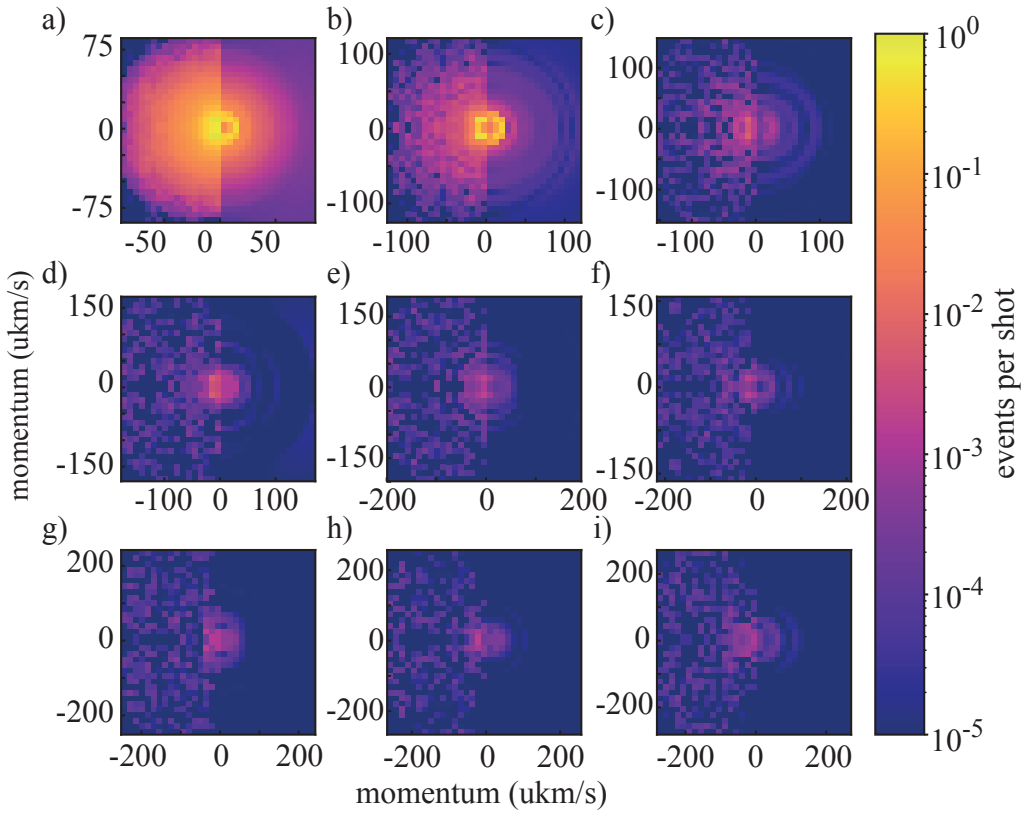

Figure D.2: Momentum map (left side) and MEVELER inverted (right side) images of a) H_2O^+, b) $(H_2O)_2^+$, c) $(H_2O)_3^+$, d) $(H_2O)_4^+$, e) $(H_2O)_5^+$, f) $(H_2O)_6^+$, g) $(H_2O)_8^+$, h) $(H_2O)_9$ and i) $(H_2O)_{10}^+$.

A plateau between 0.08 eV and 0.18 eV was found for O^+, while the radial distribution of OH^+ had a maximal intensity at an energy of 0.03 eV and local maxima at an energy of 0.006 eV and 0.22 eV.

Overall, after inversion many rings are shown in the MMIs in Figure D.2, Figure D.3 and Figure D.4 for water clusters, protonated water clusters and smaller fragments, respectively. The radial distributions of H_2O^+, $(H_2O)_2^+$, H_3O^+, $(H_2O)_2H^+$ and $(H_2O)_3H^+$ in Figure D.5 show long tails toward larger energies. Water clusters with different numbers n might undergo fragmentation processes following SFI that have at least one fragment with the same mass-to-charge ratio m/q involved. These fragments have different energies and momenta based on their fragmentation partners and the number of charges involved. All these fragments would be detected as an ion with the same mass, but with a different momenta and a different origin. An overlap of different ionization spheres would then be measured, which lead to a structure of many rings on the detector after inversion. An identification of the original parent ion is complicated and not reliable using a molecular beam containing several-sized water clusters. Instead, looking at the momenta and energies of the measured ions can help to disentangle the fragmentation process they originate from.

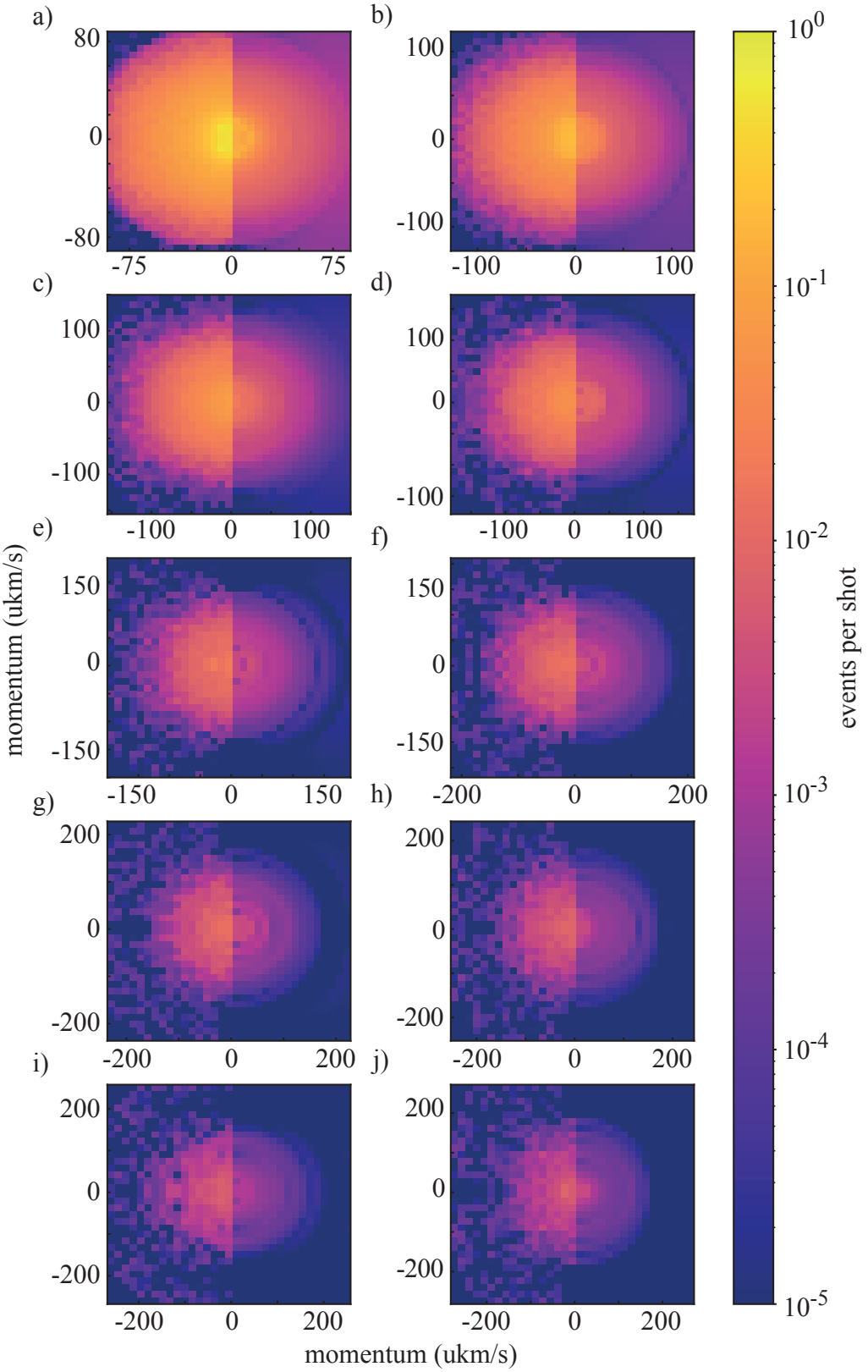

Figure D.3: Momentum map (left side) and MEVELER inverted (right side) images of protonated water clusters a) H_3O^+, b) $(H_2O)_2H^+$, c) $(H_2O)_3H^+$, d) $(H_2O)_4H^+$, e) $(H_2O)_5H^+$, f) $(H_2O)_6H^+$, g) $(H_2O)_7H^+$, h) $(H_2O)_8H^+$, i) $(H_2O)_9H^+$ and j) $(H_2O)_{10}H^+$.

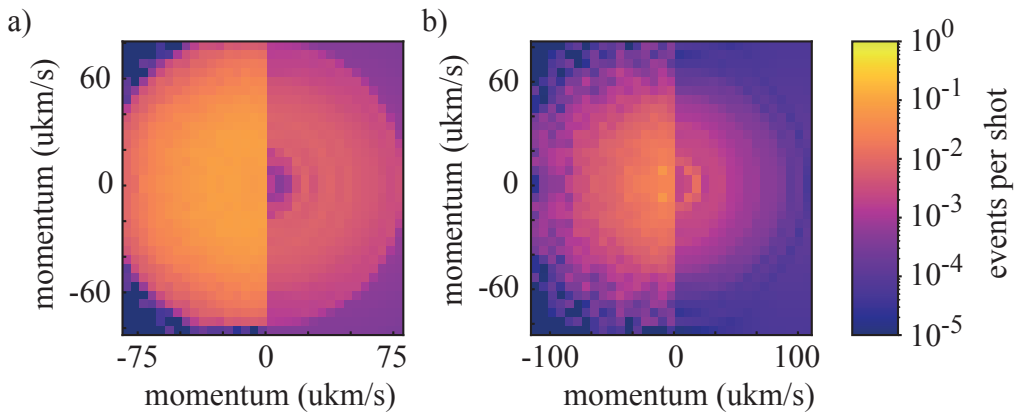

Figure D.4: Momentum map (left side) and MEVELER inverted (right side) images of a) O^+ and b) OH^+.

In analogy to chapter 5, the origin of ions in the radial distributions can be separated into parent ions (black line), neutral dissociation (black to dashed line) and Coulomb explosion (from dashed line) based on the minima and maxima of the radial distributions, as depicted by the black lines in Figure D.5. Ions with low energies between 0 eV and 0.01 eV were parent ions, while ions with energies between 0.01 to ∼0.15 eV can be described by a neutral dissociation process. Ions with energies above 0.15 eV came from a high-order ionization process. The two maxima in Figure D.5 b) might be a hint that only single and double ionization processes were measured and no higher order processes.

The ratios

$$r = \frac{N_{x,p}}{N_{x,\text{parent}} + N_{x,\text{neutral}} + N_{x,\text{Coulomb}}} \tag{D.1}$$

of the measured ion x and the process p after ionization (parent), neutral dissociation (neutral) or Coulomb explosion (Coulomb) are listed in Table D.1. Assuming protonated water clusters to be created in a molecular beam, they would be charged already before they reach the laser interaction point. Due to the spectrometer settings, those ions would not be able to reach the laser interaction point. This means that protonated water clusters can not be parent ions and must originate from a fragmentation process of an ionized water cluster. Thus, the contribution of protonated ions in the region of 0 eV and 0.01 eV were assumed to belong to a neutral dissociation process. But it has to be noted, that the maximal intensity of protonated water clusters at an energy of around 0.006 eV, might arise due to an overlap of the ionization spheres with a neighboring water cluster, which will be ignored in the following analysis. O^+ and OH^+ were also assumed to be fragments without a contribution from a parent ion.

All protonated water clusters, O^+ and OH^+ mainly originated from a neutral dissociation process following single ionization of a water cluster. H_2O^+ and $(H_2O)_2^+$ were predominantly products from a direct ionization of H_2O and $(H_2O)_2$, respectively, and second most often arising as a product from a neutral dissociation. The water trimer $(H_2O)_3^+$ originated mainly from a neutral dissociation process, followed by a direct ionization

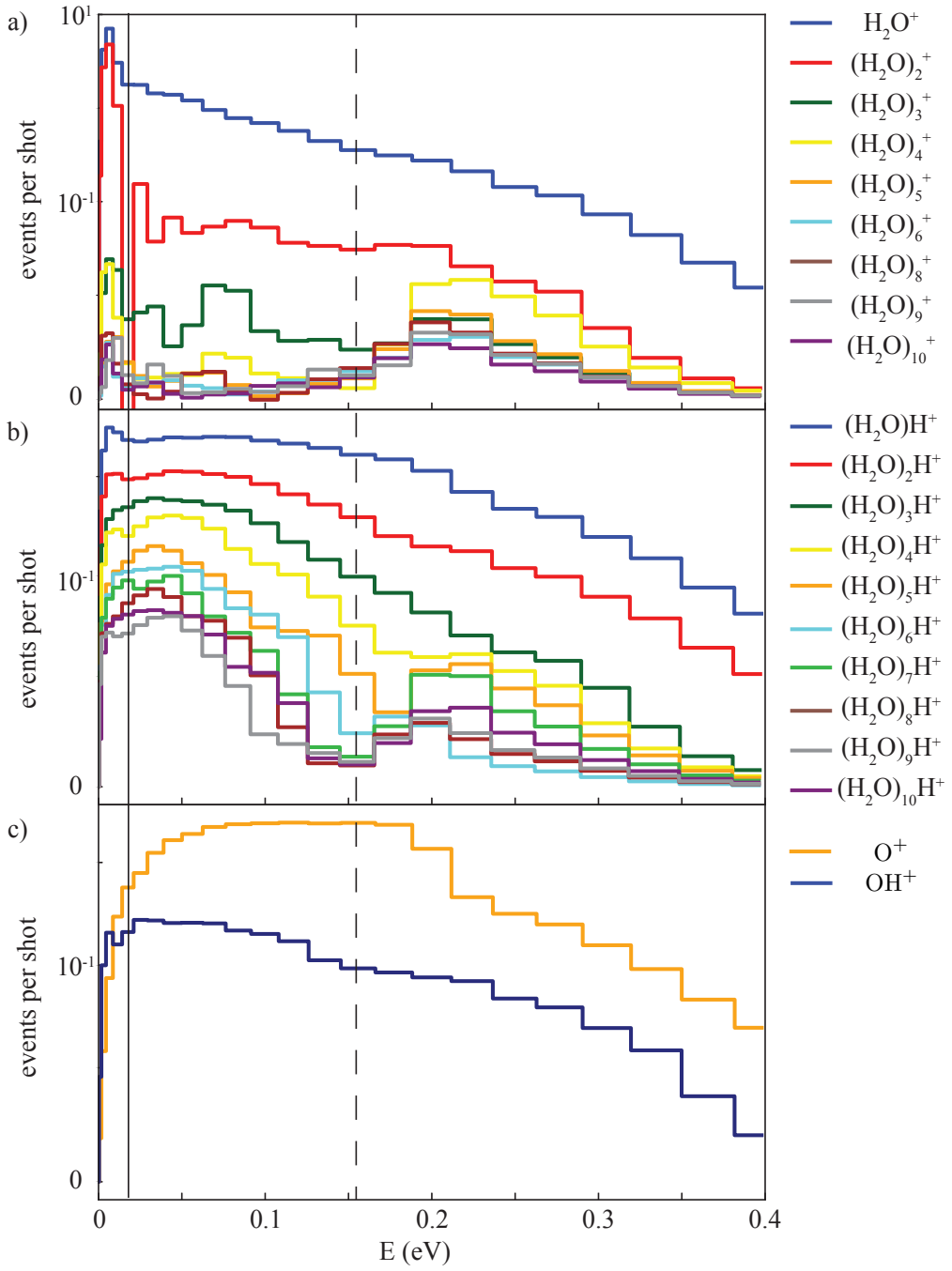

Figure D.5: Radial distribution from VMIs of a) water clusters $(H_2O)_n^+$ and b) protonated water clusters $(H_2O)_nH^+$ for $n = 1 \ldots 10$ and c) of fragments O^+ and OH^+.

Ion	parent ion	neutral dissociation	Coulomb explosion
O^+	-	0.6398	0.2413
OH^+	-	0.6559	0.1297
H_2O^+	0.4998	0.3586	0.0498
$(H_2O)_2^+$	0.9104	0.0517	0.0148
$(H_2O)_3^+$	0.2728	0.4161	0.2153
$(H_2O)_4^+$	0.3487	0.1709	0.44196
$(H_2O)_5^+$	0.1829	0.2066	0.5281
$(H_2O)_6^+$	0.1911	0.2263	0.5237
$(H_2O)_8^+$	0.2607	0.1452	0.5234
$(H_2O)_9^+$	0.2458	0.1760	0.5197
$(H_2O)_{10}^+$	0.1487	0.2369	0.5032
H_3O^+	-	0.7409	0.1461
$(H_2O)_2H^+$	-	0.8092	0.085
$(H_2O)_3H^+$	-	0.8596	0.0396
$(H_2O)_4H^+$	-	0.8817	0.0283
$(H_2O)_5H^+$	-	8549	0.04409
$(H_2O)_6H^+$	-	0.8671	0.022
$(H_2O)_7H^+$	-	0.8184	0.0616
$(H_2O)_8H^+$	-	0.8567	0.0475
$(H_2O)_9H^+$	-	0.8151	0.0816
$(H_2O)_{10}H^+$	-	0.8305	0.0823

Table D.1: Ratios of the measured protonated water clusters and water clusters. Single and double ionization processes are weighted independently from each other.

$(H_2O)_3$ and only a small contribution were formed after a Coulomb explosion. All other water clusters $n = 4 \ldots 6, 8 \ldots 10$ were mainly formed by a Coulomb explosion. While the water tetramer $n = 4$, octamer $n = 8$ and nonamer $n = 9$ were considered to have their origin from a parent ion, the water pentamer $n = 5$ and water hexamer $n = 6$ were mainly formed after a neutral dissociation.

It has been shown, that the VMI technique can be used to identify the number of charges that were involved in the fragmentation processes leading to water cluster cations and protonated water clusters. It has been shown, that water clusters were partially parent ions but also fragments from larger clusters, while protonated water clusters were fragments. The separation of a parent ion and a neutral dissociation process could be improved by using a laser polarization axis parallel to the detector plane and by decreasing the overlap of ionization spheres, for e. g. using the slicing method as described in chapter 5. As shown in chapter 3, the separation of water clusters using an electrostatic deflector might be challenging as the deflection behavior in an electric field might be similar, but still a purer molecular beam of a specific water cluster in combination with a time- and position sensitive detector could help to disentangle the fragmentation partners of the identified fragments.

Bibliography

[1] A. Szent-Györgyi, "Biology and pathology of water", Perspectives in Biology and Medicine **14**, 239 (1971).

[2] P. Ball, "Water is an active matrix of life for cell and molecular biology", PNAS **114**, 13327 (2017).

[3] P. Ball, "Water, water, everywhere?", Nature **427**, 19 (2004).

[4] P. Ball, "Seeking the solution", Nature **436**, 1084 (2005).

[5] P. Ball, "Water — an enduring mystery", Nature **452**, 291 (2008).

[6] R. Lynden-Bell, S. Morris, J. Barrow, J. Finney, and C. Harper, eds., *Water and Life* (CRC Press, Boca Raton, 2010).

[7] A. Mukhopadhyay, W. T. Cole, and R. J. Saykally, "The water dimer I: Experimental characterization", Chem. Phys. Lett. **633**, 13 (2015).

[8] A. Mukhopadhyay, S. S. Xantheas, and R. J. Saykally, "The water dimer II: Theoretical investigations", Chem. Phys. Lett. **700**, 163 (2018).

[9] M. K. Shukla and J. Leszczynski, "Radiation induced molecular phenomena in nucleic acids: A brief introduction", in *Radiation Induced Molecular Phenomena in Nucleic Acids: A Comprehensive Theoretical and Experimental Analysis* (Springer Netherlands, Dordrecht, 2008) pp. 1–14.

[10] O. Collet, "How does the first water shell fold proteins so fast?", J. Chem. Phys. **134**, 085107 (2011).

[11] A. K. Samanta, Y. Wang, J. S. Mancini, J. M. Bowman, and H. Reisler, "Energetics and Predissociation Dynamics of Small Water, HCl, and Mixed HCl-Water Clusters.", Chem. Rev. **116**, 4913 (2016).

[12] W. Demtröder, *Laser Spectroscopy 2: Experimental Techniques* (Springer Verlag, Berlin, 2008).

[13] G. Scoles, ed., *Atomic and molecular beam methods*, Vol. 1 (Oxford University Press, New York, NY, USA, 1988).

[14] U. Even, J. Jortner, D. Noy, N. Lavie, and N. Cossart-Magos, "Cooling of large molecules below 1 K and He clusters formation", J. Chem. Phys. **112**, 8068 (2000).

[15] O. F. Hagena and W. Obert, "Cluster formation in expanding supersonic jets: Effect of pressure, temperature, nozzle size, and test gas", J. Chem. Phys. **56**, 1793 (1972).

[16] Y.-P. Chang, D. A. Horke, S. Trippel, and J. Küpper, "Spatially-controlled complex molecules and their applications", Int. Rev. Phys. Chem. **34**, 557 (2015).

[17] W. Gerlach and O. Stern, "Der experimentelle Nachweis der Richtungsquantelung im Magnetfeld", Z. Phys. **9**, 349 (1922).

[18] B. Friedrich and D. Herschbach, "Stern and Gerlach: How a bad cigar helped reorient atomic physics", Phys. Today **56**, 53 (2003).

[19] M. Johny, J. Onvlee, T. Kierspel, H. Bieker, S. Trippel, and J. Küpper, "Spatial separation of pyrrole and pyrrole-water clusters", Chem. Phys. Lett. **721**, 149–152 (2019).

[20] T. Kierspel, D. A. Horke, Y.-P. Chang, and J. Küpper, "Spatially separated polar samples of the *cis* and *trans* conformers of 3-fluorophenol", Chem. Phys. Lett. **591**, 130 (2014).

[21] N. Teschmit, D. A. Horke, and J. Küpper, "Spatially separating the conformers of a dipeptide", Angew. Chem. Int. Ed. **57**, 13775 (2018).

[22] D. A. Horke, Y.-P. Chang, K. Długołęcki, and J. Küpper, "Separating para and ortho water", Angew. Chem. Int. Ed. **53**, 11965 (2014).

[23] S. Trippel, Y.-P. Chang, S. Stern, T. Mullins, L. Holmegaard, and J. Küpper, "Spatial separation of state- and size-selected neutral clusters", Phys. Rev. A **86**, 033202 (2012).

[24] D. J. Nesbitt and M. A. Suhm, "Chemical dynamics of large amplitude motion", Phys. Chem. Chem. Phys. **12**, 8151 (2010).

[25] M. Fárník, S. Davis, and D. J. Nesbitt, "High-resolution IR studies of hydrogen bonded clusters: Large amplitude dynamics in $(HCl)_n$", Faraday Disc. **118**, 63 (2001).

[26] G. Berden, W. L. Meerts, M. Schmitt, and K. Kleinermanns, "High resolution UV spectroscopy of phenol and the hydrogen bonded phenol-water cluster", J. Chem. Phys. **104**, 972 (1996).

[27] M. Gerhards, M. Schmitt, and K. Kleinermanns, "The structure of phenol(H_2O) obtained by microwave spectroscopy", J. Chem. Phys. **104**, 967 (1996).

[28] S. Blanco, J. Lopez, J. Alonso, P. Ottaviani, and W. Caminati, "Pure rotational spectrum and model calculations of indole-water", J. Chem. Phys. **119**, 880 (2003).

[29] F. Dahms, B. P. Fingerhut, E. T. J. Nibbering, E. Pines, and T. Elsaesser, "Large-amplitude transfer motion of hydrated excess protons mapped by ultrafast 2D IR spectroscopy", Science **357**, 491 (2017).

[30] V. E. Ingamells, M. G. Papadopoulos, N. C. Handy, and A. Willetts, "The electronic, vibrational and rotational contributions to the dipole moment, polarizability, and first and second hyperpolarizabilities of the bh molecule", J. Chem. Phys. **109**, 1845 (1998).

[31] L. B. Braly, K. Liu, M. G. Brown, F. N. Keutsch, R. S. Fellers, and R. J. Saykally, "Terahertz laser spectroscopy of the water dimer intermolecular vibrations. II. $(H_2O)_2$", J. Chem. Phys. **112**, 10314 (2000).

[32] R. S. Fellers, L. B. Braly, R. J. Saykally, and C. Leforestier, "Fully coupled six-dimensional calculations of the water dimer vibration-rotation-tunneling states with split Wigner pseudospectral approach. II. Improvements and tests of additional potentials", J. Chem. Phys. **110**, 6306 (1999).

[33] T. R. Dyke, "Group theoretical classification of the tunneling–rotational energy levels of water dimer", J. Chem. Phys. **66**, 492 (1977).

[34] M. Born and R. Oppenheimer, "Zur Quantentheorie der Molekeln", Ann. Physik **84**, 457 (1927).

[35] P. Hamm and G. Stock, "Vibrational conical intersections in the water dimer", Mol. Phys. **111**, 2046 (2013).

[36] T. N. Clasp and D. S. Perry, "Torsion-vibration coupling in methanol: The adiabatic approximation and intramolecular vibrational redistribution scaling", J. Chem. Phys. **125**, 104313 (2006).

[37] D. S. Perry, "The adiabatic approximation as a diagnostic tool for torsion–vibration dynamics", J. Mol. Spectrosc. **257**, 1 (2009).

[38] J. M. Bowman, "A test of an adiabatic treatment of rotation for vibration/rotation energies of polyatomic molecules", Chemical Physics Letters **217**, 36 (1994).

[39] S. C. Farantos and J. Tennyson, "On the vibrational Born–Oppenheimer separation scheme for molecules with regular and chaotic states", J. Chem. Phys. **84**, 6210 (1986).

[40] B. R. Johnson and W. P. Reinhardt, "Adiabatic separations of stretching and bending vibrations: Application to H_2O", J. Chem. Phys. **85**, 4538 (1986).

[41] D. Lauvergnat, A. Nauts, Y. Justum, and X. Chapuisat, "A harmonic adiabatic approximation to calculate highly excited vibrational levels of "floppy molecules"", J. Chem. Phys. **114**, 6592 (2001).

[42] B. Kuhn, T. R. Rizzo, D. Luckhaus, M. Quack, and M. A. Suhm, "A new six-dimensional analytical potential up to chemically significant energies for the electronic ground state of hydrogen peroxide", J. Chem. Phys. **111**, 2565 (1999).

[43] B. Fehrensen, D. Luckhaus, M. Quack, M. Willeke, and T. R. Rizzo, "Ab initio calculations of mode selective tunneling dynamics in $^{12}CH_3OH$ and $^{13}CH_3OH$", J. Chem. Phys. **119**, 5534 (2003).

[44] O. Svoboda, D. Hollas, M. Ončák, and P. Slavíček, "Reaction selectivity in an ionized water dimer: Nonadiabatic ab initio dynamics simulations", Phys. Chem. Chem. Phys. **15**, 11531 (2013).

[45] L. Valenzano, M. C. van Hemert, and G.-J. Kroes, "Photodissociation of the water dimer: Three-dimensional quantum dynamics studies on diabatic potential-energy surfaces", J. Chem. Phys. **123**, 034303 (2005).

[46] G. Avila, G. J. Kroes, and M. C. van Hemert, "The photodissociation of the water dimer in the Ã band: A twelve-dimensional quasiclassical study", J. Chem. Phys. **128**, 144313 (2008).

[47] B. Chmura, Z. Lan, M. F. Rode, and A. L. Sobolewski, "Photochemistry of the water dimer: Time-dependent quantum wave-packet description of the dynamics at the S1-S0 conical intersection", J. Chem. Phys. **131**, 134307 (2009).

[48] C. J. Burnham and S. S. Xantheas, "Development of transferable interaction models for water. I. Prominent features of the water dimer potential energy surface", J. Chem. Phys. **116**, 1479 (2002).

[49] Q. C. Nguyen, Y. S. Ong, H. Soh, and J.-L. Kuo, "Multiscale approach to explore the potential energy surface of water clusters (H2O)nn $\leq$8", J. Phys. Chem. A **112**, 6257 (2008), pMID: 18572899.

[50] P. A. Pieniazek, J. VandeVondele, P. Jungwirth, A. I. Krylov, and S. E. Bradforth, "Electronic structure of the water dimer cation", The Journal of Physical Chemistry A **112**, 6159 (2008), pMID: 18563882.

[51] H. Yachikawa, "Ionization dynamics of small-sized water clusters: A direct ab initio trajectory study", J. Phys. Chem. A **108**, 7853 (2004).

[52] F. N. Keutsch and R. J. Saykally, "Inaugural article: Water clusters: Untangling the mysteries of the liquid, one molecule at a time", PNAS **98**, 10533 (2001).

[53] W. . Demtröder, *Atoms, Molecules and Photons An Introduction to Atomic-, Molecular- and Quantum Physics*, third edition ed., Graduate Texts in Physics: SpringerLink: Bücher (Springer, 2018).

[54] N. Delbos, C. Werle, I. Dornmair, T. Eichner, L. Hübner, S. Jalas, S. Jolly, M. Kirchen, V. Leroux, P. Messner, M. Schnepp, M. Trunk, P. Walker, P. Winkler, and A. Maier, "Lux – a laser–plasma driven undulator beamline", Nucl. Instrum. Meth. A **909**, 318 (2018), 3rd European Advanced Accelerator Concepts workshop (EAAC2017).

[55] K. Yamanouchi, "The next frontier", Science **295**, 1659 (2002).

[56] T. R. Dyke and J. S. Muenter, "Microwave spectrum and structure of hydrogen bonded water dimer", J. Chem. Phys. **60**, 2929 (1974).

[57] T. R. Dyke, K. M. Mack, and J. S. Muenter, "The structure of water dimer from molecular beam electric resonance spectroscopy", J. Chem. Phys. **66**, 498 (1977).

[58] J. A. Odutola and T. R. Dyke, "Partially deuterated water dimers: Microwave spectra and structure", J. Chem. Phys. **72**, 5062 (1980).

[59] B. E. Rocher-Casterline, L. C. Ch'ng, A. K. Mollner, and H. Reisler, "Communication: Determination of the bond dissociation energy (D_0) of the water dimer, $(H_2O)_2$, by velocity map imaging", The Journal of Chemical Physics **134**, 211101 (2011).

[60] W. T. S. Cole, R. S. Fellers, M. R. Viant, C. Leforestier, and R. J. Saykally, "Far-infrared VRT spectroscopy of the water dimer: Characterization of the 20 μm out-of-plane librational vibration", J. Chem. Phys. **143**, 154306 (2015).

[61] J. Hargrove, "Water dimer absorption of visible light", Atmospheric Chemistry and Physics Discussions **7**, 11123 (2007).

[62] V. Vaida, J. S. Daniel, H. G. Kjaergaard, L. M. Goss, and A. F. Tuck, "Atmospheric absorption of near infrared and visible solar radiation by the hydrogen bonded water dimer", Quarterly Journal of the Royal Meteorological Society **127**, 1627 (2001).

[63] L. Belau, K. R. Wilson, S. R. Leone, and M. Ahmed, "Vacuum ultraviolet (VUV) photoionization of small water clusters", J. Phys. Chem. A **111**, 10075 (2007).

[64] P. P. Radi, P. Beaud, D. Franzke, H.-M. Frey, T. Gerber, B. Mischler, and A.-P. Tzannis, "Femtosecond photoionization of $(H_2O)_n$ and $(D_2O)_n$ clusters", J. Chem. Phys. **111**, 512 (1999).

[65] F. Dong, S. Heinbuch, J. J. Rocca, and E. R. Bernstein, "Dynamics and fragmentation of van der waals clusters: $(H2O)_n$, $(CH_3OH)_n$, and $(NH_3)_n$ upon ionization by a 26.5ev soft x-ray laser", J. Chem. Phys. **124**, 224319 (2006).

[66] V. C. Felicíssimo, F. F. Guimarães, F. Gel'mukhanov, A. Cesar, and H. Ågren, "The principles of infrared-x-ray pump-probe spectroscopy. Applications on proton transfer in core-ionized water dimers", J. Chem. Phys. **122**, 094319 (2005).

[67] T. Jahnke, H. Sann, T. Havermeier, K. Kreidi, C. Stuck, M. Meckel, M. Schöffler, N. Neumann, R. Wallauer, S. Voss, A. Czasch, O. Jagutzki, A. Malakzadeh, F. Afaneh, T. Weber, H. Schmidt-Böcking, and R. Dörner, "Ultrafast energy transfer between water molecules", Nat. Phys. **6**, 139 (2010).

[68] A. T. J. B. Eppink and D. H. Parker, "Velocity map imaging of ions and electrons using electrostatic lenses: Application in photoelectron and photofragment ion imaging of molecular oxygen", Rev. Sci. Instrum. **68**, 3477 (1997).

[69] M. N. R. Ashfold, N. H. Nahler, A. J. Orr-Ewing, O. P. J. Vieuxmaire, R. L. Toomes, T. N. Kitsopoulos, I. A. Garcia, D. A. Chestakov, S.-M. Wu, and D. H. Parker, "Imaging the dynamics of gas phase reactions", Phys. Chem. Chem. Phys. **8**, 26 (2006).

[70] A. I. Chichinin, K. H. Gericke, S. Kauczok, and C. Maul, "Imaging chemical reactions — 3D velocity mapping", Int. Rev. Phys. Chem. **28**, 607 (2009).

[71] K. Pfeilsticker, A. Lotter, C. Peters, and H. Bösch, "Atmospheric detection of water dimers via near-infrared absorption", Science **300**, 2078 (2003).

[72] N. Goldman, C. Leforestier, and R. J. Saykally, "Water dimers in the atmosphere II: Results from VRT(ASP-W)III potential surface", J. Phys. Chem. A **108**, 787 (2004).

[73] N. Goldman, R. S. Fellers, C. Leforestier, and R. J. Saykally, "Water dimers in the atmosphere: Equilibrium constant for water dimerization from the VRT(ASP-W) potential surface", J. Phys. Chem. A **105**, 515 (2001).

[74] V. Vaida, "Perspective: Water cluster mediated atmospheric chemistry", J. Chem. Phys. **135** (2011).

[75] T. D. Gardiner, M. Coleman, H. Browning, L. Tallis, I. V. Ptashnik, and K. P. Shine, "Absolute high spectral resolution measurements of surface solar radiation for detection of water vapour continuum absorption", Philosophical Transactions of the Royal Society A: Mathematical, Physical and Engineering Sciences **370**, 2590 (2012).

[76] J. Tennyson, M. J. Barber, and R. E. A. Kelly, "An adiabatic model for calculating overtone spectra of dimers such as $(H_2O)_2$", Philosophical Transactions of the Royal Society A: Mathematical, Physical and Engineering Sciences **370**, 2656 (2012).

[77] Y. Scribano and C. Leforestier, "Contribution of water dimer absorption to the millimeter and far infrared atmospheric water continuum", The Journal of Chemical Physics **126**, 234301 (2007).

[78] J. M. Anglada and A. Solé, "Impact of the water dimer on the atmospheric reactivity of carbonyl oxides", Phys. Chem. Chem. Phys. **18**, 17698 (2016).

[79] J. Headrick and V. Vaida, "Significance of water complexes in the atmosphere", Physics and Chemistry of the Earth, Part C: Solar, Terrestrial & Planetary Science **26**, 479 (2001).

[80] L. Sheps, B. Rotavera, A. J. Eskola, D. L. Osborn, C. A. Taatjes, K. Au, D. E. Shallcross, M. A. H. Khan, and C. J. Percival, "The reaction of criegee intermediate CH_2OO

with water dimer: Primary products and atmospheric impact", Phys. Chem. Chem. Phys. **19**, 21970 (2017).

[81] V. Vaida, H. G. Kjaergaard, and K. J. Feierabend, "Hydrated complexes: Relevance to atmospheric chemistry and climate", Int. Rev. Phys. Chem. **22**, 203 (2003).

[82] S. Xantheas and T. Dunning, "Ab initio studies of cyclic water clusters $(H_2O)_n$, n=1–6. I. optimal structures and vibrational spectra", J. Chem. Phys. **99**, 8774 (1993).

[83] W. Klopper, J. G. C. M. van Duijneveldt-van de Rijdt, and F. B. van Duijneveldt, "Computational determination of equilibrium geometry and dissociation energy of the water dimer", Phys. Chem. Chem. Phys. **2**, 2227 (2000).

[84] T. R. Dyke and J. S. Muenter, "Molecular-beam electric deflection studies of water polymers", J. Chem. Phys. **57**, 5011 (1972).

[85] P. A. Kollman and L. C. Allen, "Theory of the hydrogen bond: Electronic structure and properties of the water dimer", J. Chem. Phys. **51**, 3286 (1969).

[86] J. Reimers and R. Watts, "The structure and vibrational spectra of small clusters of water molecules", Chemical Physics **85**, 83 (1984).

[87] R. Kalescky, W. Zou, E. Kraka, and D. Cremer, "Local vibrational modes of the water dimer – comparison of theory and experiment", Chem. Phys. Lett. **554**, 243 (2012).

[88] F. N. Keutsch, L. B. Braly, M. G. Brown, H. A. Harker, P. B. Petersen, C. Leforestier, and R. J. Saykally, "Water dimer hydrogen bond stretch, donor torsion overtone, and "in-plane bend" vibrations", The Journal of Chemical Physics **119**, 8927 (2003).

[89] Y. Bouteiller and J. Perchard, "The vibrational spectrum of $(H_2O)_2$: Comparison between anharmonic ab initio calculations and neon matrix infrared data between 9000 and 90 cm^{-1}", Chem. Phys. **305**, 1 (2004).

[90] L. B. Braly, K. Liu, M. G. Brown, F. N. Keutsch, R. S. Fellers, and R. J. Saykally, "Terahertz laser spectroscopy of the water dimer intermolecular vibrations. II. $(H_2O)_2$", J. Chem. Phys. **112**, 10314 (2000).

[91] P. R. Bunker and P. Jensen, *Fundamentals of Molecular Symmetry*, Series in Chemical Physics (Institute of Physics Publishing, Bristol, UK, 2005).

[92] L. Angel and A. J. Stace, "Dissociation patterns of $(H_2O)_n^+$ cluster ions, for n=2–6", Chem. Phys. Lett. **345**, 277 (2001).

[93] H. Shinohara, N. Nishi, and N. Washida, "Photoionization of water clusters at 11.83 eV: Observation of unprotonated cluster ions $(H_2O)_n^+$ ($2 \leq n \leq 10$)", J. Chem. Phys. **84**, 5561 (1986).

[94] C. Y. Ng, D. J. Trevor, P. W. Tiedemann, S. T. Ceyer, P. L. Kronebusch, B. H. Mahan, and Y. T. Lee, "Photoionization of dimeric polyatomic molecules: Proton affinities of h2o and hf", J. Chem. Phys. **67**, 4235 (1977).

[95] S. Tomoda and K. Kimura, "Proton-transfer potential-energy surfaces of the water dimer cation $(H_2O)_2^+$ in the 12A' "and 12A" states", Chem. Phys. **82**, 215 (1983).

[96] H. Tachikawa, "Ionization dynamics of a water dimer: Specific reaction selectivity", Phys. Chem. Chem. Phys. **13**, 11206 (2011).

[97] U. Buck and F. Huisken, "Infrared spectroscopy of size-selected water and methanol clusters", Chem. Rev. **100**, 3863 (2000).

[98] U. Buck, C. C. Pradzynski, T. Zeuch, J. M. Dieterich, and B. Hartke, "A size resolved investigation of large water clusters", Phys. Chem. Chem. Phys. **16**, 6859 (2014).

[99] C. Zhang, J. Lu, T. Feng, and H. Rottke, "Proton transfer dynamics following strong-field ionization of the water dimer", Phys. Rev. A **99**, 053408 (2019).

[100] S. D. Stoychev, A. I. Kuleff, and L. S. Cederbaum, "On the intermolecular coulombic decay of singly and doubly ionized states of water dimer", The Journal of Chemical Physics **133**, 154307 (2010).

[101] L. A. Curtiss, "Ab initio molecular orbital calculations of the first two adiabatic ionizations of the water dimer", Chem. Phys. Lett. **96**, 442 (1983).

[102] R. N. Barnett and U. Landman, "Pathways and dynamics of dissociation of ionized $(H_2O)_2$", The Journal of Physical Chemistry **99**, 17305 (1995).

[103] E. Miliordos, E. Aprà, and S. S. Xantheas, "Optimal geometries and harmonic vibrational frequencies of the global minima of water clusters $(H_2O)_n$, n = 2–6, and several hexamer local minima at the ccsd(t) level of theory", J. Chem. Phys. **139**, 114302 (2013).

[104] C. Pérez, S. Lobsiger, N. A. Seifert, D. P. Zaleski, B. Temelso, G. C. Shields, Z. Kisiel, and B. H. Pate, "Broadband fourier transform rotational spectroscopy for structure determination: The water heptamer", Chem. Phys. Lett. **571**, 1 (2013).

[105] C. Pérez, M. T. Muckle, D. P. Zaleski, N. A. Seifert, B. Temelso, G. C. Shields, Z. Kisiel, and B. H. Pate, "Structures of cage, prism, and book isomers of water hexamer from broadband rotational spectroscopy.", Science **336**, 897 (2012).

[106] J. K. Gregory, D. C. Clary, K. Liu, M. G. Brown, and R. J. Saykally, "The water dipole moment in water clusters", Science **275**, 814 (1997).

[107] K. Liu, M. G. Brown, J. D. Cruzan, and R. J. Saykally, "Vibration-rotation tunneling spectra of the water pentamer: Structure and dynamics", Science **271**, 62 (1996).

[108] J. D. Cruzan, L. B. Braly, K. Liu, M. G. Brown, J. G. Loeser, and R. J. Saykally, "Quantifying hydrogen bond cooperativity in water: VRT spectroscopy of the water tetramer", Science **271**, 59 (1996).

[109] K. Liu, M. G. Brown, C. Carter, R. J. Saykally, J. K. Gregory, and D. C. Clary, "Characterization of a cage form of the water hexamer", Nature **381**, 501 (1996).

[110] D. H. Levy, "The spectroscopy of very cold gases", Science **214**, 263 (1981).

[111] E. Illenberger and J. Momigny, *Gaseous Molecular Ions: An Introduction to Elementary Processes Induced by Ionization*, Topics in Physical Chemistry (Steinkopff, 2013).

[112] S. Y. T. van de Meerakker, H. L. Bethlem, and G. Meijer, "Taming molecular beams", Nat. Phys. **4**, 595 (2008).

[113] E. Becker, K. Bier, and W. Henkes, "Strahlen aus kondensierten Atomen und Molekülen im Hochvakuum", Z. Phys. **146**, 333 (1956).

[114] O. F. Hagena, "Cluster ion sources (invited)", Rev. Sci. Instrum. **63**, 2374 (1992).

[115] O. F. Hagena, "Condensation in free jets: Comparison of rare gases and metals", Z. Phys. D **4**, 291 (1987).

[116] O. F. Hagena, "Nucleation and growth of clusters in expanding nozzle flows", Surface Science **106**, 101 (1981).

[117] O. G. Danylchenko, S. I. Kovalenko, and V. N. Samovarov, "Experimental verification of the hagena relation for large clusters formed in a conical nozzle", Tech. Phys. Lett. **34**, 1037 (2008).

[118] I. Yamada, *Materials Processing by Cluster Ion Beams: History, Technology, and Applications* (CRC Press, 2015).

[119] C. Bobbert, S. Schutte, C. Steinbach, and U. Buck, "Fragmentation and reliable size distributions of large ammonia and water clusters", European Phys. J. D **19**, 183 (2002).

[120] I. Pócsik, "Lognormal distribution as the natural statistics of cluster systems", Z. Phys. D **20**, 395 (1991).

[121] M. D. Morse, in *Atomic, Molecular, and Optical Physics: Atoms and Molecules*, Experimental Methods in the Physical Sciences, Vol. 29, edited by F. Dunning and R. G. Hulet (Academic Press, 1996) pp. 21 – 47.

[122] R. E. Smalley, L. Wharton, and D. H. Levy, "Molecular optical spectroscopy with supersonic beams and jets", Acc. Chem. Res. **10**, 139 (1977).

[123] H. Pauly, *Atom, Molecule, and Cluster Beams II*, Cluster Beams, Fast and Slow Beams, Accessory Equipment and Applications, Springer Series on Atomic, Optical, and Plasma Physics, Vol. 32 (Springer Verlag, 2000).

[124] J. S. Kienitz, S. Trippel, T. Mullins, K. Długołęcki, R. González-Férez, and J. Küpper, "Adiabatic mixed-field orientation of ground-state-selected carbonyl sulfide molecules", Chem. Phys. Chem. **17**, 3740 (2016).

[125] J. Wang, L. He, J. Petrovic, A. Al-Refaie, H. Bieker, J. Onvlee, K. Długołęcki, and J. Küpper, "Spatial separation of 2-propanol monomer and its ionization-fragmentation pathways", J. Mol. Struct. **1208**, 127863 (2020).

[126] Y.-P. Chang, F. Filsinger, B. Sartakov, and J. Küpper, "CMISTARK: Python package for the Stark-effect calculation and symmetry classification of linear, symmetric and asymmetric top wavefunctions in dc electric fields", Comp. Phys. Comm. **185**, 339 (2014), current version available from GitHub.

[127] S. L. Shostak, W. L. Ebenstein, and J. S. Muenter, "The dipole moment of water. I. dipole moments and hyperfine properties of H_2O and HDO in the ground and excited vibrational states", J. Chem. Phys. **94**, 5875 (1991).

[128] F. C. DeLucia, P. Helminger, and W. H. Kirchhoff, "Microwave spectra of molecules of astrophysical interest V. Water vapor", J. Phys. Chem. Ref. Data **3**, 211 (1974).

[129] N. P. Malomuzh, V. N. Makhlaichuk, and S. V. Khrapatyi, "Water dimer dipole moment", Russ. J. Phys. Chem. A **88**, 1431 (2014).

[130] L. H. Coudert and J. T. Hougen, "Analysis of the microwave and far infrared spectrum of the water dimer", J. Mol. Spectrosc. **139**, 259 (1990).

[131] F. N. Keutsch, J. D. Cruzan, and R. J. Saykally, "The water trimer", Chem. Rev. **103**, 2533 (2003).

[132] A. Owens and A. Yachmenev, "RichMol: A general variational approach for rovibrational molecular dynamics in external electric fields", J. Chem. Phys. **148**, 124102 (2018).

[133] B. Zhang, R. Wepf, K. Fischer, M. Schmidt, S. Besse, P. Lindner, B. T. King, R. Sigel, P. Schurtenberger, Y. Talmon, Y. Ding, M. Kröger, A. Halperin, and A. D. Schlüter, "The largest synthetic structure with molecular precision: Towards a molecular object", Angew. Chem. Int. Ed. **50**, 737 (2011).

[134] K. Amini, J. Biegert, F. Calegari, A. Chacón, M. F. Ciappina, A. Dauphin, D. K. Efimov, C. F. de Morisson Faria, K. Giergiel, P. Gniewek, A. S. Landsman, M. Lesiuk, M. Mandrysz, A. S. Maxwell, R. Moszyński, L. Ortmann, J. A. Pérez-Hernández, A. Picón, E. Pisanty, J. Prauzner-Bechcicki, K. Sacha, N. Suárez, A. Zaïr, J. Zakrzewski,

and M. Lewenstein, "Symphony on strong field approximation", Rep. Prog. Phys. **82**, 116001 (2019).

[135] L. Keldysh, "Ionization in the field of a strong electromagnetic wave", J. Exp. Theor. Phys. **20**, 1307 (1965).

[136] R. Wang, Q. Zhang, D. Li, S. Xu, P. Cao, Y. Zhou, W. Cao, and P. Lu, "Identification of tunneling and multiphoton ionization in intermediate keldysh parameter regime", Opt. Exp. **27**, 6471 (2019).

[137] M. Klaiber and J. S. Briggs, "Crossover from tunneling to multiphoton ionization of atoms", Phys. Rev. A **94**, 053405 (2016).

[138] L. Fechner, "Ionization in strong, ultrashort laser pulses", in *High-Resolution Experiments on Strong-Field Ionization of Atoms and Molecules: Test of Tunneling Theory, the Role of Doubly Excited States, and Channel-Selective Electron Spectra* (Springer International Publishing, Cham, 2016) pp. 29–51.

[139] J. Laskin and C. Lifshitz, "Kinetic energy release distributions in mass spectrometry", J. Mass. Spectrom. **36**, 459 (2001).

[140] A. K. Pandey, *Dissociation Dynamics of Unstable Molecular Systems*, Dissertation, Mohanlal Sukhadia University, UDAIPUR, India (2014).

[141] M. R. Jana, *Dynamics and kinetics of ion impact dissociation of molecules*, Dissertation, University of Calcutta, Kolkata, India (2013).

[142] R. G. Cooks and J. H. Beynon, "Metastable ions and ion kinetic energy spectrometry: The development of a new research area", J. Chem. Educ. **51**, 437 (1974).

[143] W. Wiley and I. Mclaren, "Time-of-flight mass spectrometer with improved resolution", Rev. Sci. Instrum. **26**, 1150 (1955).

[144] Scientific Instrument Services Inc., USA, "Simion 8.1" (2011), URL: `http://simion.com`.

[145] J. Cooper and R. N. Zare, "Angular distribution of photoelectrons", J. Chem. Phys. **48**, 942 (1968).

[146] S. Wallace and D. Dill, "Detector integrated angular distribution: Chemisorption-site geometry, axial-recoil photofragmentation, and molecular-beam orientation", Phys. Rev. B **17**, 1692 (1978).

[147] J. S. Kienitz, K. Długołęcki, S. Trippel, and J. Küpper, "Improved spatial separation of neutral molecules", J. Chem. Phys. **147**, 024304 (2017).

[148] S. Trippel, M. Johny, T. Kierspel, J. Onvlee, H. Bieker, H. Ye, T. Mullins, L. Gumprecht, K. Długołęcki, and J. Küpper, "Knife edge skimming for improved separation of molecular species by the deflector", Rev. Sci. Instrum. **89**, 096110 (2018).

[149] G. A. Jeffrey, *An Introduction to Hydrogen Bonding* (Oxford University Press, 1997).

[150] K. Liu, J. Cruzan, and R. Saykally, "Water clusters", Science **271**, 929 (1996).

[151] K. Nauta and R. E. Miller, "Formation of cyclic water hexamer in liquid helium: The smallest piece of ice", Science **287**, 293 (2000).

[152] G. T. Dunning, D. R. Glowacki, T. J. Preston, S. J. Greaves, G. M. Greetham, I. P. Clark, M. Towrie, J. N. Harvey, and A. J. Orr-Ewing, "Vibrational relaxation and microsolvation of DF after F-atom reactions in polar solvents", Science **347**, 530 (2015).

[153] T. M. Korter, D. W. Pratt, and J. Küpper, "Indole-H_2O in the gas phase. Structures, barriers to internal motion, and $S_1 \leftarrow S_0$ transition moment orientation. Solvent reorganization in the electronically excited state", J. Phys. Chem. A **102**, 7211 (1998).

[154] A. L. Sobolewski and W. Domcke, "Photoinduced electron and proton transfer in phenol and its clusters with water and ammonia", J. Phys. Chem. A **105**, 9275 (2001).

[155] X. Ren, E. Wang, A. D. Skitnevskaya, A. B. Trofimov, G. Kirill, and A. Dorn, "Experimental evidence for ultrafast intermolecular relaxation processes in hydrated biomolecules", Nat. Phys. **79**, 1745 (2018).

[156] H. Yu and W. F. van Gunsteren, "Charge-on-spring polarizable water models revisited: From water clusters to liquid water to ice", J. Chem. Phys. **121**, 9549 (2004).

[157] T. Marchenko, L. Inhester, G. Goldsztejn, O. Travnikova, L. Journel, R. Guillemin, I. Ismail, D. Koulentianos, D. Céolin, R. Püttner, M. N. Piancastelli, and M. Simon, "Ultrafast nuclear dynamics in the doubly-core-ionized water molecule observed via auger spectroscopy", Phys. Rev. A **98**, 063403 (2018).

[158] A. Kilaj, H. Gao, D. Rösch, U. Rivero, J. Küpper, and S. Willitsch, "Observation of different reactivities of para- and ortho-water towards trapped diazenylium ions", Nat. Commun. **9**, 2096 (2018).

[159] R. Boll, B. Erk, R. Coffee, S. Trippel, T. Kierspel, C. Bomme, J. D. Bozek, M. Burkett, S. Carron, K. R. Ferguson, L. Foucar, J. Küpper, T. Marchenko, C. Miron, M. Patanen, T. Osipov, S. Schorb, M. Simon, M. Swiggers, S. Techert, K. Ueda, C. Bostedt, D. Rolles, and A. Rudenko, "Charge transfer in dissociating iodomethane and fluoromethane molecules ionized by intense femtosecond x-ray pulses", Struct. Dyn. **3**, 043207 (2016).

[160] T. Kierspel, *Imaging structure and dynamics using controlled molecules*, Dissertation, Universität Hamburg, Hamburg, Germany (2016).

[161] B. Winter, E. F. Aziz, U. Hergenhahn, M. Faubel, and I. V. Hertel, "Hydrogen bonds in liquid water studied by photoelectron spectroscopy", J. Chem. Phys. **126**, 124504 (2007).

[162] J. D. Smith, C. D. Cappa, K. R. Wilson, B. M. Messer, R. C. Cohen, and R. J. Saykally, "Energetics of hydrogen bond network rearrangements in liquid water", Science **306**, 851 (2004).

[163] T. S. Zwier, "The spectroscopy of solvation in hydrogen-bonded aromatic clusters", Annu. Rev. Phys. Chem. **47**, 205 (1996).

[164] J. B. Paul, C. P. Collier, R. J. Saykally, J. J. Scherer, and A. O'Keefe, "Direct measurement of water cluster concentrations by infrared cavity ringdown laser absorption spectroscopy", J. Phys. Chem. A **101**, 5211 (1997).

[165] F. Filsinger, U. Erlekam, G. von Helden, J. Küpper, and G. Meijer, "Selector for structural isomers of neutral molecules", Phys. Rev. Lett. **100**, 133003 (2008).

[166] F. Filsinger, J. Küpper, G. Meijer, J. L. Hansen, J. Maurer, J. H. Nielsen, L. Holmegaard, and H. Stapelfeldt, "Pure samples of individual conformers: The separation of stereoisomers of complex molecules using electric fields", Angew. Chem. Int. Ed. **48**, 6900 (2009).

[167] J. H. Nielsen, P. Simesen, C. Z. Bisgaard, H. Stapelfeldt, F. Filsinger, B. Friedrich, G. Meijer, and J. Küpper, "Stark-selected beam of ground-state OCS molecules characterized by revivals of impulsive alignment", Phys. Chem. Chem. Phys. **13**, 18971 (2011).

[168] H. S. You, J. Kim, S. Han, D.-S. Ahn, J. S. Lim, and S. K. Kim, "Spatial isolation of conformational isomers of hydroquinone and its water cluster using the stark deflector", J. Phys. Chem. A **122**, 1194 (2018).

[169] R. Moro, J. Bulthuis, J. Heinrich, and V. V. Kresin, "Electrostatic deflection of the water molecule: A fundamental asymmetric rotor", Phys. Rev. A **75**, 013415 (2007).

[170] R. Moro, R. Rabinovitch, C. Xia, and V. V. Kresin, "Electric dipole moments of water clusters from a beam deflection measurement", Phys. Rev. Lett. **97**, 123401 (2006).

[171] C. C. Pradzynski, R. M. Forck, T. Zeuch, P. Slavíček, and U. Buck, "A fully size-resolved perspective on the crystallization of water clusters", Science **337**, 1529 (2012).

[172] J. Küpper, S. Stern, L. Holmegaard, F. Filsinger, A. Rouzée, A. Rudenko, P. Johnsson, A. V. Martin, M. Adolph, A. Aquila, S. Bajt, A. Barty, C. Bostedt, J. Bozek, C. Caleman, R. Coffee, N. Coppola, T. Delmas, S. Epp, B. Erk, L. Foucar, T. Gorkhover, L. Gumprecht, A. Hartmann, R. Hartmann, G. Hauser, P. Holl, A. Hömke, N. Kimmel, F. Krasniqi, K.-U. Kühnel, J. Maurer, M. Messerschmidt, R. Moshammer, C. Reich, B. Rudek, R. Santra, I. Schlichting, C. Schmidt, S. Schorb, J. Schulz, H. Soltau, J. C. H. Spence, D. Starodub, L. Strüder, J. Thøgersen, M. J. J. Vrakking, G. Weidenspointner, T. A. White, C. Wunderer, G. Meijer, J. Ullrich, H. Stapelfeldt, D. Rolles, and H. N. Chapman, "X-ray diffraction from isolated and strongly aligned gas-phase molecules with a free-electron laser", Phys. Rev. Lett. **112**, 083002 (2014).

[173] S. Stern, L. Holmegaard, F. Filsinger, A. Rouzée, A. Rudenko, P. Johnsson, A. V. Martin, A. Barty, C. Bostedt, J. D. Bozek, R. N. Coffee, S. Epp, B. Erk, L. Foucar, R. Hartmann, N. Kimmel, K.-U. Kühnel, J. Maurer, M. Messerschmidt, B. Rudek, D. G. Starodub, J. Thøgersen, G. Weidenspointner, T. A. White, H. Stapelfeldt, D. Rolles, H. N. Chapman, and J. Küpper, "Toward atomic resolution diffractive imaging of isolated molecules with x-ray free-electron lasers", Faraday Disc. **171**, 393 (2014).

[174] F. Filsinger, J. Küpper, G. Meijer, L. Holmegaard, J. H. Nielsen, I. Nevo, J. L. Hansen, and H. Stapelfeldt, "Quantum-state selection, alignment, and orientation of large molecules using static electric and laser fields", J. Chem. Phys. **131**, 064309 (2009).

[175] G. Maroulis, "Static hyperpolarizability of the water dimer and the interaction hyperpolarizability of two water molecules", J. Chem. Phys. **113**, 1813 (2000).

[176] X. Liu, W.-C. Lu, C. Wang, and K. Ho, "Energetic and fragmentation stability of water clusters $(H_2O)_n$, n=2–30", Chem. Phys. Lett. **508**, 270 (2011).

[177] C. J. Hensley, J. Yang, and M. Centurion, "Imaging of isolated molecules with ultrafast electron pulses", Phys. Rev. Lett. **109**, 133202 (2012).

[178] T. Kierspel, C. Bomme, M. Di Fraia, J. Wiese, D. Anielski, S. Bari, R. Boll, B. Erk, J. S. Kienitz, N. L. M. Müller, D. Rolles, J. Viefhaus, S. Trippel, and J. Küpper, "Photophysics of indole upon X-ray absorption", Phys. Chem. Chem. Phys. **20**, 20205 (2018).

[179] A. Bauder, "Fundamentals of rotational spectroscopy", in *Handbook of High-resolution Spectroscopy* (American Cancer Society, 2011) https://onlinelibrary.wiley.com/doi/pdf/10.1002/9780470749593.hrs002.

[180] J. J. Omiste and L. B. Madsen, "Torsional and rotational couplings in nonrigid molecules", Phys. Rev. A **95**, 023402 (2017).

[181] C. B. Madsen, L. B. Madsen, S. S. Viftrup, M. P. Johansson, T. B. Poulsen, L. Holmegaard, V. Kumarappan, K. A. Jørgensen, and H. Stapelfeldt, "A combined experimental and theoretical study on realizing and using laser controlled torsion of molecules", J. Chem. Phys. **130**, 234310 (2009).

[182] R. T. Hall and J. M. Dowling, "Pure rotational spectrum of water vapor", J. Chem. Phys. **47**, 2454 (1967).

[183] J. Sarka, A. G. Császár, S. C. Althorpe, D. J. Wales, and E. Mátyus, "Rovibrational transitions of the methane–water dimer from intermolecular quantum dynamical computations", Phys. Chem. Chem. Phys. **18**, 22816 (2016).

[184] Y. Saleh, *On (Non)adiabatic Dynamics of Deflected Molecular Beams (analysis and simulation)*, Master thesis, University of L'Aquila, L'Aquila, Italy (2019).

[185] J. S. Brodbelt, "Photodissociation mass spectrometry: New tools for characterization of biological molecules", Chem. Soc. Rev. **43**, 2757 (2014).

[186] J. P. Reilly, "Ultraviolet photofragmentation of biomolecular ions", Mass Spectrom. Rev. **28**, 425 (2009).

[187] J. B. Shaw, W. Li, D. D. Holden, Y. Zhang, J. Griep-Raming, R. T. Fellers, B. P. Early, P. M. Thomas, N. L. Kelleher, and J. S. Brodbelt, "Complete protein characterization using top-down mass spectrometry and ultraviolet photodissociation", J. Am. Chem. Soc. **135**, 12646 (2013), pMID: 23697802.

[188] J. P. O'Brien, W. Li, Y. Zhang, and J. S. Brodbelt, "Characterization of native protein complexes using ultraviolet photodissociation mass spectrometry", Journal of the American Chemical Society **136**, 12920 (2014), pMID: 25148649.

[189] L. Lammich, J. Rajput, and L. H. Andersen, "Photodissociation pathways of gas-phase photoactive yellow protein chromophores", Phys. Rev. E **78**, 051916 (2008).

[190] L. H. Andersen, H. Bluhme, S. Boyé, T. J. D. Jørgensen, H. Krogh, I. B. Nielsen, S. Brøndsted Nielsen, and A. Svendsen, "Experimental studies of the photophysics of gas-phase fluorescent protein chromophores", Phys. Chem. Chem. Phys. **6**, 2617 (2004).

[191] F. Canon, A. Milosavljević, G. van der Rest, M. Réfrégiers, L. Nahon, P. Sarni-Manchado, V. Cheynier, and A. Giuliani, "Photodissociation and dissociative photoionization mass spectrometry of proteins and noncovalent protein–ligand complexes", Angew. Chem. Int. Ed. **52**, 8377 (2013).

[192] D. T. Ha, M. A. Huels, M. Huttula, S. Urpelainen, and E. Kukk, "Experimental and *ab initio* study of the photofragmentation of DNA and RNA sugars", Phys. Rev. A **84**, 033419 (2011).

[193] E. Sarantopoulou, Z. Kollia, A. Cefalas, S. Kobe, and Z. Samardžija, "Photodissociation dynamics of DNA bases", Journal of Biological Physics **29**, 149 (2003).

[194] H. Bieker, J. Onvlee, M. Johny, L. He, T. Kierspel, S. Trippel, D. A. Horke, and J. Küpper, "Pure molecular beam of water dimer", J. Phys. Chem. A **123**, 7486 (2019).

[195] J. Zhang, Y. Yang, Z. Li, S. Zhang, and Z. Sun, "Dissociative photoionization of 1,2-dichloroethane in intense near-infrared femtosecond laser field", Chem. Phys. Lett. **667**, 238 (2017).

[196] B. Dick, "Inverting ion images without abel inversion: Maximum entropy reconstruction of velocity maps", Phys. Chem. Chem. Phys. **16**, 570 (2014).

[197] L. Christensen, L. Christiansen, B. Shepperson, and H. Stapelfeldt, "Deconvoluting nonaxial recoil in Coulomb explosion measurements of molecular axis alignment", Phys. Rev. A **94**, 023410 (2016).

[198] B. Liu, Y. Yang, H. Sun, and Z. Sun, "Dissociative ionization and coulomb explosion of molecular bromocyclopropane in an intense femtosecond laser field", Molecules **23**, 3039 (2018).

[199] Y. Yan, J. Long, and Y. Liu, "Study on photodynamics of furan via strong field multiphoton ionization by velocity map imaging technique", Chem. Phys. **530**, 110611 (2020).

[200] X. Llopart, R. Ballabriga, M. Campbell, L. Tlustos, and W. Wong, "Timepix, a 65k programmable pixel readout chip for arrival time, energy and/or photon counting measurements", Nucl. Instrum. Meth. A **581**, 485 (2007).

[201] A. Roberts, P. Svihra, A. Al-Refaie, H. Graafsma, J. Küpper, K. Majumdar, K. Mavrokoridis, A. Nomerotski, D. Pennicard, B. Philippou, S. Trippel, C. Touramanis, and J. Vann, "First demonstration of 3D optical readout of a TPC using a single photon sensitive Timepix3 based camera", J. Instrum. **14**, P06001 (2019).

[202] A. Zhao, M. van Beuzekom, B. Bouwens, D. Byelov, I. Chakaberia, C. Cheng, E. Maddox, A. Nomerotski, P. Svihra, J. Visser, V. Vrba, and T. Weinacht, "Coincidence velocity map imaging using Tpx3Cam, a time stamping optical camera with 1.5 ns timing resolution", Rev. Sci. Instrum. **88**, 113104 (2017).

[203] A. Al-Refaie, M. Johny, J. Correa, D. Pennicard, P. Svihra, A. Nomerotski, S. Trippel, and J. Küpper, "PymePix: A python library for SPIDR readout of Timepix3", J. Instrum. **14**, P10003 (2019).

[204] B. K. McFarland, J. P. Farrell, S. Miyabe, F. Tarantelli, A. Aguilar, N. Berrah, C. Bostedt, J. D. Bozek, P. H. Bucksbaum, J. C. Castagna, R. N. Coffee, J. P. Cryan, L. Fang, R. Feifel, K. J. Gaffney, J. M. Glownia, T. J. Martinez, M. Mucke, B. Murphy, A. Natan,

T. Osipov, V. S. Petrovic, S. Schorb, T. Schultz, L. S. Spector, M. Swiggers, I. Tenney, S. Wang, J. L. White, W. White, and M. Gühr, "Ultrafast x-ray auger probing of photoexcited molecular dynamics.", Nat. Commun. **5**, 4235 (2014).

[205] M. N. Piancastelli, R. Guillemin, T. Marchenko, L. Journel, O. Travnikova, T. Marin, G. Goldsztejn, B. C. de Miranda, I. Ismail, and M. Simon, "New achievements on relaxation dynamics of atoms and molecules photoexcited in the tender x-ray domain at synchrotron SOLEIL", Journal of Physics B: Atomic, Molecular and Optical Physics **50**, 042001 (2017).

[206] B. Erk, D. Rolles, L. Foucar, B. Rudek, S. W. Epp, M. Cryle, C. Bostedt, S. Schorb, J. Bozek, A. Rouzee, A. Hundertmark, T. Marchenko, M. Simon, F. Filsinger, L. Christensen, S. De, S. Trippel, J. Küpper, H. Stapelfeldt, S. Wada, K. Ueda, M. Swiggers, M. Messerschmidt, C. D. Schroter, R. Moshammer, I. Schlichting, J. Ullrich, and A. Rudenko, "Ultrafast charge rearrangement and nuclear dynamics upon inner-shell multiple ionization of small polyatomic molecules", Phys. Rev. Lett. **110**, 053003 (2013).

[207] U. Hergenhahn, "Interatomic and intermolecular coulombic decay: The early years", J. Electron. Spectrosc. Relat. Phenom. **184**, 78 (2011), advances in Vacuum Ultraviolet and X-ray Physics.

[208] J. H. D. Eland, "The dynamics of three-body dissociations of dications studied by the triple coincidence technique PEPIPICO", Mol. Phys. **61**, 725 (1987).

[209] J. Ullrich, R. Moshammer, A. Dorn, R. Dörner, L. P. H. Schmidt, and H. Schmidt-Böcking, "Recoil-ion and electron momentum spectroscopy: Reaction-microscopes", Rep. Prog. Phys. **66**, 1463 (2003).

[210] J. Ullrich, R. Moshammer, R. Dörner, O. Jagutzki, V. Mergel, H. Schmidt-Böcking, and L. Spielberger, "Recoil-ion momentum spectroscopy", J. Phys. B **30**, 2917 (1997).

[211] C. Bomme, R. Guillemin, T. Marin, L. Journel, T. Marchenko, D. Dowek, N. Trcera, B. Pilette, A. Avila, H. Ringuenet, R. K. Kushawaha, and M. Simon, "Double momentum spectrometer for ion-electron vector correlations in dissociative photoionization.", Rev. Sci. Instrum. **84**, 103104 (2013).

[212] R. Guillemin, C. Bomme, T. Marin, L. Journel, T. Marchenko, R. K. Kushawaha, N. Trcera, M. N. Piancastelli, and M. Simon, "Complex decay patterns in atomic core photoionization disentangled by ion-recoil measurements", Phys. Rev. A **84**, 063425 (2011).

[213] D. Dowek, A. Haouas, R. Guillemin, C. Elkharrat, J. C. Houver, W. B. Li, F. Catoire, L. Journel, M. Simon, and R. R. Lucchese, "Recoil frame photoemission in inner-shell

photoionization of small polyatomic molecules", Eur. Phys. J. Special Topics **169**, 85 (2009).

[214] H. Levola, E. Itala, K. Schlesier, K. Kooser, S. Laine, J. Laksman, D. T. Ha, E. Rachlew, M. Tarkanovskaja, K. Tanzer, and E. Kukk, "Ionization-site effects on the photofragmentation of chloro- and bromoacetic acid molecules", Phys. Rev. A **92**, 063409 (2015).

[215] E. Kukk, D. T. Ha, Y. Wang, D. G. Piekarski, S. Diaz-Tendero, K. Kooser, E. Itala, H. Levola, M. Alcami, E. Rachlew, and F. Martín, "Internal energy dependence in x-ray-induced molecular fragmentation: An experimental and theoretical study of thiophene", Phys. Rev. A **91**, 043417 (2015).

[216] D. Attwood, *Soft x-rays and extreme ultraviolet radiation: principles and applications* (Cambridge University Press, University of California, Berkeley, 2000).

[217] J. Als-Nielsen and D. McMorrow, *Elements of Modern X-ray Physics* (John Wiley & Sons, Chichester, West Sussex, United Kingdom, 2001).

[218] V. Felicíssimo, I. Minkov, F. G. Åes, F. Gel'mukhanov, A. Cesar, and H. Ågren, "A theoretical study of the role of the hydrogen bond on core ionization of the water dimer", Chem. Phys. **312**, 311 (2005).

[219] "Cross-sections and asymmetry parameters".

[220] K. Bennett, Y. Zhang, M. Kowalewski, W. Hua, and S. Mukamel, "Multidimensional resonant nonlinear spectroscopy with coherent broadband x-ray pulses", Phys. Scr. **T169**, 014002 (2016).

[221] R. Rey, K. B. Møller, and J. T. Hynes, "Hydrogen bond dynamics in water and ultrafast infrared spectroscopy", J. Phys. Chem. A **106**, 11993 (2002).

[222] S. A. Yamada, W. H. Thompson, and M. D. Fayer, "Water-anion hydrogen bonding dynamics: Ultrafast IR experiments and simulations", J. Chem. Phys. **146**, 234501 (2017).

[223] C. Zhou, X. Li, Z. Gong, C. Jia, Y. Lin, C. Gu, G. He, Y. Zhong, J. Yang, and X. Guo, "Direct observation of single-molecule hydrogen-bond dynamics with single-bond resolution", Nat. Commun. **9**, 2041 (2018).

[224] E. T. Karamatskos, S. Raabe, T. Mullins, A. Trabattoni, P. Stammer, G. Goldsztejn, R. R. Johansen, K. Długołęcki, H. Stapelfeldt, M. J. J. Vrakking, S. Trippel, A. Rouzée, and J. Küpper, "Molecular movie of ultrafast coherent rotational dynamics of OCS", Nat. Commun. **10**, 3364 (2019).

[225] M. P. Minitti, J. M. Budarz, A. Kirrander, J. S. Robinson, D. Ratner, T. J. Lane, D. Zhu, J. M. Glownia, M. Kozina, H. T. Lemke, M. Sikorski, Y. Feng, S. Nelson, K. Saita, B. Stankus, T. Northey, J. B. Hastings, and P. M. Weber, "Imaging molecular motion: Femtosecond x-ray scattering of an electrocyclic chemical reaction", Phys. Rev. Lett. **114**, 255501 (2015).

[226] H. N. Chapman, in *Biology with FELs: Toward the Molecular Movie* (Lawrence Berkeley National Laboratory, Berkeley, CA 94720, USA, 2011).

[227] C. M. Günther, B. Pfau, R. Mitzner, B. Siemer, S. Roling, H. Zacharias, O. Kutz, I. Rudolph, D. Schondelmaier, R. Treusch, and S. Eisebitt, "Sequential femtosecond x-ray imaging", Nature Photonics **5**, 99 (2011).

[228] R. J. D. Miller, R. Ernstorfer, M. Harb, M. Gao, C. T. Hebeisen, H. Jean-Ruel, C. Lu, G. Moriena, and G. Sciaini, "'Making the molecular movie': First frames", Acta Crystallogr A **66**, 137 (2010).

[229] J. H. D. Eland and V. Schmidt, "Coincidence measurements on ions and electrons", in *VUV and Soft X-Ray Photoionization*, edited by U. Becker and D. A. Shirley (Springer US, Boston, MA, 1996) pp. 495–520.

[230] T. Poikela, J. Plosila, T. Westerlund, M. Campbell, M. De Gaspari, X. Llopart, V. Gromov, R. Kluit, M. van Beuzekom, F. Zappon, V. Zivkovicd, C. Brezinae, K. Desche, Y. Fue, and A. Kruth, "Timepix3: a 65K channel hybrid pixel readout chip with simultaneous ToA/ToT and sparse readout", J. Instrum. **9**, C05013 (2014).

[231] E. Frojdh, M. Campbell, M. D. Gaspari, S. Kulis, X. Llopart, T. Poikela, and L. Tlustos, "Timepix3: first measurements and characterization of a hybrid-pixel detector working in event driven mode", J. Instrum. **10**, C01039 (2015).

[232] J. C. Tully, "Molecular dynamics with electronic transitions", The Journal of Chemical Physics **93**, 1061 (1990).

[233] E. Towns-Andrews, A. Berry, J. Bordas, G. R. Mant, P. K. Murray, K. Roberts, I. Sumner, J. S. Worgan, R. Lewis, and A. Gabriel, "Time-resolved x-ray diffraction station: X-ray optics, detectors, and data acquisition", Rev. Sci. Instrum. **60**, 2346 (1989).

[234] M. G. Pullen, B. Wolter, A.-T. Le, M. Baudisch, M. Hemmer, A. Senftleben, C. D. Schroter, J. Ullrich, R. Moshammer, C. D. Lin, and J. Biegert, "Imaging an aligned polyatomic molecule with laser-induced electron diffraction", Nat. Commun. **6**, 7262 (2015).

[235] C. I. Blaga, J. Xu, A. D. DiChiara, E. Sistrunk, K. Zhang, P. Agostini, T. A. Miller, L. F. DiMauro, and C. D. Lin, "Imaging ultrafast molecular dynamics with laser-induced electron diffraction", Nature **483**, 194 (2012).

[236] J. Xu, C. I. Blaga, K. Zhang, Y. H. Lai, C. D. Lin, T. A. Miller, P. Agostini, and L. F. DiMauro, "Diffraction using laser-driven broadband electron wave packets", Nat. Commun. **5**, 4635 (2014).

[237] B. P. Gorshunov, E. S. Torgashev, V. I.and Zhukova, V. G. Thomas, M. A. Belyanchikov, C. Kadlec, F. Kadlec, M. Savinov, T. Ostapchuk, J. Petzelt, J. Prokleška, P. V. Tomas, E. V. Pestrjakov, D. A. Fursenko, G. S. Shakurov, A. S. Prokhorov, V. S. Gorelik, L. S. Kadyrov, V. V. Uskov, R. K. Kremer, and M. Dressel, "Field-free molecular alignment probed by the free electron laser in Hamburg (FLASH)", Nat. Commun. **7**, 12842 (2016).

[238] M. Yang, P. Senet, and C. Van Alsenoy, "DFT study of polarizabilities and dipole moments of water clusters", Int. J. Quantum Chem. **101**, 535 (2005).

[239] J. R. Hammond, N. Govind, K. Kowalski, J. Autschbach, and S. S. Xantheas, "Accurate dipole polarizabilities for water clusters n=2–12 at the coupled-cluster level of theory and benchmarking of various density functionals", J. Chem. Phys. **131**, 214103 (2009).

[240] B. Lindner and U. Seydel, "Laser desorption mass spectrometry of nonvolatiles under shock wave conditions", Anal. Chem. **57**, 895 (1985).

[241] V. V. Golovlev, S. L. Allman, W. R. Garrett, N. I. Taranenko, and C. H. Chen, "Laser-induced acoustic desorption", Int. J. Mass Spectrom. Ion Processes **169–170**, 69 (1997).

[242] W.-P. Peng, Y.-C. Yang, M.-W. Kang, Y.-K. Tzeng, Z. Nie, H.-C. Chang, W. Chang, and C.-H. Chen, "Laser-induced acoustic desorption mass spectrometry of single bioparticles", Angew. Chem. Int. Ed. **45**, 1423 (2006).

[243] L. Nyadong, J. P. Quinn, C. S. Hsu, C. L. Hendrickson, R. P. Rodgers, and A. G. Marshall, "Atmospheric pressure laser-induced acoustic desorption chemical ionization mass spectrometry for analysis of saturated hydrocarbons", Anal. Chem. **84**, 7131 (2012).

[244] R. Tembreull and D. M. Lubman, "Resonant two-photon ionization of small peptides using pulsed laser desorption in supersonic beam mass spectrometry", Anal. Chem. **59**, 1003 (1987).

[245] G. Meijer, M. S. de Vries, H. E. Hunziker, and H. R. Wendt, "Laser desorption jet-cooling of organic molecules – cooling characteristics and detection sensitivity", Appl. Phys. B **51**, 395 (1990).

[246] E. Nir, K. Kleinermanns, and M. S. de Vries, "Pairing of isolated nucleic-acid bases in the absence of the DNA backbone", Nature **408**, 949 (2000).

[247] M. S. de Vries and P. Hobza, "Gas-phase spectroscopy of biomolecular building blocks", Annu. Rev. Phys. Chem. **58**, 585 (2007).

[248] N. Teschmit, K. Długołęcki, D. Gusa, I. Rubinsky, D. A. Horke, and J. Küpper, "Characterizing and optimizing a laser-desorption molecular beam source", J. Chem. Phys. **147**, 144204 (2017).

[249] S. Techert, S. Thekku Veedu, and S. Bari, "Development of ultrafast x-ray free electron laser tools in (bio)chemical research", in *Nanoscale Photonic Imaging*, edited by T. Salditt, A. Egner, and D. R. Luke (Springer International Publishing, Cham, 2020) pp. 457–499.

[250] R. Neutze, R. Wouts, S. Techert, J. Davidsson, M. Kocsis, A. Kirrander, F. Schotte, and M. Wulff, "Visualizing photochemical dynamics in solution through picosecond x-ray scattering", Phys. Rev. Lett. **87**, 195508 (2001).

[251] I. Rajkovic, J. Hallmann, S. Grübel, R. More, W. Quevedo, M. Petri, and S. Techert, "Development of a multipurpose vacuum chamber for serial optical and diffraction experiments with free electron laser radiation", Rev. Sci. Instrum. **81**, 045105 (2010).

[252] P. Wernet, K. Kunnus, I. Josefsson, I. Rajkovic, W. Quevedo, M. Beye, S. Schreck, S. Grübel, M. Scholz, D. Nordlund, W. Zhang, R. W. Hartsock, W. F. Schlotter, J. J. Turner, B. Kennedy, F. Hennies, F. M. F. de Groot, K. J. Gaffney, S. Techert, M. Odelius, and A. Föhlisch, "Orbital-specific mapping of the ligand exchange dynamics of $Fe(CO)_5$ in solution", Nature **520**, 78–81 (2015).

[253] P. Zalden, L. Song, X. Wu, H. Huang, F. Ahr, O. D. Mücke, J. Reichert, M. Thorwart, P. K. Mishra, R. Welsch, R. Santra, F. X. Kärtner, and C. Bressler, "Molecular polarizability anisotropy of liquid water revealed by terahertz-induced transient orientation", Nat. Commun. **9**, 2142 (2018).

[254] A. D. Smith, E. M. Warne, D. Bellshaw, D. A. Horke, M. Tudorovskya, E. Springate, A. J. H. Jones, C. Cacho, R. T. Chapman, A. Kirrander, and R. S. Minns, "Mapping the complete reaction path of a complex photochemical reaction", Phys. Rev. Lett. **120**, 183003 (2018).

[255] F. Lehmkühler, F. Dallari, A. Jain, M. Sikorski, J. Möller, L. Frenzel, I. Lokteva, G. Mills, M. Walther, H. Sinn, F. Schulz, M. Dartsch, V. Markmann, R. Bean, Y. Kim, P. Vagovic, A. Madsen, A. P. Mancuso, and G. Grübel, "Emergence of anomalous dynamics in soft matter probed at the European XFEL", PNAS **117**, 24110 (2020).

[256] F. Perakis, G. Camisasca, T. J. Lane, A. Späh, K. T. Wikfeldt, J. A. Sellberg, F. Lehmkühler, H. Pathak, K. H. Kim, K. Amann-Winkel, S. Schreck, S. Song, T. Sato, M. Sikorski, A. Eilert, T. McQueen, H. Ogasawara, D. Nordlund, W. Roseker, J. Koralek, S. Nelson, P. Hart, R. Alonso-Mori, Y. Feng, D. Zhu, A. Robert, G. Grübel, L. G. M. Pettersson,

and A. Nilsson, “Coherent x-rays reveal the influence of cage effects on ultrafast water dynamics”, Nat. Commun. **9**, 1917 (2018).

[257] A. Nilsson and L. G. M. Pettersson, “The structural origin of anomalous properties of liquid water”, Nat. Commun. , 8998 (2015).

[258] F. Perakis, K. Amann-Winkel, F. Lehmkühler, M. Sprung, D. Mariedahl, J. A. Sellberg, H. Pathak, A. Späh, F. Cavalca, D. Schlesinger, A. Ricci, A. Jain, B. Massani, F. Aubree, C. J. Benmore, T. Loerting, G. Grübel, L. G. M. Pettersson, and A. Nilsson, “Diffusive dynamics during the high-to-low density transition in amorphous ice”, PNAS **114**, 8193 (2017).

[259] L. V. Thesing, A. Yachmenev, R. González-Férez, and J. Küpper, “Laser-induced alignment of weakly bound molecular aggregates”, Phys. Rev. A **98**, 053412 (2018).

[260] P. J. Linstrom and W. G. Mallard, eds., *NIST Chemistry WebBook, NIST Standard Reference Database Number 69* (National Institute of Standards and Technology, Gaithersburg MD, 20899, 2017).

[261] D. R. Stull, “Vapor pressure of pure substances. organic and inorganic compounds”, Ind. Eng. Chem. **39**, 517 (1947).

[262] D. M. Murphy and T. Koop, “Review of the vapour pressures of ice and supercooled water for atmospheric applications”, Q.J.R. Meteorol. Soc. **131**, 1539 (2005).

[263] R. T. Jongma, Y. Huang, S. Shi, and A. M. Wodtke, “Rapid evaporative cooling suppresses fragmentation in mass spectrometry: Synthesis of "unprotonated" water cluster ions”, J. Phys. Chem. A **102**, 8847 (1998).

[264] V. Papadakis and T. N. Kitsopoulos, “Slice imaging and velocity mapping using a single field”, Rev. Sci. Instrum. **77**, 3101 (2006).

[265] J. S. Kienitz, *Orientation of state selected OCS molecules in mixed strong dc and laser fields*, Dissertation, Universität Hamburg, Hamburg, Germany (2016).

List of Publications

Publications related to this thesis

2020 *Spatial separation of 2-propanol monomer and its ionization-fragmentation pathways*
Jia Wang, Lanhai He, Jovana Petrovic, Ahmed Al-Refaie, **Helen Bieker**, Jolijn Onvlee, Karol Długołęcki, Jochen Küpper
Journal of Molecular Structure **1208**, 0022 (2020), *arXiv*:2001.07164

2019 *Spatial separation of pyrrole and pyrrole-water clusters*
Melby Johny, Jolijn Onvlee, Thomas Kierspel, **Helen Bieker**, Sebastian Trippel, Jochen Küpper
The Journal of Chemical Physics **721**, 149 (2019), *arxiv*:1901.05267

2019 *Pure Molecular Beam of Water Dimer*
Helen Bieker, Jolijn Onvlee, Melby Johny, Lanhai He, Thomas Kierspel, Sebastian Trippel, Daniel A Horke, Jochen Küpper
The Journal of Physical Chemistry **123**, 37486 (2019), *arxiv*:1904.08716

2018 *Knife edge skimming for improved separation of molecular species by the deflector*
Sebastian Trippel, Melby Johny, Thomas Kierspel, Jolijn Onvlee, **Helen Bieker**, Hong Ye, Terry Mullins, Lars Gumprecht, Karol Długołęcki, Jochen Küpper
The Journal of Chemical Physics **89**, 096110 (2018), *arXiv*:1802.04053

Acknowledgments

Herewith, I would like to thank all the people that contributed to this work and supported me during this hard time. Originally I named this thesis "The Water Dimer Goes Crazy", because the water dimer (and others) drove me crazy.

Nevertheless, I would like to thank my supervisors Jochen Küpper and Daniel Horke to give me the opportunity to do science at such an amazing place like Center for Free-Electron Laser Science (CFEL) and Deutsches Elektronen-Synchrotron (DESY) and for believing in me, while I was doubting myself. I really appreciate the time I was allowed to spend with so many great scientists.

Further, I would like to thank Prof. Dr. Daniela Pfannkuche, Prof. Dr. Gerhard Grübel and Prof. Dr. Arwen Pearson for being members of my PhD committee.

In addition, I would like to thank my graduate school The Hamburg Center for Ultrafast Imaging (CUI) for paying my salary and giving me the chance to meet other PhD students and to give me a great overview over the science that has been done by other PhDs within the framework of CUI. I would also like to thank the State Graduate Funding Program scholarships (HmbNFG) for the funding of my last year, which gave me the chance to finish my PhD thesis.

A special thanks goes to Jolijn Onvlee. You are a genius and incredible talented, motivating and helpful. You did so much for me and others in this group that I could fill a whole book with it. Another big thanks goes to Daniel Horke, Sebastian Trippel, Nicole Teschmit, Melby Johny, Thomas Kierspel, Joss Wiese and Lanhai He for supporting me with the measurements and the analysis. I really learned a lot from you and am very thankful for all your ideas and constructive feedback. I would also like toto Yahya Saleh, Andrey Yachmenev and Boris G. Sartakov for your help with the non-rigid water dimer simulations I wouldn't have been able to do without you. You all are so clever, that is beyond my mind. A big thanks goes the whole team of the beamtime 2018 at Petra III. Firstly, the people that joined the shift with me: Jolijn Onvlee, Melby Johny, Lanhai He, Rebecca Boll and Florian Trinter. All of you are just amazing, intelligent and nice people and I really enjoyed to work with you. And of course I would also like to thank the people that took over the other half of the shifts: Sebastian Trippel, Thomas Kierspel, Terry Mullins, Daniel Horke and Hong Ye. I appreciate all the time and effort you put into this beamtime. Jolijn Onvlee, Joe Chen, Stefanie Kerbstadt, Emil Zak, Evangelos Karamatskos, Amit Samanta, Linda Thesing, Yahya Saleh and Lanhai He thank you all for reading through my thesis and to make it better step by step.

I would also like to thank all the people that I got to know during this time and I hope that we are going to stay connected afterwards. At first, Bastian Deppe, thank you so much for being the first one make me feel welcomed in this group. Daniel Gusa, the second friend I found, thanks for the pogo dance at the Zebrahead concert and the joint

tantrums in the lab. Nils Roth, you creative and smart boy, you were my survival kit and best friend at work. I enjoyed all the crazy discussions we had during lunch breaks and every kg I gained was worth it. Thanks for teaching me to think outside the box and to see things from different angles. Joss Wiese, it was a pleasure to work and hang out with you and see your passion about molecular science, music and your friends. You are a genius but still helpful, nice and interesting. Power! Pau Gonzalez, you would have deserve to get your PhD already during your time at CMI instead of your master degree. You are so smart and impressed me a lot with your passion and interest. Frederike Ahr, thanks for being so open and friendly and for all the joint lunches at Lincontro. Jolijn Onvlee, Melby Johny, Lanhai He and Ruth Livingstone, you all are so powerful, smart and friendly. Thanks for spending time with me and for all cheer ups. Joe Chen, thanks for talking to me during your stay at CFEL. Every year, I am happy to achieve a happy birthday message from you. Thank you so much for reading through my thesis during these crazy Corona-virus times. Lena Worbs, Jannik Lübke, Guang Yang and Yahya Saleh, you all are so smart, nice and talented. Unfortunately, suffering is the biggest part of the PhD, please keep in mind: you will get your PhD and you deserve it! Whatever happens keep believing in you, as I do. Amine Gourram, you are so motivated and strong. I am sure you will reach your goals and find a business idea that will make you to a happy and successful business man! Stefanie Kerbstadt, in a very short time, you showed my how strong, powerful and intelligent you are. I am sure, that you can reach to the top very quickly and amaze other people, as you amazed me! Barbora Vagovic, thanks a lot for all the paper work and meeting arrangements you have done for me and for being the connection with Jochen. Jean-Francois Olivieri, thanks for the great vacation and the hikes at Yosemite National Park. You are not only super smart, but also super sporty. Mohamed Youssef, another impressive and nice person. Thanks for your nice words!

I thank all the people that are or have been working in CMI and that I was allowed to get to know during the time here. All of you showed me how great personalities you have and how talented you are! Thanks to all former CMI PhD students: Nele Müller, Jens Kienitz, Thomas Kierspel, Bastian Deppe, Nicole Teschmit, Salah Awel, Zhipeng Huang, Evangelos Karamtskos, Linda Thesing, Joss Wiese and Nils Roth. You gave me some hope, that it is possible to finish the PhD. Thanks to all current members of the CMI group: Barbora Vagovic, Andrey Yachemenev, Emil Zak, Karol Długołęcki, Amit Samanta, Muhamed Amin, Hubertus Bromberger, Armando Estillore, Lanhai He, Stefanie Kerbstadt, Jia Wang. I am sad to leave you behind, but am looking forward for something new. And thanks to all former members of the CMI group: Amine Gourram, Andrey Duchko, Jovana Petrovic, Terry Mullins, Igor Rubinsky, Ahmed Al-Refaie, Alec Owens, Xiaoyan Sun, Vijay Singh, Michele Di Fraia, Andrea Trabattoni, Ruth Livingstone, Tim Ossenbrüggen, Nicolai Pohlmann. You all helped me in one way or the other.

Thanks to everyone of CMI that contributed to all the PhD hats, speeches, fancy theaters and games we invented. I had a lot of fun with you. In particular, Karol Długołęcki, you

and your skills are so amazing!

Another group of people that helped me to overcome all the frustration during the PhD time are the organizers of the Deutsche Physikerinnentagung 2016 in Hamburg on DESY campus. Nele Müller, Marie Lutz, Francesca Moglia, Stephanie Manz, Melanie Schnell, Elina Fuchs, Caroline Arnold and Gudrid Moortgat-Pick. It was a pleasure to work with you and to meet such great role models. I really enjoyed the working atmosphere, which gave me some hope and the feeling of being appreciated, which I needed the most back then. A special thanks in that respect goes to Nele Müller, as I became a member of that group because of you.

I would also like to thank all old and new friends, the Hip Hop and the Musical dance classes of Saba Pedük Dance Classes. You made Hamburg feel like home.

A very special thanks goes to my family: Mama, Papa and Ute, Laura, Simon, Mira and Fabio, Ruben, Selina and Spike, thanks for accepting me being quiet, when I wasn't feeling well, but still not giving up on me. I love you all so much! Everyone of you is awesome in your own way and I am happy to have you in my life! I know the past years weren't easy for you, seeing me suffering. But only because of your love I could keep going. In particular, Mira and Fabio, the two of you are lightening up my heart every time I see you. To me you are still the most incredible wonder in my life.

Last but not least, the person I am spending most of my time with is my best friend, boyfriend and co-fighter Michael Diez. Who made me aware of the open position for this PhD position. It is a boon and bane, when both are doing their PhD at the same time. I hate to see you suffering, while I am suffering myself and knowing that nothing I say would make you feel better. But I won't stop trying: you are incredible smart, nice, interesting and the most wonderful person in my life. I am so happy to be with you and I am looking forward to our future. I love you!